Università degli Studi di Padova

Dipartimento di Matematica "Tullio Levi-Civita"

Corso di Dottorato in Scienze Matematiche

Curriculum Matematica

Ciclo XXXVIII

Chaotic Transport in the Solar System

Coordinator
Prof. Giovanni Colombo
Supervisor
Prof. Massimiliano Guzzo
Co-Supervisor
Prof. Elena Lega

Candidate:
Xiang Liu

Academic Year: 2022-2025

To my grandfather.

Abstract

This thesis is dedicated to the study of chaos and diffusion in the mean motion resonances (MMRs) of the circular restricted three-body problem (CT3BP), focusing on the orbits that undergo close encounters with the secondary body. First we implement a semi-analytical averaging method to compute the averaged Hamiltonian for a specific MMR, and we verify its effectiveness to approximate the motions whose orbits cross the orbit of the secondary body, as well as the situations in which such an approximation is not acceptable. This study requires a careful examination of the representation of the collision singularities and the associated Fourier expansions of the perturbing function, in the specific action-angle variables used for the representation of the averaged Hamiltonian. Afterwards, we investigate two aspects of the problem: the boundaries of application of Hamiltonian perturbation theory (i.e. the conjugation of the averaged Hamiltonian to the original one) and the chaotic diffusion that can result from the accumulation of the effects of multiple close encounters with a planet. The planar and spatial CR3BP have been studied separately. Indeed, the different dimensionality of the planar and spatial cases impacts both the analytic representation of the aforementioned singularities as well as on the mechanisms that determine the chaotic nature and instability of the resonant motions. Both problems have been studied by leveraging: the computation of approximate first integrals, obtained from a canonical transformation of the Hamiltonian of the CR3BP; the computation of Fast Lyapunov Indicators, obtained from numerical integrations of the regularized equations of motion; the analytic representation of the gravitational singularities and of the singularities of the Fourier expansion of the perturbing function, in the resonant action-angle variables; the computation of the adiabatic invariants, which are the main tool to study the chaos generated by the crossing of a separatrix in the spatial CR3BP.

Our results indicate that the efficacy of the averaging method is confirmed also for the orbits which cross the orbit of the secondary body, except when they enter a neighborhood of the set where the Fourier transform of the perturbation with respect to the fast angle of the resonant is singular. Quite unexpectedly, the averaging method proves to be effective also when large parts of the resonant phase-plane are affected by chaotic diffusion, as it has been revealed by the computation of the regularized FLI. In these regimes, already one step of the perturbation theory is sufficient to reveal the properties of these chaotic diffusions which occur with small random almost-stepwise variations of the quasi-integrals of motion similarly to the Arnold diffusion. Chaotic diffusion in particular is effective in removing phase-protection mechanisms, leading to possible deep close encounters.

For the spatial problem, we also provide examples of chaotic diffusion which,

in addition to the crossings of a separatrix, are due to the accumulation of effects of weak close encounters. In particular, we will provide orbits having a deeper close encounter which determines the extraction from a main resonance, and the subsequent cascade of close encounters determines a slower chaotic diffusion between the nearby resonances. The numerical examples of Chapter 3 and 4 have been provided for the 1:2 external mean motion resonances, for the value of the mass parameter which represents the Sun-Neptune system.

Sommario

Questa tesi è volta allo studio di fenomeni di caos e diffusione nelle risonanze di moto medio (MMR) del problema dei tre corpi ristretto circolare (CT3BP), concentrandosi sulle orbite soggette ad incontri ravvicinati con il corpo secondario. In primo luogo, viene implementato un metodo di media semi-analitica per calcolare l'hamiltoniana media per uno specifico MMR, e ne verifichiamo l'efficacia sia nell'approssimare i moti delle orbite che intersecano la traiettoria del corpo secondario, che nelle situazioni in cui tale approssimazione non è possibile. Questo studio richiede uno scrupoloso esame della rappresentazione delle singolarità di collisione e delle espansioni di Fourier della funzione perturbata, nelle specifiche variabili azione-angolo utilizzare per la rappresentazione dell'hamiltoniana media. Successivamente investighiamo due aspetti del problema: i limiti dell'applicazione della teoria hamiltoniana perturbativa (ovvero la coniugazione dell'hamiltoniana media con quella originale) e la diffusione caotica che può risultare dall'accumulo degli effetti di molteplici incontri ravvicinati con una pianeta. Il problema dei tre corpi circolare ristretto è stato studiato separatamente nel caso piano e in quello spaziale. Infatti, la diversa dimensione del problema planare e spaziale ha un impatto tanto sulla rappresentazione analitica delle suddette singolarità, quanto sui meccanismi che determinano la natura caotica e l'instabilità dei moti risonanti. Entrambi i problemi sono stati studiati utilizzando: il calcolo di integrali primi approssimati, ottenuti dalla trasformazione canonica dell'hamiltoniana del CR3BP; il calcolo dei Fast Lyapunov Indicators, ottenuti da integrazioni numeriche delle equazioni regolarizzate dei moti; la rappresentazione analitica delle singolarità gravitazionali e delle singolarità delle espansioni di Fourier della funzione perturbata, nelle variabili azione-angolo; il calcolo degli invarianti adiabatici, che sono i principali strumenti per studiare il caos generato dall'intersezione di una separatrice nel CR3BP spaziale.

I risultati ottenuti indicano che l'efficacia del metodo della media è confermata anche per le orbite che intersecano la traiettoria del corpo secondario, fatta eccezione per il caso in cui esse attraversano un intorno dell'insieme in cui la trasformata di Fourier della perturbazione rispetto all'angolo veloce della risonanza è singolare. Inaspettatamente, il metodo della media risulta efficace anche quando grandi parti dello spazio delle fasi risonante subiscono l'influenza della diffusione caotica, come rivelato dal calcolo dell'FLI regolarizzato. In questi regimi, anche un solo passo della teoria perturbativa è sufficiente per rivelare le proprietà di questa diffusione caotica, che si verifica con piccole variazioni casuali quasi impulsive dei quasi-integrali del moto, analogamente alla diffusione di Arnold. Inoltre, la diffusione caotica è efficace nell'eliminare i meccanismi di protezione di fase, portando a possibili incontri ravvicinati profondi.

Per il problema spaziale, vengono presentati esempi di diffusione caotica che, oltre all'attraversamento di una separatrice, sono dovuti all'accumulo degli effetti di incontri ravvicinati deboli. In particolare, forniremo esempi di come un incontro ravvicinato più profondo possa determinare l'estrazione da una risonanza principale, e la successiva cascata di incontri ravvicinati determini una diffusione caotica più lenta tra le risonanze vicine. Gli esempi numerici del Capitolo 3 e 4 sono stati forniti per risonanze esterne di moto medio 1:2, quando il valore del parametro di massa rappresenta il sistema Sole-Giove ed il sistema Sole-Nettuno.

Contents

Abstract **ii**

Sommario **iv**

1 Introduction **1**

2 Restricted Three-Body Problem **8**

2.1 The Restricted Three-Body Problem 8

2.1.1 Equations of Motion in Heliocentric coordinate frame 8

2.1.2 Hamiltonian representation of the CRTBP 9

2.1.3 Orbital elements 10

2.1.4 Delaunay Variables 13

2.2 Hamiltonian Perturbation Theory 14

2.2.1 Nearly-Integrable Hamiltonian Systems 15

2.2.2 Lie Series Method 16

2.2.3 The resonant normal form 18

2.3 The MMRs of the CRTBP 20

2.3.1 Resonant action-angle variables 22

2.3.2 Resonant normal form Hamiltonian 24

2.4 Regularizing the Circular Restricted 3-Body Problems 26

2.4.1 Equations of Motion of the CRTBP in the Synodic Coordinate System 27

2.4.2 The Levi-Civita Regularization for the PCRTBP 29

2.4.3 The Kustaanheimo-Stiefel Regularization for the SCRTBP . 30

2.5 Fast Lyapunov chaos indicators 31

2.5.1 The finite time chaos indicator 31
2.5.2 FLI for the PCRTBP in MMR 37

3 The limits of canonical perturbation theory inside MMRs for crossing orbits and close encounters: the planar case 40
3.1 Fourier expansions, singular sets and sets of close encounters 41
3.1.1 The singular set and the set of close encounters 44
3.1.2 Singular sets and Fourier expansions 49
3.2 Definition of the averaging transformation 55
3.3 Numerical explorations 59
3.3.1 Analysis of the 1:2 MMR with Jupiter 59
3.3.2 Comparisons with the Sun-Neptune case and the 5:6 resonance 69
3.3.3 Technical details 74
3.4 Conclusions 77

4 Explorations of chaotic diffusions triggered by multiple close encounters in a MMR: the spatial case 79
4.1 The averaged Hamiltonian, the singular set and the line of MRD . . 80
4.1.1 Definition of the averaging transformation 82
4.1.2 Characterization of the collision and singular sets 83
4.1.3 The perturbing function and the singular set 88
4.2 Examples of resonant Lidov-Kozai dynamics and close-encounters . 91
4.2.1 Below the critical value 91
4.2.2 Near the critical value 94
4.2.3 Above the critical value 98
4.3 Appendix and remarks 106
4.3.1 Classification of regions in Phase-Space 106
4.3.2 Adiabatic invariants for the CRTBP inside MMRs 107
4.3.3 The Fast Lyapunov Indicator 109
4.4 Conclusions 110

A Computation of the perturbation function $\widehat{\mathcal{H}}_1$ with resonant variables 111

Acknowledgements 113

Chapter 1

Introduction

In the Solar System, mean motion resonances (MMRs), which occur when the ratio of the orbital periods of two celestial bodies is equal to a ratio of small integers, play a crucial role in the dynamics of small bodies. An asteroid in a mean motion resonance with a planet can have a repeating configuration, which may correspond to either stable or unstable motion, depending on a multitude of complex factors. For example, the famous Kirkwood gaps in the distribution of the main belt asteroids are due to the instability inside certain MMRs (corresponding, for example, to the locations of the 3:1, 5:2, and 7:3 MMR with Jupiter). Another celebrated example is Pluto, a trans-Neptunian object, which is in 2:3 MMR with Neptune. The orbit of Pluto has high eccentricity ($e \simeq 0.25$) and high inclination ($i \simeq 17^\circ$), and it crosses the orbit of Neptune. However, due to the stabilization effect of the 2:3 MMR with Neptune, Pluto never collides with it. The aforementioned Kirkwood gaps are examples of inner resonance in the sense that the semi-major axis of the asteroid is smaller than the semi-major axis of the planet (Jupiter in this case), while the 2:3 MMR between Pluto and Neptune is an example of exterior resonance, where the semi-major axis of Pluto is larger than that of Neptune. More generally, the exterior MMRs with Neptune are important for the dynamics of trans-Neptunian objects. There is extensive research in the literature on MMRs, see for instance[1] [HenL83, Lam84, Hadji93, MorM93, Morbi95, WinMur97a, GroM98, Mal98, Nesv02, ValseMGC03, NeiSido04, PetroMalTre13, WangMal17, AntoLib18, Hadji93, MorM93, Morbi95, WinMur97a, Nesv02, NeiSido04, PetroMalTre13, Féj16, WangMal17, AntoLib18].

In this thesis we specifically study chaos and diffusion inside the MMRs of the circular restricted three-body problem (CRTBP), focusing on the orbits that undergo close encounters with the secondary body.

[1] This list is far to be comprehensive.

The starting point is that the crossing of a separatrix within a MMR with a planet is recognized as one of the primary mechanisms of chaos generation [Wis83, Nei87b, NeiSido04] for an asteroid. Additional sources of chaos, arising from gravitational interactions, are associated with, for example, three-body or secular resonances and close encounters. In the context of chaos generation within a MMR, adiabatic theory provides the theoretical model to study the coupling between the chaotic motions of the semi-secular resonant normal form variables and the long-term evolution of eccentricity and inclination (see, for example, [Wis83, Nei87, NeiSido04, Sido06, SidoNAZ14, MilB98, EfimS20, Sido24, FerS89, Mor02, NesTFM02, Sail16, Gal20, FenGS22, Pan25]). At high eccentricities, Chirikov diffusion [Chirikov, MorG97, Mor02] within nearby resonances and close encounters with planets become relevant. In fact, the amplitude of separatrices of the resonant normal forms overlap at suitable large values of the eccentricity [MorTM95, Mor02] and when the orbits cross the planetary orbits the occurrence of close encounters and collisions is possible.

Some studies have modeled the effect of individual close encounters, which may induce a sharp change in the orbital elements, potentially leading to extraction from a MMR [Opik76, Valse02, Guzzo24]. Other studies have incorporated the effects of close encounters into averaged normal form dynamics to the maximum extent possible (for example, in [LidZ74, FerS89, Bea94, MorTM95, Tho98, GroM98, MilB98, RoigSFT97, Mor02, NesF00, NesF01, NesTFM02, Sido06, Fer07, GroT12, SidoNAZ14, Sail16, MaroG18, EfimS20, Gal20, Pan25, FenGS22, Sido24]). In fact, while the averaged normal form may be not valid to describe the effect of an individual deep close encounter, it can be used to study the evolution of the orbital elements of the asteroid (or comet) in cases where the minimum distance between the asteroid and the planet, attained during a resonant cycle, may progressively decrease. When the close encounter is sufficiently deep, it may produce sharp variations of the averaged Hamiltonian, and extract the small body P from the given MMR. In the planar problem, the analysis of close encounters in a MMR is simplified by specific features [MorTM95, Tho98, NesTFM02]. In particular, the normal form Hamiltonian of a $p : q$ MMR is completely integrable (apart from a remainder that is initially neglected), since it depends on the angles only through the critical angle of the resonance $\sigma = q\lambda - p\lambda_1 - (q-p)\varpi$. Correspondingly, for the planar problem the quantity:

$$N_{pl} = \sqrt{a}[p - q\sqrt{1-e^2}] \tag{1.1}$$

is a first integral and for every given value of N_{pl} the dynamics have a phase-portrait which can be represented in the plane of the resonant variables S, σ (S is the conjugate action to σ; see for example [HenL83, Lam84, WinMur97a, WinMur97b, Mor02]). The action N_{pl} defined in (1.1) is therefore the crucial parameter to

classify the phase-portraits of the averaged Hamiltonian of the planar problem (see, for example, [HenL83, Lam84, Bea94, Mor02]). On the one hand, its value determines the localization of the equilibria of the averaged Hamiltonian and of their separatrices (see, for example, [HenL83, Lam84, Bea94, Mor02]); on the other hand, thanks to its peculiar dependence as a function of semi-major axis and eccentricity, its value indicates also the possibility of collisions with the planet, hereafter denoted by P_1 (see [Bea94, Tho98, Mor02]). In fact, for given values of the semi-major axis, larger values of N_{pl} correspond to larger values of the eccentricity. In particular, there is a critical value of N_{pl}, which we denote by N_c hereafter, such that all the orbits with $N_{pl} < N_c$ do not intersect (and are not tangent to) the orbit of P_1.

It is well established that the averaged Hamiltonian describes accurately the resonant dynamics for values on N_{pl} which are definitely smaller than N_c so as collisions, but also close encounters of P with P_1 are ruled out. Instead, for values of N_{pl} which are close to or larger than the critical value N_c the validity of the averaging method is more uncertain and merits further investigations. In fact, in this case the averaged Hamiltonian could be effective when P is far from P_1, while it may lose efficiency, and strong instability can show up, when P approaches P_1 [Bea94, Tho98, Mor02, NesTFM02]. In particular, for the planar case, specific curves of the resonant phase-plane have been identified as sets where a collision of P with P_1 is possible [Bea94, MorTM95, Tho98, NesTFM02]; these curves will be called singular sets.

The singular sets play a crucial role in the generation of complex orbits with essentially two mechanisms. In the first one, studied in [MorTM95, Bea94], following the level curves of the resonant phase-portrait an orbit may hit the singular set and P experiences a deep close encounter with P_1. During the deep close encounter the value of the perturbing function is possibly divergent, and therefore the averaging method is not effective. Correspondingly, the function N_{pl} ceases to be a first integral and may undergo large variations. In the second one, which will be studied in this thesis (see Chapter 3), following the level curves of the resonant phase-portrait the orbit approaches the singular set at a relatively small distance corresponding to a weak encounter of P with P_1. In this case, even if the value of the perturbation is increased during the weak close encounter, we find that the averaging method remains effective. As a result, during the weak close encounter we detect tiny variations of N_{pl} and of the value of the averaged Hamiltonian, which may increase the amplitude of resonant librations and decrease the minimum distance attained at subsequent close encounter. Therefore, when P experiences several weak close encounters, we observe the chaotic accumulation of the small variations of N_{pl} and of the value of the averaged Hamiltonian, producing a complex trajectory. We detect this behavior also in orbits with values of N_{pl} which are slightly smaller

than the critical value N_c for which the singular set appears. Finally, chaos due to resonance overlapping may interplay with both mechanisms, reducing the efficacy of perturbation theory in large areas of the resonant phase-portrait.

The various dynamical instability mechanisms outlined above are studied in Chapter 3. First, we study the boundaries of validity of the averaging method for the PCRTBP, specifically the validity of the normal form approximations, for values of N_{pl} which are close to or larger than the critical value N_c. Given the multitude of potential factors contributing to the possible failure of the averaging method, and the emergence of complex dynamics, a more comprehensive understanding will be achieved by supplementing the information provided by phase-portrait representations of the averaged Hamiltonian with analyses concerning the preservation of the function N (computed through at least one step of perturbation theory) and the computation of Fast Lyapunov Indicators (FLI hereafter) regularized with respect to the close encounters with the secondary body P_1. Originally introduced in [FroGL97a, FroLG97b], the FLI method has been successfully developed for detecting the distribution of chaotic and regular motions in the phase-space of dynamical systems, as well as to localize the stable and unstable manifolds of hyperbolic fixed points and normally hyperbolic invariant manifolds [RosG24, GuzL23, ScantaG, GuzL18, GuzL15, GuzL17, LegG16, LegGF16, GuzL15, GuzL14, GuzL13b, GuzL13, LegGF11, TodoGLF11, LegGF10, GuzLF09a, GuzLF09, FroGL05a, FroGL05, FroGL00, FroGL01]. Regularized FLI, which are defined using the equations of motion of the CRTBP regularized with respect to the collisions with the secondary body, have been defined since [CelSLF11, LegGF11, GuzL13, GuzL14, LegG16, GuzL18, GuzL23, RosG24]. In this thesis regularized FLIs are used to compute the distribution of regular and chaotic motions inside the MMRs, for large values of the eccentricity, and compare the results with the phase-portraits of the averaged Hamiltonian (see Section 2.5 for an introduction to the FLI method and Chapters 3 and 4 for new applications to the planar and spatial CRTBPs).

The computation of the time evolution of the function N in particular requires to compute explicitly the averaging transformation in all the resonant phase-plane with the exclusion of a small neighborhood of the singular set. It is well known that, when the eccentricity is large, this computation may be affected by several singularities, including singularities in the Fourier expansion of the perturbing function expressed with the Delaunay variables. To perform our analysis we therefore first assess the validity of a suitable Fourier expansion which is regular also for large values of the eccentricity, up to a small distance from the singular sets. Then, we show that the averaging transformation $\mathcal{C}$ constructed using such expansion is suitably precise: to define the quasi-integral of motion N_{pl} (accurate up to order ε^2) outside a small neighborhood of the singular set also for orbits of large eccen-

tricity crossing the orbit of P_1; to provide a good preservation of both N_{pl} and of the averaged Hamiltonian for regular orbits which are phase-protected from close encounters; to describe complex dynamics such as the those generated by chaotic motions of large libration amplitudes which initially are phase-protected by close encounters, but the chaotic diffusion of N_{pl} and of the averaged Hamiltonian lead to close encounters between P and P_1. The results are compared with the numerical computations of the FLI, regularized with the respect to the close encounters with the secondary body P_1, on very refined grids of the resonant phase-plane which reveal the emergence of chaos due to resonance overlapping and close encounters (see [GuzL13, GuzL23, RosG24]). The informations provided by the computations of the phase-portrait representations of the averaged Hamiltonian, by the preservation of N_{pl} and of the averaged Hamiltonian, and by the computation of FLI, are used to study in the detail the 1:2 external MMR for values of the mass ratios which are representative of the Sun-Jupiter case[2]. Comparisons with the 1:2 and 5:6 MMR with Neptune will also be provided. The efficacy of the averaging transformations for the analysis of the dynamics in MMR is tested and established also for chaotic orbits of eccentricity up to $e \simeq 0.55$. The choice of these model resonances has been done according to the different values of the resonant semi-major axis: the 5:6 resonance represents the limit case of a resonance very close to the semi-major axis of the planet, while the 1:2 resonance is more distant from this value. Both resonances are of first order to optimize the description of the analytic part; resonances of larger order may be considered with a proper re-definition of the resonant variables. Only external resonances are considered for two reasons. The first reason is that external resonant encounters had been identified by several authors to be relevant for the diffusion of Kuiper belt objects to the inner part of the Solar system. The second reason is that we can use the same analytic framework, and simplify the discussion of the results. Internal resonances may be considered as well, with suitable modifications of the variables and the expansions.

Quite unexpectedly, we find that the averaging method is effective also when large parts of the resonant phase-plane are affected by chaotic diffusion, revealed by the computation of the regularized FLI. In these regime, already one step of perturbation theory reveals the properties of these chaotic diffusions which occur with small random almost-stepwise variations of N_{pl} and of the averaged Hamiltonian, similarly to the Arnold diffusion detected in [GuzEP20]. In particular, we find that chaotic diffusion is effective in removing phase-protection mechanisms, leading to possible deep close encounters. Within deep close encounters, as expected, the resonant averaging is not effective, and other perturbation methods could be employed (such as the perturbation theory developed in [Guzzo24]) and

[2]Since the circular restricted three-body problem represents an approximation of the real problem, we prefer to use the approximated values for the mass ratios $10^{-3}, 0.0000515139$.

used to complement the previous analysis.

The analysis of the singularities of the averaged Hamiltonian in the spatial CRTBP is complicated by the more complex geometry of close encounters due to the higher dimensionality [NesTFM02, Sail16, FenGS22, Sido24]. In the spatial case, the flow of the averaged Hamiltonian still has a first integral:

$$N = \sqrt{a}\left(p - q\sqrt{1-e^2}\cos(i)\right), \tag{1.2}$$

which generalizes the integral N_{pl} of the planar problem, but is not integrable since the averaged Hamiltonian depends on two angles, and it can exhibit chaotic motions generated by the crossing of a separatrix[Wis83, Nei87, NeiSido04]. In the spatial case, we have two relevant phase-planes: a plane of the semi-secular variables S, σ, where σ is the critical angle of the resonance and S its conjugate action, and a plane of variables A, α, representing only secular evolution. The chaotic diffusion of the secular variables A, α can accumulate to secular instability, which has been effectively studied in the literature using the theory of adiabatic invariants [Wis83, Nei87, NeiSido04] applied to the averaged Hamiltonian. Another source of slow secular instability in external MMRs has been related to sequences of close encounters with a planet. For example, in [Mor97], the ejection of comets from the 2/3 MMR has been related to the combination of chaotic diffusion and collisional 'kicks'.

The second part of the original research of this thesis, described in Chapter 4, will focus on the problem or orbits in a $p : q$ MMR experiencing close encounters in the spatial CRTBP. From a technical point of view, the implementation of the averaging method inside the MMR is analogous with that of the planar problem, but the dynamics and the representation of the gravitational singularities is quite different, due to the higher dimensionality of the phase-space. In fact, the averaged Hamiltonian of the SCRTBP, still having the action N as a first integral, has two degrees of freedom, of which one is the critical angle of the resonance $\sigma = q\lambda - p\lambda_1 - (q-p)\varpi$ and the other one is related to the argument of perihelion $\alpha = -\omega$. Indeed, the variables σ and its conjugate action S are semi-secular variables and the other pair of action-angle variables α, A are secular variables. The crossing of a separatrix in the plane of semi-secular variables, and the coupling with the secular ones may determine chaotic diffusion of the secular variables which accumulate to secular instability. These complex dynamics have been studied using the theory of adiabatic invariants [Wis82, Wis83, Wis85, Nei87, Nei87b, NeiSido04, NeiSido04, Sido06, SidoNAZ14, Sail16, Sido24] applied to the averaged Hamiltonian. Another source of instability in external MMRs is related to sequences of close encounters with a planet. For instance, we refer to the already quoted examples for the planar problem, as well as the already mentioned paper [Mor97], where the ejection of

comets from the 2:3 MMR has been related to combination of chaotic diffusion and collisional 'kicks'.

In Chapter 4 we analyze in detail how the crossing of a region of the resonant plane S, σ, where close encounters with a planet occur, results in a combination of adiabatic chaos, which occurs with the conservation of the averaged Hamiltonian $\widehat{\mathcal{H}}$ and of the action N, and diffusion of these quantities. In fact, we see that between two consecutive clusters of close encounters, the averaging method is effective, showing a good conservation of of $\widehat{\mathcal{H}}$ and N. Correspondingly, far from close encounters the dynamics is studied using the theory of adiabatic invariants, which provides a precise and complete characterization of the projections of the averaged orbits to the semi-secular plane S, σ and the secular plane A, α. Instead, at close encounters, we observe almost step-wise jumps of $\widehat{\mathcal{H}}$ and N, possibly determining the extraction from the MMR. In fact, when the close encounter is sufficiently deep, it can alone determine the extraction from the MMR. But, for moderate close encounters the step-wise jumps of $\widehat{\mathcal{H}}$ and N are qualitatively similar to the ones modelled for Arnold diffusion in [GuzEP20]. In particular, when the examined orbits arrive just outside the external separatrix that delimits the resonance, they begin a sequence of moderate close encounters that can lead them towards other nearby resonances, as for the Chirikov diffusion. In more detail, the analog of the singular set (which was the most relevant geometric object in the planar case) is generally just a point in the semi-secular phase-plane S, σ and its role is replaced by a curve of values of the plane S, σ (for given values of A, N, α) characterized by a possible small distance from P_1. The definition of this curve is well formulated using an indicator of the minimum distance of P from P_1 attained on the orbits with given values of the resonant variables S, A, N, σ, α, which we call Minimum Resonant Distance (MRD) (See Eq. (4.24)). We remark that the MRD is not the Minimum Orbital Intersection Distance (MOID); in fact we can have value of S, A, N, σ, α compatible with orbits of MOID equal to zero, and strictly positive MRD.

A neighborhood of the curve of minimum MRD represents the place of the plane S, σ where resonant motions (regular or chaotic) may undergo a close encounter with the planet, determining a jump in the values of $\widehat{\mathcal{H}}$ and N, possibly extracting P from the region of resonant librations. Following this event, P may enter a chaotic region characterized by many crossings with the region of small MRD, determining a diffusion towards a nearby MMR. This process is similar to the Chirikov diffusion between nearby overlapping resonances, but is triggered by close encounters: the diffusion is due to the accumulation of the sharp variations of N and of the averaged Hamiltonian occurring at close encounters of P with P_1. In the same time, chaotic diffusion is observed for the variables A, α.

Chapter 2

Restricted Three-Body Problem

In this Chapter we introduce some basic notions and some fundamental tools and methods which are going to be applied in this thesis. First we introduce the restricted three-body problem in the heliocentric reference frame, its Hamiltonian formulation, the orbital elements and the Delaunay variables. Then we present a synthesis of Hamiltonian perturbation theory inside resonant domains. For the basic formulas appearing in Section 2.1,2.2,2.3 we refer to [Mor02, MurDer00] After that we introduce specific resonant variables and normal forms for the MMRs of the restricted three-body problem. Also we introduce the regularization method for the restricted three-body problem, which will be used for the numerical integration of motions with close encounters and collisions. Last, the Fast Lyapunov Indicators (FLIs) will be introduced and examples of about the use of the so called FLI method will be provided.

2.1 The Restricted Three-Body Problem

2.1.1 Equations of Motion in Heliocentric coordinate frame

Consider a gravitational system consisting of three bodies P_0, P_1 and P_2 (for instance the Sun, a planet, and an asteroid, respectively) of masses m_0, m_1, m_2 and position vectors $\bar{\mathbf{r}}_0, \bar{\mathbf{r}}_1, \bar{\mathbf{r}}_2$ whose motion in a barycentric inertial reference frame is determined by the equations

$$\frac{\mathrm{d}^2\bar{\mathbf{r}}_i}{\mathrm{d}t^2} = -\mathcal{G}\sum_{j\neq i} m_j \frac{\bar{\mathbf{r}}_i - \bar{\mathbf{r}}_j}{\|\bar{\mathbf{r}}_i - \bar{\mathbf{r}}_j\|^3}, \quad i = 0, 1, 2 \tag{2.1}$$

where $\mathcal{G}$ denotes the gravitational constant. The system (2.1) can be reduced by considering the heliocentric radius vectors of the planet and the asteroid $\mathbf{r}_i :=$

$\bar{\mathbf{r}}_i - \bar{\mathbf{r}}_0$, $i = 1, 2$

$$\begin{aligned}
\frac{\mathrm{d}^2\mathbf{r}_1}{\mathrm{d}t^2} &= -\mathcal{G}(m_0 + m_1)\frac{\mathbf{r}_1}{\|\mathbf{r}_1\|^3} + \mathcal{G}m_2\left(\frac{\mathbf{r}_2 - \mathbf{r}_1}{\|\mathbf{r}_2 - \mathbf{r}_1\|^3} - \frac{\mathbf{r}_2}{\|\mathbf{r}_2\|^3}\right) \\
\frac{\mathrm{d}^2\mathbf{r}_2}{\mathrm{d}t^2} &= -\mathcal{G}(m_0 + m_2)\frac{\mathbf{r}_2}{\|\mathbf{r}_2\|^3} + \mathcal{G}m_1\left(\frac{\mathbf{r}_1 - \mathbf{r}_2}{\|\mathbf{r}_1 - \mathbf{r}_2\|^3} - \frac{\mathbf{r}_1}{\|\mathbf{r}_1\|^3}\right)
\end{aligned} \tag{2.2}$$

and the motion of the Sun satisfies $\bar{\mathbf{r}}_0 = -\frac{m_1\bar{\mathbf{r}}_1 + m_2\bar{\mathbf{r}}_2}{m_0+m_1+m_2}$.

In this thesis we consider the restricted case, defined when the mass of the smaller body (the asteroid) is set equal to zero. In this case, Eq.s (2.2) become

$$\begin{aligned}
\frac{\mathrm{d}^2\mathbf{r}_1}{\mathrm{d}t^2} &= -\mathcal{G}(m_0 + m_1)\frac{\mathbf{r}_1}{\|\mathbf{r}_1\|^3} \\
\frac{\mathrm{d}^2\mathbf{r}_2}{\mathrm{d}t^2} &= -\mathcal{G}m_0\frac{\mathbf{r}_2}{\|\mathbf{r}_2\|^3} + \mathcal{G}m_1\left(\frac{\mathbf{r}_1 - \mathbf{r}_2}{\|\mathbf{r}_1 - \mathbf{r}_2\|^3} - \frac{\mathbf{r}_1}{\|\mathbf{r}_1\|^3}\right)
\end{aligned} \tag{2.3}$$

where the first equation merely describes a two-body system consisting of P_0 and P_1 (called the primary body and the secondary body), and the second equation is the equation of motion of the massless body P_2 in the gravity fields of the Sun and the planet, representing the equations of motion of the restricted three-body problem. Note that the second equation of (2.3) can be regarded as a two-body system, composed of P_0 and P_2, plus a perturbation due to the existence of P_1. The first term of the perturbation, called direct perturbation, is related to the relative position of P_2 with respect to P_1, and the second term is called indirect perturbation.

According to the hypotheses on the motions of the primaries and of the massless body the restricted three-body problem can be further classified into: Circular restricted three-body problem (CRTBP hereafter): the motion of the primary and secondary bodies are circular around their barycenter; Elliptic restricted three-body problem (ERTBP hereafter): the motion of the primary and secondary bodies are elliptic around their barycenter; Planar CRTBP or ERTBP: the motion of P_2 lies in the orbital plane of P_0 and P_1; Spatial CRTBP or ERTBP: the motion of P_2 can move off the orbital plane of P_0 and P_1.

2.1.2 Hamiltonian representation of the CRTBP

My thesis will study the CRTBPs. Since the motions of P_0 (the Sun) and P_1 (the planet) are given, while the interest is to determine the motion of P_2 (the asteroid), in the following the indices of variables corresponding to the asteroid will be dropped (i.e. $\mathbf{r}_2$ will be $\mathbf{r}$ and P_2 will be P). The second equation of (2.3)

can be derived from the Hamiltonian:

$$\mathcal{H}(\mathbf{r},\mathbf{p}) := \frac{\|\mathbf{p}\|^2}{2} - \frac{\mathcal{G}m_0}{r} - \mathcal{G}m_1\left(\frac{1}{\|\mathbf{r}-\mathbf{r}_1\|} - \frac{\mathbf{r}\cdot\mathbf{r}_1}{\|r_1\|^3}\right) \tag{2.4}$$

where $\mathbf{r}$ is the (heliocentric) radius vector of P, $\mathbf{p}$ is its conjugate momentum; $r = \|\mathbf{r}\|$; $\mathbf{r}_1$ is the radius vector of P_1 defined by $\mathbf{r}_1 = r_1(\cos(n_1 t), \sin(n_1 t), 0)$ with constant r_1 and n_1 is defined according to Kepler's law; the angle $\lambda_1 := n_1 t$ will be called the true longitude of the planet. We choose the units of measure such that $\mathcal{G} = 1, m_0 = 1, r_1 = 1$, and the mass ratio of the system is denoted by $\varepsilon = m_1/m_0$. With these assumptions the Hamiltonian has the form:

$$\mathcal{H}(\mathbf{r},\mathbf{p}) = \mathcal{H}_0(r,\mathbf{p}) + \varepsilon\mathcal{H}_1(\mathbf{r},\mathbf{r}_1) \tag{2.5}$$

where

$$\mathcal{H}_0(\mathbf{r},\mathbf{p}) = \frac{\|\mathbf{p}\|^2}{2} - \frac{1}{r},$$

is integrable and corresponds to the Hamiltonian of Kepler problem composed of P_0 and P_1, while

$$\mathcal{H}_1(\mathbf{r},\mathbf{r}_1) = -\frac{1}{\|\mathbf{r}-\mathbf{r}_1\|} + \frac{\mathbf{r}\cdot\mathbf{r}_1}{\|r_1\|^3}$$

is a perturbation of $\mathcal{H}_0$, and ε determines its strength.

2.1.3 Orbital elements

The Keplerian orbits of P are identified by the orbital elements. By considering the elliptic motions of eccentricity $e \in (0,1)$, the central body P_0 is located at one of the foci of the Keplerian ellipse. In the orbital plane of P let us introduce a reference frame (q_1, q_2) with the axis q_1 pointing towards the pericenter of the orbit and the axis q_2 as in Fig. 2.1. The shape of the ellipse is described by the *semi-major axis* a and the eccentricity e. To describe the motion of the body we introduce the polar coordinates (r, f) on this plane. In such a way, r is the heliocentric distance from the body to the Sun (the right focus in the figure) and f is the polar angle called *true anomaly*. Another angle, called the *eccentric anomaly* E, is also defined: by introducing an auxiliary circle centered at the center of the ellipse and having a radius equal to the semi-major axis a. One projects the position of the body on the circle and the eccentric anomaly E is defined with respect to this circle, as shown in the right panel of the Figure. (2.1). The following classical relationships hold (see, for example, [Mor02])

$$r = a(1 - e\cos E), \quad \tan\left(\frac{f}{2}\right) = \sqrt{\frac{1+e}{1-e}}\tan\left(\frac{E}{2}\right).$$

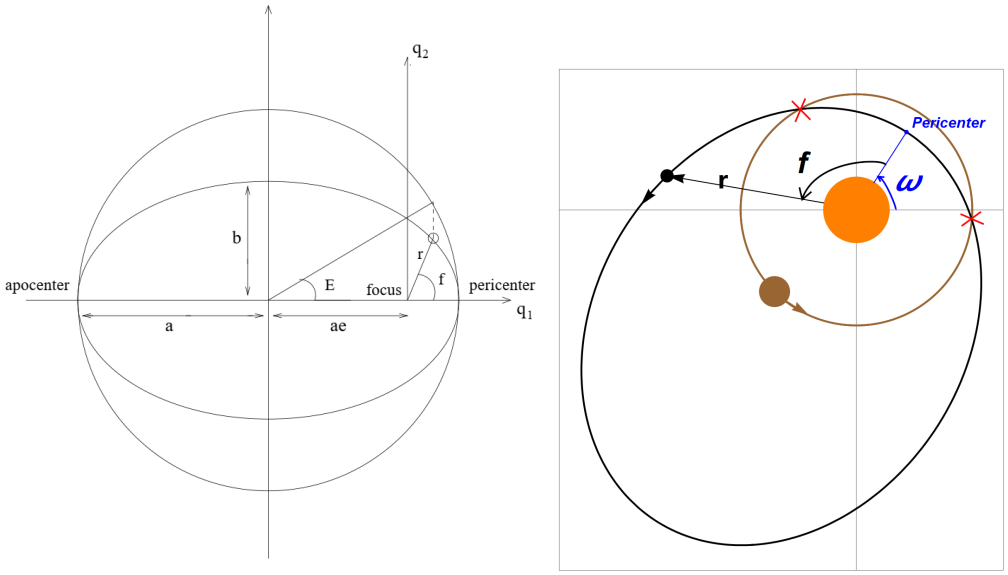

Figure 2.1: Keplerian orbit (the left panel is from [Mor02]): illustration of some orbital elements in the plane: semi-major axis a, eccentricity e, eccentric anomaly E, true anomaly f and argument of pericenter ω.

Note that for given a and e, there exists a one-to-one correspondence between E and f, and the (q_1, q_2)-coordinates of the body are given by

$$(q_1, q_2) = (a(\cos E - e), a\sqrt{1-e^2}\sin E).$$

Another angle, called *mean anomaly*, is defined by:

$$M = n(t - t_0),$$

where t_0 is the time of passage of P from the pericenter. The relationship between E and M is expressed by the *Kepler's equation*

$$E - e\sin E = M.$$

For $e \leq 0.66...$ a convergent series expressing the solution E as a function of M:

$$E = M + 2\sum_{s=1}^{\infty} \frac{1}{s} J_s(se)\sin(sM),$$

where

$$J_s(e) = \frac{1}{\pi}\int_0^{\pi} \cos(sE - se\sin E)dE,$$

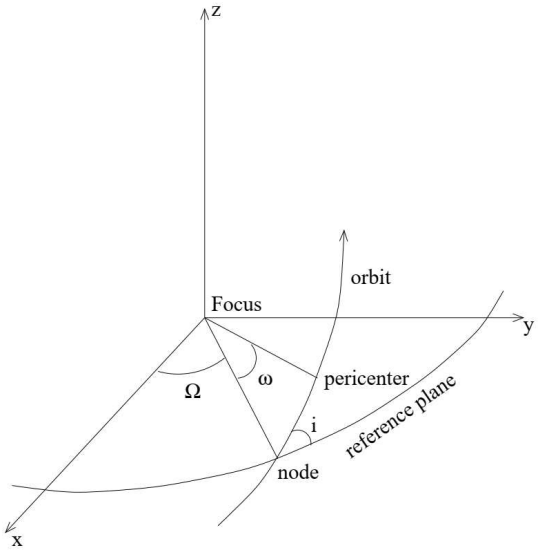

Figure 2.2: Orbital elements in the spatial coordinates.

is the Bessel function. If the Keplerian orbit is rotated, as shown in Fig. 2.1, then to identify the position of the Keplerian ellipse an addition angle ω is introduced, which is the angle between the pericenter and the q_1-axis (as shown in the right panel of Fig. 2.1), called the *argument of pericenter*.

The elements (a, e, ω, M) are enough to describe the motions in the planar case. However, to describe the spatial motions additional elements are needed. Fig. 2.2 illustrates the additional orbital elements for describing orbits in a reference inertial frame xyz. Note that the origin of the spatial reference frame is the position of the central body. An obvious element is the *inclination* i between the orbital plane and the xy reference plane, or more precisely, the angle between the angular momentum and the z-axis. For nonzero inclination the orbit has two intersection points with the xy plane called *nodes*: The *ascending node* where the body passes from below to above the xy-plane; the *descending node* where the body passes from above to below the xy-plane. The line determined by the two nodes is called *line of the nodes*. The *longitude of node* Ω is finally introduced by the angle from the x-axis to the ascending node. Note that when $i = 0$, the longitude of the node Ω is not well-defined and this case is reduced to the planar case; the argument of pericenter ω is defined by the angle between the pericenter and the ascending node.

There is a one-to-one correspondence between $(\mathbf{r}, \dot{\mathbf{r}}) = \left(x, y, z, \frac{dx}{dt}, \frac{dy}{dt}, \frac{dz}{dt}\right)$ and the orbital elements $a, e, i, \omega, \Omega, M$. For an elliptical orbit of the xy-plane with

pericenter on the x-axis, we have:

$$\mathbf{q} = (q_1, q_2, 0) = (a(\cos E - e), a\sqrt{1-e^2}\sin E, 0),$$
$$\frac{d\mathbf{q}}{dt} = \left(\frac{dq_1}{dt}, \frac{dq_2}{dt}, 0\right) = \left(-\frac{na\sin E}{1-e\cos E}, \frac{na\sqrt{1-e^2}\cos E}{1-e\cos E}, 0\right).$$

Then, for given values of i, ω, Ω we have:

$$(x, y, z) = R(i, \omega, \Omega)\mathbf{q}, \quad \left(\frac{dx}{dt}, \frac{dy}{dt}, \frac{dz}{dt}\right) = R(i, \omega, \Omega)\frac{d\mathbf{q}}{dt},$$

where the rotation matrix $R(i, \omega, \Omega)$ is defined by (see,[Mor02])

$$R(i, \omega, \Omega) = \begin{pmatrix} \cos\Omega\cos\omega - \sin\Omega\cos i\sin\omega & -\cos\Omega\sin\omega - \sin\Omega\cos i\cos\omega & \sin\Omega\sin i \\ \sin\Omega\cos\omega + \cos\Omega\cos i\sin\omega & -\sin\Omega\sin\omega + \cos\Omega\cos i\cos\omega & -\cos\Omega\sin i \\ \sin i\sin\omega & \sin i\cos\omega & \cos i \end{pmatrix}$$

2.1.4 Delaunay Variables

For small values ε of the planetary mass, Hamiltonian (2.5) of the CRTBP is a perturbation of the Hamiltonian of the Kepler problem. Therefore, it is convenient to express it as a function of the Delaunay variables, which are action-angle variables for the Kepler problem, and are defined by:

$$\begin{aligned} L &= \sqrt{\mathcal{G}m_0 a}, & l &= M \\ G &= L\sqrt{1-e^2}, & g &= \omega \\ H &= G\cos i, & h &= \Omega. \end{aligned}$$

The elements M, ω, Ω define the 'angle' variables, while the elements a, e, i define the 'action' variables. When the inclination and/or the eccentricity are equal to zero, the angles l, g, h are not well defined. To avoid this problem, the modified Delaunay variables are also introduced:

$$\begin{aligned} \Lambda &= L = \sqrt{a}, & \lambda &= l + g + h = M + \Omega + \omega \\ \Phi &= L - G = \sqrt{a}(1 - \sqrt{1-e^2}), & \varphi &= -g - h = -\omega - \Omega \\ \Gamma &= G - H = \sqrt{a(1-e^2)}(1-\cos i), & \gamma &= -h = -\Omega. \end{aligned}$$

The definition of the angle λ can be easily extended also when the eccentricity and/or the inclination are equal to zero while φ and γ are not well defined when Φ and Γ are equal to zero (corresponding to zero eccentricity and zero inclination). The Hamiltonian (2.4) of the CRTBP is then expressed using the modified Delaunay variables as:

$$\mathcal{H} = \mathcal{H}_0 + \varepsilon\mathcal{H}_1(\Lambda, \Phi, \Gamma, \lambda, \varphi, \gamma, \lambda_1), \tag{2.6}$$

where

$$\mathcal{H}_0 = -\frac{1}{2\Lambda^2} + n_1\Lambda_1,$$

and Λ_1 is an action conjugate to λ_1, introduced to make the Hamiltonian system autonomous.

Since in this thesis we study separately the planar and the spatial problems, we also recall that the modified Delaunay variables for the planar problem are:

$$\begin{aligned} &\Lambda = L = \sqrt{a}, && \lambda = l + g = M + \omega, \\ &\Phi = L - G = \sqrt{a}(1 - \sqrt{1-e^2}), && \varphi = -g = -\omega, \end{aligned}$$

and the Hamiltonian of the planar CRTBP has the form:

$$\mathcal{H} = \mathcal{H}_0 + \varepsilon\mathcal{H}_1(\Lambda, \Phi, \lambda, \varphi, \lambda_1). \tag{2.7}$$

Note that the expression of the perturbation $\mathcal{H}_1$ is not explicitly given in these variables. Therefore we consider its Fourier expansion

$$\mathcal{H}_1 = \sum_{(k,m,l)\in\mathbb{Z}^3} c_{k,m,l}(\Lambda, \Phi, \Gamma) e^{i[k\lambda + (k+m-l)\varphi + l\gamma + m\lambda_1]}, \tag{2.8}$$

which can be computed using classical expressions, which are valid for small values of e and i, or using numerical methods. Note the peculiar dependence of the coefficients of $\lambda, \varphi, \gamma, \lambda_1$ on the integers k, m, l, due to the well-known D'Alembert rules, as well as the relation

$$c_{k,m,l} = c_{-k,-m,-l}, \tag{2.9}$$

between the coefficients. Moreover, the complex Fourier expansion (2.8), which is reformulated as a real Fourier expansion, contains only cosine terms. Both properties are consequences of geometric symmetries of the perturbing function: the first one is due to the invariance by rotation around the vertical axis, and the second one is due to the invariance of $\mathcal{H}_1$ with respect to the simultaneous reflection of all the angles.

2.2 Hamiltonian Perturbation Theory

Since in this thesis we will study the effect of close encounters on the resonant dynamics of the CRTBP, in this chapter we recall the basic tools of the Hamiltonian perturbation theory which allow to define and represent the resonant normal forms. The main tool will be the Lie method, while we will describe in a subsequent chapter the method of adiabatic invariants.

2.2.1 Nearly-Integrable Hamiltonian Systems

A Hamiltonian system is said to be nearly-integrable if its Hamilton function can be represented in the form:

$$\mathcal{H}(J,\psi) = \mathcal{H}_0(J) + \varepsilon\mathcal{H}_1(J,\psi)$$

where ε is a small parameter and (J,ψ) are action-angle variables which are canonically conjugate and are defined in a set of $\mathcal{D}\times\mathbb{T}^n$, where $\mathcal{D}\subset\mathbb{R}^n$ is open. $\mathcal{H}_0$ is identified as the integrable part of the Hamiltonian and $\mathcal{H}_1$ as the perturbation, with ε measuring its strength. Indeed, the Hamiltonian of the restricted three-body problem possesses such a form when it is represented with the modified Delaunay variables (see Subsection 2.1.4), and when the parameter ε represents the ratio between the mass of a planet of the Solar system and the mass of the Sun, for instance, $\varepsilon \approx 0.001, 0.0000515139, 0.000003003$ for Sun-Jupiter, Sun-Neptune and Sun-Earth systems, respectively.

For $\varepsilon = 0$, the Hamiltonian system is integrable, and its flow is easily represented by:

$$\begin{aligned} J(t) &= J(0),\\ \psi(t) &= \omega(J(0))t + \psi(0), \end{aligned}$$

where $\omega(J) := \partial_J\mathcal{H}_0$ is called *frequency map*. When $\varepsilon \neq 0$ the action variables are no longer first integrals, and the perturbed flow doesn't have an explicit solution (except possibly for specific initial conditions).

The first goal of Hamiltonian perturbation theory is to define a close-to-the-identity canonical transformation

$$(J,\psi) = \mathcal{C}_1(J^{(1)},\psi^{(1)}) \tag{2.10}$$

conjugating the Hamiltonian $\mathcal{H}$ to:

$$\mathcal{H}^{(1)}(J^{(1)},\psi^{(1)}) = \mathcal{H}_0(J^{(1)}) + \varepsilon\tilde{\mathcal{H}}_1(J^{(1)}) + \varepsilon^2\mathcal{H}_2(J^{(1)},\psi^{(1)}) \tag{2.11}$$

having the property that the dependence on the angles appears at order $\mathcal{O}(\varepsilon^2)$ (and not at order $\mathcal{O}(\varepsilon)$, as for the original Hamiltonian). The Hamiltonian (2.11) is called non-resonant normal form, and the transformation (2.10) is called averaging transformation.

The existence of the averaging transformation is subject to hypotheses on the Hamiltonian $\mathcal{H}_0$, on the domain $\mathcal{D}$ of the action variables (more details will be given in the following), and moreover the perturbing parameter ε must be suitably small. A more subtle question, which is treated within the celebrated KAM and

Nekhoroshev theories, concern the possibility of iterating the averaging transformation, thus constructing a canonical transformation conjugating $\mathcal{H}$ to:

$$\begin{aligned}\mathcal{H}^{(s)}(J^{(s)},\psi^{(s)}) =&\mathcal{H}_0(J^{(s)}) + \varepsilon\tilde{\mathcal{H}}_1(J^{(s)}) + \varepsilon^2\tilde{\mathcal{H}}_2(J^{(s)}) + \cdots + \varepsilon^s\tilde{\mathcal{H}}_s(J^{(s)}) \\ &+ \varepsilon^{s+1}\mathcal{H}_{s+1}(J^{(s)},\psi^{(s)})\end{aligned}$$

for the largest possible integer s.

In this thesis, since we are testing the limits of the averaging method close to gravitational singularities, we are interested in determining the boundary within which at least the first step $\mathcal{C}_1$ of the iteration can be defined.

2.2.2 Lie Series Method

The Lie method provides a classical way to construct the averaging transformation (see, for example, [Gior22]) as the Hamiltonian flow at time ε of a suitable generating function χ. To describe the Lie method, we first represent the Hamiltonian flow defined by a Hamiltonian χ at time ε, in powers of ε itself. By indicating with:

$$\mathcal{L}_\chi f = \{f,\chi\}$$

the Lie derivative of a function f with respect to χ, the solution of the Hamilton equations of χ at time ε, with initial conditions $(J(0),\psi(0)) = (\tilde{J},\tilde{\psi})$, is represented in the form:

$$J(\varepsilon) = \exp(\varepsilon\mathcal{L}_\chi)J\Big|_{\tilde{J},\tilde{\psi}}, \quad \psi(\varepsilon) = \exp(\varepsilon\mathcal{L}_\chi)\psi\Big|_{\tilde{J},\tilde{\psi}}$$

where the Lie series operator $\exp(\varepsilon\mathcal{L}_\chi)$ is utilized:

$$\exp(\varepsilon\mathcal{L}_\chi) = \sum_{s\geq 0}\frac{\varepsilon^s}{s!}\mathcal{L}_\chi.$$

Explicitly the solution of the Hamilton equations is

$$\begin{aligned}J(\varepsilon) &= \tilde{J} + \varepsilon\mathcal{L}_\chi J\Big|_{\tilde{J},\tilde{\psi}} + \frac{\varepsilon^2}{2}\mathcal{L}_\chi^2 J\Big|_{\tilde{J},\tilde{\psi}} + \cdots, \\ \psi(\varepsilon) &= \tilde{\psi} + \varepsilon\mathcal{L}_\chi\psi\Big|_{\tilde{J},\tilde{\psi}} + \frac{\varepsilon^2}{2}\mathcal{L}_\chi^2\psi\Big|_{\tilde{J},\tilde{\psi}} + \cdots.\end{aligned}$$

The nearly-integrable Hamiltonian $\mathcal{H}$ is conjugate to

$$\tilde{\mathcal{H}}(\tilde{J},\tilde{\psi}) := \mathcal{H}\circ\exp(\varepsilon\mathcal{L}_\chi)(\tilde{J},\tilde{\psi}).$$

The following celebrated exchange lemma (see [Gior22]) allows to easily expand the conjugate Hamiltonian in power series of the perturbing parameter ε:

Lemma 1. *Given a generating function $\chi(J,\psi)$ and a function $f(J,\psi)$, the following equality holds true:*

$$f(J,\psi)\Big|_{J=\exp(\varepsilon\mathcal{L}_\chi)\tilde{J},\psi=\exp(\varepsilon\mathcal{L}_\chi)\tilde{\psi}} = \exp(\varepsilon\mathcal{L}_\chi)f\Big|_{J=\tilde{J},\psi=\tilde{\psi}}.$$

This lemma indicates that we can just apply the Lie series operator to the Hamiltonian and then replace the old variables with the new variables, instead of utilizing the canonical transformation and then expanding it.

By the exchange lemma, we have

$$\exp(\varepsilon\mathcal{L}_\chi)\mathcal{H} = \mathcal{H}_0 + \varepsilon\left(\mathcal{H}_1 + \{\mathcal{H}_0,\chi\}\right) + \mathcal{O}(\varepsilon^2). \tag{2.12}$$

Let us now return to the basic goal of the perturbation theory defined above. Motivated by Eq. (2.12), we look for a generating function $\chi(J,\psi)$ solving the following equation

$$\mathcal{H}_1 + \{\mathcal{H}_0,\chi\} = \tilde{\mathcal{H}}_1, \tag{2.13}$$

with $\tilde{\mathcal{H}}_1$ dependent only on the variables J. To solve Eq. (2.13) we expand $\mathcal{H}_1$ and χ in Fourier series with respect to ψ

$$\begin{aligned}\mathcal{H}_1(J,\psi) &= \sum_{k\in\mathbb{Z}^n} c_k(J)\exp(ik\cdot\psi), \\ \chi(J,\psi) &= \sum_{k\in\mathbb{Z}^n} d_k(J)\exp(ik\cdot\psi),\end{aligned} \tag{2.14}$$

and then by solving Eq. (2.13) term by term we find:

$$d_k(J) = -i\frac{c_k(J)}{k\cdot\omega(J)} \quad \forall k\neq 0, \tag{2.15}$$

where $\omega(J) := \frac{\partial\mathcal{H}_0}{\partial J}(J)$ is the frequency map. This leads to:

$$\tilde{\mathcal{H}}_1(J) = c_0(J). \tag{2.16}$$

Since there are no conditions on $d_0(J)$, one sets $d_0(J)=0$.

Assuming that the Fourier series defined by the coefficients d_k as in Eq. (2.15) is analytic in the open domain $\mathcal{D}$ of the actions, for suitably small ε the Hamiltonian flow of χ is close to the identity and conjugates the original Hamiltonian to the non-resonant normal form:

$$\tilde{\mathcal{H}}(J,\psi) = \mathcal{H}_0(J) + \varepsilon c_0(J) + \mathcal{O}(\varepsilon^2),$$

where we drop the symbol˜for simplicity. If we neglect the remainder of $\mathcal{O}(\varepsilon^2)$, we remain with an integrable Hamiltonian dependent only on the new action variables.

From Eq. (2.15) one understands that a necessary condition for the definition of the coefficients $d_k(J)$ for $J \in \mathcal{D}$ is that in $\mathcal{D}$ there are no solutions to the equation

$$k \cdot \omega(J) = 0, \tag{2.17}$$

for all $k \neq 0$ such that:

$$\sup_{J \in \mathcal{D}} |c_k(J)| \geq \varepsilon.$$

In fact, if $|c_k(J)| < \varepsilon$ for all $J \in \mathcal{D}$, the term $\varepsilon c_k \exp(ik \cdot \psi)$ is a small term of order ε^2 and can be relegated into the remainder. Correspondingly, for this k we define $\chi_k = 0$.

The relation (2.17) defines a resonance, and in a neighborhood of the values J satisfying (2.17) the non-resonant normal form is not conjugate to the original Hamiltonian. However, it remains the possibility to define a resonant normal form, depending on the linear combination of the angles $k \cdot \psi$. This is precisely the case that we have in the mean motion resonances (MMRs), which are the object of study of the thesis, So, in the next Section, we will describe in more detail the resonant case.

2.2.3 The resonant normal form

For any $\kappa \in \mathbb{Z}^n \backslash \{0\}$, define the resonant manifold:

$$\mathcal{R}_\kappa := \{J \in \mathcal{D} : \kappa \cdot \omega(J) = 0\}.$$

As already remarked, the coefficient d_κ defined in Eq. (2.15) is singular in a neighborhood of $\mathcal{R}_\kappa$, and therefore one proceeds to define a resonant averaging corresponding to set d_k as in Eq. (2.15) for all the integer vectors k which are not parallel to κ, and

$$d_k = 0, \quad \text{if} \quad k \in \langle \kappa \rangle,$$

where $\langle \kappa \rangle$ denotes the one-dimensional sub-lattice of $\mathbb{Z}^n$ containing κ. Correspondingly, the averaged Hamiltonian would be of the form

$$\begin{aligned} \tilde{\mathcal{H}}(J, \psi) &= \mathcal{H}_0(J) + \varepsilon \tilde{\mathcal{H}}_1(J, \psi) + \mathcal{O}(\varepsilon^2) \\ &= \mathcal{H}_0(J) + \varepsilon \sum_{k \in \langle \kappa \rangle} c_k(J) \exp(ik \cdot \psi) + \mathcal{O}(\varepsilon^2). \end{aligned} \tag{2.18}$$

Therefore, not all the angles are eliminated at order ε, and the dynamics of the resonant normal form is more complex than the dynamics of the non-resonant one. If $\bar{k} \in \mathbb{Z}^n$ is such that

$$\langle \kappa \rangle = \{k \in \mathbb{Z}^n : k = n\bar{k}, n \in \mathbb{Z}\},$$

it is convenient to introduce the resonant angle:

$$\sigma = \bar{k} \cdot \psi,$$

and correspondingly there is a linear canonical transformation:

$$\begin{pmatrix} \sigma \\ \phi_1 \\ \ddots \\ \phi_{n-1} \end{pmatrix} = \Gamma \begin{pmatrix} \psi_1 \\ \psi_2 \\ \ddots \\ \psi_n \end{pmatrix},$$
$$\begin{pmatrix} S \\ F_1 \\ \ddots \\ F_{n-1} \end{pmatrix} = \Gamma^{-T} \begin{pmatrix} J_1 \\ J_2 \\ \ddots \\ J_n \end{pmatrix},$$

with the matrix Γ having integer entries and $\det(\Gamma) = 1$, so that

$$\mathcal{H}_0(J) + \varepsilon \sum_{k \in \langle \kappa \rangle} c_k \exp[ik \cdot \psi]$$

is conjugate to the resonant normal form Hamiltonian:

$$\tilde{\mathcal{H}}_0(S, F_1, \cdots, F_{n-1}) + \varepsilon \tilde{\mathcal{H}}_1(S, \sigma, F_1, \cdots, F_{n-1}). \tag{2.19}$$

The Hamiltonian flow of the resonant normal form (2.19) is such that the actions F_j are first integrals. Therefore, for any fixed values of $F_1, \cdots, F_{n-1}$, the variables S, σ satisfy the Hamilton equations of the one degree of freedom reduced Hamiltonian

$$\widehat{\mathcal{H}}(S, \sigma; F_1, \cdots, F_{n-1}) = \tilde{\mathcal{H}}_0(S, F_1, \cdots, F_{n-1}) + \varepsilon \tilde{\mathcal{H}}_1(S, \sigma, F_1, \cdots, F_{n-1}),$$

which is the kind of normal forms that are obtained for the MMRs of the planar CRTBP.

The resonant case described above is defined by a single resonant combination $\kappa \cdot \psi$ of the angles ψ. Instead, we have an higher-dimensional resonance when the domain $\mathcal{D}$ intersects the resonant set:

$$\mathcal{R}_L = \{I \in \mathcal{D} : k \cdot \omega(I) = 0, \forall k \in L\},$$

where $L \subseteq \mathbb{Z}^n$ is a d-dimensional lattice, i.e. there exist linearly independent vectors $(\nu_1, \nu_2, \cdots, \nu_d) \in \mathbb{Z}^n$ which span L:

$$L = \{k \in \mathbb{Z}^n : \exists n_1, n_2, \cdots, n_d \in \mathbb{Z} \text{ with } k = \sum_{j=1}^{d} n_j \nu_j\}.$$

In such a case, one sets equal to zero all the coefficients d_k with $k \in L$, and the resonant normal form is:

$$\mathcal{H} = \mathcal{H}_0 + \varepsilon \sum_{k \in L} c_k(J) \exp(ik \cdot \psi) + \mathcal{O}(\varepsilon^2).$$

Correspondingly, there is a linear canonical transformation:

$$\begin{pmatrix} \sigma_1 \\ \ddots \\ \sigma_d \\ \phi_1 \\ \ddots \\ \phi_{n-d} \end{pmatrix} = \Gamma\psi, \quad \begin{pmatrix} S_1 \\ \ddots \\ S_d \\ F_1 \\ \ddots \\ F_{n-d} \end{pmatrix} = \Gamma^{-T} \begin{pmatrix} J_1 \\ \ddots \\ J_n \end{pmatrix}, \tag{2.20}$$

such that $\mathcal{H}_0 + \varepsilon \sum_{k \in L} c_k(J) \exp(ik \cdot \psi)$ is conjugate to

$$\tilde{\mathcal{H}}_0(S, F) + \varepsilon \tilde{\mathcal{H}}_1(S, F, \sigma_1, \cdots, \sigma_d) \tag{2.21}$$

this will be precisely the case of the MMR normal forms of the spatial CRTBP, which will depend on two angles (afterwards denoted by σ and α). The dynamics of the Hamiltonian system corresponding to the resonant normal form (2.21) is by far more complicated than the dynamics of the normal form (2.19). Indeed, even if the actions $F_1, \cdots, F_{n-d}$ are first integrals, the Hamiltonian (2.21) is not integrable for $d \geq 2$.

2.3 The MMRs of the CRTBP

The aforementioned general construction of resonant normal forms can be applied to the CRTBP. We start from the Hamiltonian of the spatial circular restricted 3-body problem (see Eq. (2.6)):

$$\mathcal{H} = \mathcal{H}_0(\Lambda, \Lambda_1) + \varepsilon \mathcal{H}_1(\Lambda, \Phi, \Gamma, \lambda, \varphi, \gamma, \lambda_1).$$

Since the action variables are $J = (\Lambda, \Phi, \Gamma, \Lambda_1)$, the frequency map is

$$\begin{aligned}\omega = \frac{\partial \mathcal{H}_0}{\partial J} &= \left(\frac{\partial \mathcal{H}_0}{\partial \Lambda}, \frac{\partial \mathcal{H}_0}{\partial \Phi}, \frac{\partial \mathcal{H}_0}{\partial \Gamma}, \frac{\partial \mathcal{H}_0}{\partial \Lambda_1}\right) \\ &= \left(\frac{1}{\Lambda^3}, 0, 0, n_1\right).\end{aligned}$$

A $p : q$ MMR is defined by the lattice generated by the linearly independent integer vectors:

$$\begin{aligned}\underline{\nu}^{(1)} &= (q, 0, 0, -p), \\ \underline{\nu}^{(2)} &= (0, 1, 0, 0), \\ \underline{\nu}^{(3)} &= (0, 0, 1, 0),\end{aligned}$$

so that we have:

$$L = \text{span}\{\underline{\nu}^{(1)}, \underline{\nu}^{(2)}, \underline{\nu}^{(3)}\} = \left\{k \in \mathbb{Z}^4 : \frac{k_1}{k_4} = -\frac{q}{p}\right\}.$$

But, different from the generic quasi-integrable Hamiltonian systems, the perturbing function $\mathcal{H}_1$ of the CRTBP satisfies the D'Alembert rules, and therefore we can restrict the definition of L to the vectors $k \in \mathbb{Z}^4$ such that:

$$k_1 - k_2 - k_3 + k_4 = 0,$$

namely, the definition of L will be

$$L = \{k \in \mathbb{Z}^4 : k_1 p + k_4 q = 0 \text{ and } k_1 - k_2 - k_3 + k_4 = 0\},$$

which is a 2-dimensional lattice of $\mathbb{Z}^4$. Correspondingly, the resonant manifold is

$$\begin{aligned}\mathcal{R}_L &= \{(\Lambda, \Phi, \Gamma, \Lambda_1) : k \cdot \omega = 0 \text{ for all } k \in L\} \\ &= \left\{(\Lambda, \Phi, \Gamma, \Lambda_1) : \Lambda = \left(\frac{q}{p n_1}\right)^{1/3}\right\},\end{aligned}$$

and we can proceed by introducing the action-angle variables (2.20) adopted for the specific resonance, having two slow angles (which are denoted by σ, α) and two fast angles (which are denoted by ν, θ) [Mor02, Sail16].

Remark: The integrable part $\mathcal{H}_0$ depends only on the action Λ and Λ_1, which is due to the well-known degeneracy of the Kepler problem, namely, having the 2 frequencies $\dot{\omega} = 0$ and $\dot{\Omega} = 0$ for all the motions [Pin23].

2.3.1 Resonant action-angle variables

In this subsection we introduce the action-angle variables adapted to an external $p : q$ resonance of order 1, which will be used in this thesis for the implementation of the averaging method.

Be referring to the notation of the previous subsections, for the spatial CRTBP the angles σ_1 and σ_2 will be denoted by σ and α, while ϕ_1 and ϕ_2 will be denoted by ν and θ.

Let us therefore consider the canonical transformation:

$$\begin{pmatrix} \sigma \\ \alpha \\ \nu \\ \theta \end{pmatrix} = \begin{pmatrix} q & q-p & 0 & -p \\ 0 & 1 & -1 & 0 \\ -1 & 0 & 0 & 0 \\ 0 & 0 & 0 & 1 \end{pmatrix} \begin{pmatrix} \lambda \\ \varphi \\ \gamma \\ \lambda_1 \end{pmatrix}, \tag{2.22a}$$

$$\begin{pmatrix} S \\ A \\ N \\ \Theta \end{pmatrix} = \begin{pmatrix} 0 & 1 & 1 & 0 \\ 0 & 0 & p-q & 0 \\ p-q & q & q & 0 \\ 0 & p & p & 1 \end{pmatrix} \begin{pmatrix} \Lambda \\ \Phi \\ \Gamma \\ \Lambda_1 \end{pmatrix}. \tag{2.22b}$$

Remarks:

- Here we only list the resonant action-angle variables for the spatial problem. For the planar case, analogous variables are defined, but of course without the couple of variables Γ and γ, correspondingly there are no resonant variables A and α. As a result, for the planar problem, we just delete the third rows and the third columns of the coefficient matrices. In Chapter 3 the resonant variables for the planar circular restricted 3-body problem will be re-introduced for completeness.

- Even if the averaged Hamiltonian will depend on both the angles σ and α, they have a different meaning. In fact, the angle σ is the critical angle of the resonance: it is the angle $q\lambda - p\lambda_1$ plus the angle $(q-p)\varphi$ which is necessary for $\sigma = q\lambda - p\lambda_1 + (q-p)\varphi$ to be invariant with respect to rotations of the axis of the nodes, and has the given expression in such a way to respect the D'Alembert rules.

- The angle σ, related to the MMR, along with its conjugate action variable S will be called resonant variables. For the spatial problem, the action-angle variables (A, α) are called secular variables.

- Since we only consider the first-order external $p : q$ mean motion resonances, the matrix in Eq. (2.22) has integer entries and its determinant is $q - p = 1$.

Therefore, it defines an invertible transformation on the torus $\mathbb{T}^4$. For mean motion resonances of larger order, one usually considers matrices of rational numbers (see [LiuGuzzo25] for how to define them and see [Mor02] and [MilB98] for similar ones).

- The angle α is a secular one (the variation of both α and its conjugate action A are proportional to ε).
- The angles $\nu = -\lambda$ and $\theta = \lambda_1$ are fast angles of the problem. Moreover, the Hamiltonians of the spatial and planar restricted three-body problems depend on the fast angles ν and θ only through their sum $\nu + \theta$, which is a fast angle as well: $\nu + \theta = -\lambda + \lambda_1$.

In these canonical variables, the Hamiltonian of circular restricted 3-body problem will depend on the actions variables S, A, N, Θ, on the critical angle σ, on the secular angle α and on the summation of the angles $\nu + \theta$. The integrable part of the Hamiltonian is:

$$\widehat{\mathcal{H}}_0(S, A, N, \Theta) := -\frac{1}{2(qS - N)^2} + n_1(-pS + \Theta), \tag{2.23}$$

while the perturbation $\widehat{\mathcal{H}}_1$, which depends on σ, α and $\nu + \theta$, will be represented as a real Fourier series with respect to the fast angle $\nu + \theta$:

$$\begin{aligned}\widehat{\mathcal{H}}_1(S, A, N, \sigma, \alpha, \nu + \theta) =& c_0(S, A, N, \sigma, \alpha) + \sum_{k=1}^{\infty} c_k(S, A, N, \sigma, \alpha) \cos(k(\nu + \theta)) \\ &+ \sum_{k=1}^{\infty} s_k(S, A, N, \sigma, \alpha) \sin(k(\nu + \theta)),\end{aligned} \tag{2.24}$$

where using basic Fourier theory $c_0(S, A, N, \sigma, \alpha)$ is the Fourier average of the perturbing function along $\nu + \theta$:

$$c_0(S, A, N, \sigma, \alpha) = \frac{1}{2\pi} \int_0^{2\pi} \widehat{\mathcal{H}}_1(S, A, N, \sigma, \alpha, \nu + \theta) \mathrm{d}(\nu + \theta), \tag{2.25}$$

while the other coefficients are:

$$c_k(S, A, N, \sigma, \alpha) = \frac{1}{\pi} \int_0^{2\pi} \widehat{\mathcal{H}}_1(S, A, N, \sigma, \alpha, \nu + \theta) \cos[k(\nu + \theta)] \mathrm{d}(\nu + \theta), \tag{2.26}$$

$$s_k(S, A, N, \sigma, \alpha) = \frac{1}{\pi} \int_0^{2\pi} \widehat{\mathcal{H}}_1(S, A, N, \sigma, \alpha, \nu + \theta) \sin[k(\nu + \theta)] \mathrm{d}(\nu + \theta). \tag{2.27}$$

Indeed, expansion (2.24), whose coefficients are obtained by integrating the perturbing function over only one angle, is more regular than the triple Fourier series (2.8) when the possibility of collisions of P with P_1 are considered. The efficiency of the Fourier representation (2.24) in this case will be verified in the next chapters. The formulas here are related to the spatial problem; for the planar problem we just ignore the secular variables (A, α).

The coefficient $c_0(S, A, N, \sigma, \alpha)$ in Eq. (2.25) is particularly important, since it provides the perturbation of the averaged Hamiltonian. In the literature it has been numerically computed, following, for example, Schubart's method (see [Schu64, Schu66, Moons94]). In particular, in the papers ([Bea94, Tho98]) c_0 had been numerically computed also for large values of the eccentricity outside a curve of the resonant phase-plane (σ, S), the 'singular set' defined in next chapter, where collisions of P with P_1 may occur.

2.3.2 Resonant normal form Hamiltonian

After averaging the fast angles from the Hamiltonian $\widehat{\mathcal{H}}_0 + \varepsilon\widehat{\mathcal{H}}_1$ using a canonical transformation as explained in previous subsections, we obtain the resonant normal form Hamiltonian:

$$\begin{aligned}\widehat{\mathcal{H}}(S, A, N, \Theta, \sigma, \alpha) &= \widehat{\mathcal{H}}_0(S, A, N, \Theta) + \frac{\varepsilon}{2\pi}\int_0^{2\pi} \widehat{\mathcal{H}}_1(S, A, N, \sigma, \alpha, \nu + \theta)\mathrm{d}(\nu + \theta),\\ &= \widehat{\mathcal{H}}_0(S, A, N, \Theta) + \varepsilon\widehat{\mathcal{H}}_1^{Res}(S, A, N, \sigma, \alpha),\end{aligned}$$

where $\widehat{\mathcal{H}}^{Res} = c_0(S, A, N, \sigma, \alpha)$. Since N and Θ are first integrals for the Hamilton equations of $\widehat{\mathcal{H}}$, the normal form Hamiltonian can be studied as a system of two degrees of freedom, depending parametrically on the values of N, Θ. However, one immediately realizes that the value of Θ, defined by the auxiliary variable Λ_1, is of no interest, while the value of N is important for studying the resonant dynamics of the problem. For the spatial case, we have:

$$\begin{aligned}N &= (p - q)\Lambda + q\Phi + q\Gamma,\\ &= \sqrt{a}\left(p - q\sqrt{1 - e^2}\cos(i)\right),\end{aligned} \tag{2.28}$$

and for the planar case

$$N = \sqrt{a}\left(p - q\sqrt{1 - e^2}\right). \tag{2.29}$$

Since N is related to the semi-major axis a, the eccentricity e and the inclination i, for suitable values of N we may obtain so large values of eccentricity that close

encounters and collisions of P with P_1 become possible. For the resonances that we consider in this thesis (1:2 and 5:6 resonance), we only study the averaged Hamiltonian for negative values of N. Indeed, there exists a critical value $N_c < 0$ of N for which if the value of N is smaller than N_c there are no collisions and if the value of N is larger than or equal to N_c we can have crossing orbits or tangential orbits.

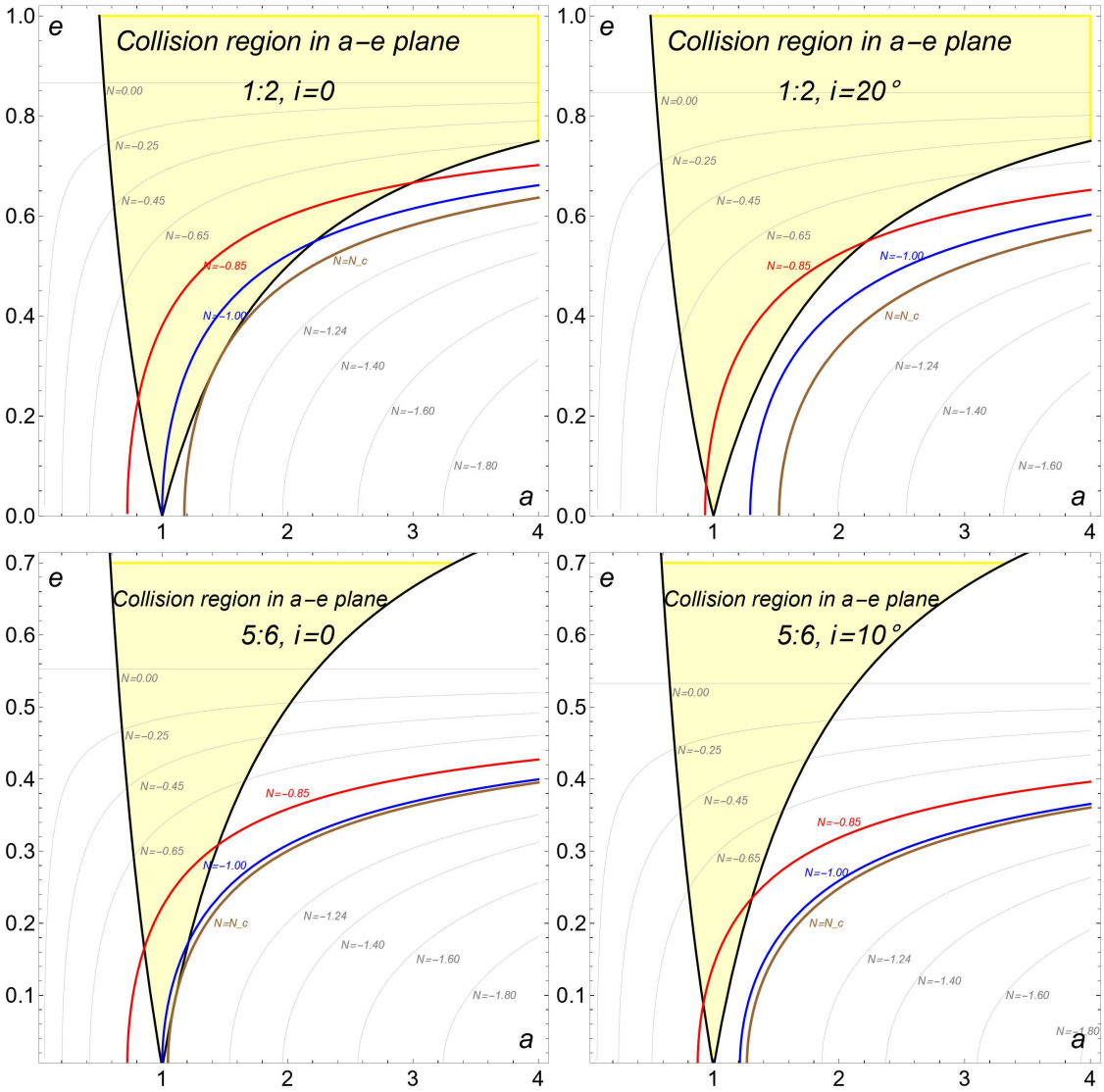

Figure 2.3: Representation in the a-e plane of different level sets of the action $N = \sqrt{a}\left(p - q\sqrt{1-e^2}\cos(i)\right)$ defined for the 1:2 and 5:6 resonance for different inclinations. Please see text for more details

For example, in Fig. 2.3 we represent the level curves of N for the 1:2 and 5:6 MMR (the cases considered in this thesis), for fixed values of the inclination i. We also represent the curves $a(1+e)=1$ and $a(1-e)=1$ corresponding to the values of a, e for which the apocenters and pericenters are equal to 1. Only when a, e belong to the shaded area (defined by $a(1-e) \leq 1 \leq a(1+e)$) the orbit of P may intersect or be tangent to the orbit of P_1. For any given value of i, we see that there is a critical value $N_c(i)$ for which the level curve of the first integral N is tangent to the curve of pericenters. Moreover, by changing the inclinations i, the minimum value of $N_c(i)$ is obtained for $i=0$. Therefore, we have $N_c := N_c(0)$.

The top panels of the Fig. 2.3 illustrate the level curves for the 1:2 resonance and for $i=0$ (left panel) and $i=20^\circ$ (right panel). The bottom two panels depict the level curves for 5:6 resonance and for $i=0$ (left panel) and $i=10^\circ$ (right panel). In all the panels, the curves of pericenters $a(1-e)=1$ and of apocenters $a(1+e)=1$ are represented in black. The region $a(1-e) \leq 1 \leq a(1+e)$, which contains the values of semi-major axis and eccentricity of the orbits which possible intersect or are tangent to the orbit of P_1, is represented by the yellow area.

In the top panels of Fig. 2.3, the level curves corresponding to some sample values of N are highlighted with colors: the red curve corresponds to $N=-0.85$, the blue curve $N=-1.00$ and the brown curve identifies the critical value $N_c \simeq -1.08525$. Notice that the critical value is obtained for $i=0$. The level curves for the other values are represented in gray. For the 5:6 resonance, in the bottom panels we represent the level curves corresponding to $N=-0.85$, $N=-1.00$, and to the critical value for this resonance $N_c \simeq -1.02276$. From left panels of Fig. 2.3, we appreciate that there is a critical value N_c of the first integral for the planar problem (i.e. zero inclination $i=0$), such that the orbits with $N < N_c$ do not intersect and are not tangent to the orbit or P_1.

2.4 Regularizing the Circular Restricted 3-Body Problems

In this thesis we will present many numerically computed orbits of both the planar and circular restricted three-body problems, which are obtained by integrating the equations of motion of the problems regularized with the Levi-Civita (for the planar problem) or Kustaanheimo-Stiefel (for the spatial problem) regularizations. In the first subsection we define the CRTBP in the synodic reference frame; in the next subsections we define the Levi-Civita and Kustaanheimo-Stiefel regularizations. For more detail we refer to [Szeb67].

2.4.1 Equations of Motion of the CRTBP in the Synodic Coordinate System

Since the massless body doesn't affect the two-body system, its motion can be studied in a uniformly rotating frame defined as follows. Fixing the origin of the reference frame at the barycenter of P_0 and P_1, and represent the motions of P_0 and P_1 by:

$$\begin{aligned}\bar{\mathbf{r}}_0 &= (X_0, Y_0, Z_0) = (-\mu\cos(n_1 t), -\mu\sin(n_1 t), 0),\\ \bar{\mathbf{r}}_1 &= (X_1, Y_1, Z_1) = ((1-\mu)\cos(n_1 t), (1-\mu)\sin(n_1 t), 0),\end{aligned}$$

where the unit distance is assumed equal to $\|P_0 - P_1\|$, $\mu := \frac{m_1}{m_0+m_1} = \frac{\varepsilon}{1+\varepsilon}$ is the reduced mass and n_1 is the angular velocity of the primaries. Let the coordinates of P in the barycentric system be denoted by (X, Y, Z). The equations of motion for P are

$$\begin{aligned}\ddot{X} &= m_0\frac{X_0 - X}{r_0^3} + m_1\frac{X_1 - X}{r_1^3},\\ \ddot{Y} &= m_0\frac{Y_0 - Y}{r_0^3} + m_1\frac{Y_1 - Y}{r_1^3},\\ \ddot{Z} &= m_0\frac{Z_0 - Z}{r_0^3} + m_1\frac{Z_1 - Z}{r_1^3},\end{aligned} \tag{2.30}$$

where $\mathcal{G}$ is assumed to be equal to 1, and $r_0 = \|P - P_0\|, r_1 = \|P - P_1\|$ are the distances from P to P_0 and P_1, respectively.

Now let's consider the rotating system with the origin at the barycenter of P_0 and P_1 rotates at a uniform rate n_1. In the new system, the x-axis is chosen such that two primaries P_0 and P_1 have fixed positions $(x_0, y_0, z_0) = (-\mu, 0, 0)$ and $(x_1, y_1, z_1) = (1-\mu, 0, 0)$, respectively. The expression of distances r_0 and r_1 will be

$$\begin{aligned}r_0 &= \sqrt{(x+\mu)^2 + y^2 + z^2},\\ r_1 &= \sqrt{(x-1+\mu)^2 + y^2 + z^2},\end{aligned}$$

where (x, y, z) are the coordinates of P in the rotating system.

By introducing the rotation matrix:

$$\mathcal{R}(\alpha) := \begin{pmatrix}\cos\alpha & -\sin\alpha & 0\\ \sin\alpha & \cos\alpha & 0\\ 0 & 0 & 1\end{pmatrix},$$

the relation between the coordinates in the sidereal and the synodic system is given

by:

$$\begin{pmatrix} X \\ Y \\ Z \end{pmatrix} = \mathcal{R}(n_1 t) \begin{pmatrix} x \\ y \\ z \end{pmatrix},$$

and correspondingly we have

$$\begin{pmatrix} \dot{X} \\ \dot{Y} \\ \dot{Z} \end{pmatrix} = \mathcal{R}(n_1 t) \begin{pmatrix} \dot{x} - n_1 y \\ \dot{y} + n_1 x \\ \dot{z} \end{pmatrix}, \quad \begin{pmatrix} \ddot{X} \\ \ddot{Y} \\ \ddot{Z} \end{pmatrix} = \mathcal{R}(n_1 t) \begin{pmatrix} \ddot{x} - 2n_1\dot{y} - n_1^2 x \\ \ddot{y} + 2n_1\dot{x} - n_1^1 y \\ \ddot{z} \end{pmatrix},$$

Substituting them into Eq. (2.30) and after simplification we obtain the equations of motion in synodic coordinate frame

$$\begin{aligned} \ddot{x} - 2n_1\dot{y} - n_1^2 x &= -(1-\mu)\frac{x+\mu}{r_1^3} - \mu\frac{x-1+\mu}{r_2^3}, \\ \ddot{y} + 2n_1\dot{x} - n_1^2 y &= -\frac{1-\mu}{r_1^3}y - \frac{\mu}{r_2^3}y, \\ \ddot{z} &= -\frac{1-\mu}{r_1^3}z - \frac{\mu}{r_2^3}z. \end{aligned} \tag{2.31}$$

Indeed, by introducing a scalar function U, called *effective potential*

$$U(x,y,z) = -\frac{n_1^2}{2}(x^2+y^2) - \frac{1-\mu}{r_1} - \frac{\mu}{r_2},$$

the equations of motion are simply represented as:

$$\begin{aligned} \ddot{x} - 2n_1\dot{y} &= -\frac{\partial U}{\partial x}, \\ \ddot{y} + 2n_1\dot{x} &= -\frac{\partial U}{\partial y}, \\ \ddot{z} &= -\frac{\partial U}{\partial z}. \end{aligned}$$

Indeed the effective potential is equal to the Newtonian potential plus one additional term $-\frac{n_1^2}{2}(x^2+y^2)$, which is the centrifugal potential.

The circular restricted three-body problem has a first integral called *Jacobi integral*

$$\begin{aligned} C_J &= -2U - (\dot{x}^2 + \dot{y}^2 + \dot{z}^2) \\ &= n_1^2(x^2+y^2) + 2\left(\frac{1-\mu}{r_1} + \frac{\mu}{r_2}\right) - (\dot{x}^2 + \dot{y}^2 + \dot{z}^2), \end{aligned} \tag{2.32}$$

which is the only first integral of the problem. The Jacobi integral plays a crucial role for numerical exploration of the problem.

2.4.2 The Levi-Civita Regularization for the PCRTBP

In this thesis we care about the situation where close encounters or collisions of P with P_1 are possible. It is useful, and for numerical consideration it is mandatory, to define the equations of motion for P by regularizing the equations (2.31) with respect to the secondary mass P_1. For the planar problem, we consider the Levi-Civita transformation defined by:

$$\begin{pmatrix} x-(1-\mu) \\ y \end{pmatrix} = \begin{pmatrix} u_1 & -u_2 \\ u_2 & u_1 \end{pmatrix} \begin{pmatrix} u_1 \\ u_2 \end{pmatrix},$$

along with the time transformation:

$$dt = r_1 ds,$$

where s is called the fictitious time. The equations of motion in the new variables u_1, u_2 with respect to the fictitious time s are

$$\begin{cases} u_1'' &= \frac{1}{4}\left[(a+b)u_1 + cu_2\right], \\ u_2'' &= \frac{1}{4}\left[(a-b)u_2 + cu_1\right], \end{cases} \tag{2.33}$$

with a, b, c given in [Fro70]

$$\begin{cases} a &= \frac{2(1-\mu)}{r_0} - C_J + x^2 + y^2, \\ b &= 4y' + 2r_1 x - \frac{2(1-\mu)r_1(x+\mu)}{r_0^3}, \\ c &= 2r_1 y - 4x' - \frac{2(1-\mu)r_1 y}{r_0^3}. \end{cases}$$

To get the variational equations we first write the Eq. (2.33) as a system of first order differential equations:

$$\begin{cases} u_1' = v_1, \\ u_2' = v_2, \\ v_1' = \frac{1}{4}\left[(a+b)u_1 + cu_2\right], \\ v_2' = \frac{1}{4}\left[(a-b)u_2 + cu_1\right], \end{cases} \tag{2.34}$$

and, with $\mathbf{w} = (u_1, u_2, v_1, v_2)$, we write it in compact form

$$\mathbf{w}' = F(\mathbf{w}),$$

whose variational equations are

$$\begin{cases} \mathbf{w}' &= F(\mathbf{w}), \\ \boldsymbol{\xi}' &= \frac{\partial F}{\partial \mathbf{w}}(\mathbf{w})\boldsymbol{\xi}, \end{cases} \tag{2.35}$$

where $\boldsymbol{\xi} \in \mathbb{R}^4$ represents a tangent vector. The variational equations will be used for the computation of the Fast Lyapunov Indicators.

2.4.3 The Kustaanheimo-Stiefel Regularization for the SCRTBP

The generalization of the Levi-Civita regularization to the spatial CRTBP is represented by the Kustaanheimo-Stiefel regularization [Kust64, Kust65]:

$$\begin{pmatrix} x-(1-\mu) \\ y \\ z \\ 0 \end{pmatrix} = \begin{pmatrix} u_1 & -u_2 & -u_3 & u_4 \\ u_2 & u_1 & -u_4 & -u_3 \\ u_3 & u_4 & u_1 & u_2 \\ u_4 & -u_3 & u_2 & -u_1 \end{pmatrix} \begin{pmatrix} u_1 \\ u_2 \\ u_3 \\ u_4 \end{pmatrix},$$

which is a map from 4-dimensional space to the 3-dimensional space (for more details, see [Kust64, Kust65, RosG24, CardG22]). The fictitious time is also introduced

$$dt = r_1 ds,$$

where in the new variables the distance between P and P_1 is

$$r_1 = \sqrt{(x-1+\mu)^2 + y^2 + z^2} = u_1^2 + u_2^2 + u_3^2 + u_4^2.$$

The inverse relations distinguish between the cases $x-(1-\mu) < 0$ and $x-(1-\mu) \geq 0$ (see [Fro70]):

$$\begin{array}{ll} \text{for } x-(1-\mu) < 0, & \text{for } x-(1-\mu) \geq 0 \\ u_3 = 0, & u_4 = 0 \\ u_2 = \sqrt{\dfrac{r_1 - (x-(1-\mu))}{2}}, & u_1 = \sqrt{\dfrac{r_1 + (x-(1-\mu))}{2}} \\ u_1 = \dfrac{y}{2u_2}, & u_2 = \dfrac{y}{2u_1} \\ u_4 = \dfrac{z}{2u_2}, & u_3 = \dfrac{z}{2u_1}. \end{array}$$

With these new variables, after some computations we have:

$$\begin{pmatrix} 4u_1'' \\ 4u_2'' \\ 4u_3'' \\ 4u_4'' \end{pmatrix} = A_1 \begin{pmatrix} u_1 \\ u_2 \\ u_3 \\ u_4 \end{pmatrix} + A_2 \begin{pmatrix} u_1 \\ -u_2 \\ -u_3 \\ u_4 \end{pmatrix} + A_3 \begin{pmatrix} u_2 \\ u_1 \\ -u_4 \\ -u_3 \end{pmatrix} + A_4 \begin{pmatrix} u_3 \\ u_4 \\ u_1 \\ u_2 \end{pmatrix}, \tag{2.36}$$

where

$$\begin{cases} A_1 &= \frac{2(1-\mu)}{r_0} - C_J + x^2 + y^2, \\ A_2 &= 4y' + 2xr_1 - \frac{2(1-\mu)r_1(x+\mu)}{r_0^3}, \\ A_3 &= -4x' + 2yr_1 - \frac{2(1-\mu)yr_1}{r_0^3}, \\ A_4 &= -\frac{2(1-\mu)zr_1}{r_0^3}. \end{cases}$$

Similar with the planar case, Eq. (2.36) can also be written as a system of first order differential equations, from which the variational equations can be derived.

2.5 Fast Lyapunov chaos indicators

In the phase-space of quasi-integrable Hamiltonian systems, several types of motions can coexist, such as the perpetually stable motions on KAM tori, complex motions which are homoclinic or heteroclinic to hyperbolic resonant tori, or even motions undergoing very slow diffusions (for instance Chirikov diffusion, adiabatic diffusion and Arnold diffusion). In the literature there are at least numerical examples of all these kinds of motions in the restricted three-body problem which, however, presents an additional ingredient for instability because of the gravitational close encounters with the secondary body.

In the last decades a set of numerical tools have demonstrated to be very efficient in the detection of the different types of motions described above, such as the Frequency Analysis [LasFC92, Las93] and the finite time chaos indicators, like the Fast Lyapunov Indicator (FLI) [FroGL00, GuzL02], the Mean Exponential Growth of Nearby Orbits (MEGNO) [CinS00] and the Finite Time Lyapunov Exponents (FTLE) [TangB96]. In this thesis we use the Finite Time Lyapunov Indicator to analyze the output of numerical integrations, and in particular different versions of the FLI have been developed in the literature to specifically study the close encounters of the three body problem [FroGL97a, FroGL00, LegGF11, GuzL13, GuzL14, GuzL15, LegG16, LegGF16, GuzL23]. In this Section we recall the definition of FLI, as well as some of its properties, that will be used in the thesis. We refer to the previous references for more detailed explanations.

2.5.1 The finite time chaos indicator

Consider a system of first-order differential equations defined on an open subset $D \subset \mathbb{R}^n$

$$\dot{\mathbf{w}} = F(\mathbf{w}), \tag{2.37}$$

where $F : D \to \mathbb{R}^n$ is a smooth vector field on D. From the theory of Lyapunov exponents, the chaotic properties of a solution are measured by the temporal separation of solutions with initial data close to it. More precisely, consider a reference solution $\mathbf{w}(t)$ with initial condition $\mathbf{w}(0) = \mathbf{w}_0$ and the modified solution $\mathbf{w}(t) + \varepsilon\boldsymbol{\xi}(t)$ with the initial condition $\mathbf{w}(0) + \varepsilon\boldsymbol{\xi}(0) = \mathbf{w}_0 + \varepsilon\boldsymbol{\xi}_0$. Since we have

$$\dot{\mathbf{w}} + \varepsilon\dot{\boldsymbol{\xi}} = F(\mathbf{w} + \varepsilon\boldsymbol{\xi}),$$

by expanding the right-hand side around $\mathbf{w}$, substituting Eq. (2.37), and ignoring higher order terms in ε we obtain the variational equation for $\boldsymbol{\xi}$:

$$\dot{\boldsymbol{\xi}} = \frac{\partial F}{\partial \mathbf{w}}(\mathbf{w}(t))\boldsymbol{\xi}. \tag{2.38}$$

Since the variational equation is linear in ξ, we regard the vector $\boldsymbol{\xi} \in \mathbb{R}^n$ as a tangent vector. For $\boldsymbol{\xi}_0 \in \mathbb{R}^n \backslash \{0\}$, the ratio $\|\boldsymbol{\xi}(t)\|/\|\boldsymbol{\xi}_0\|$ estimates the amplification of the separation of two orbits at time t whenever ε is small and as long as $\varepsilon\|\boldsymbol{\xi}(t)\|$ remains small as well. The law of local asymptotic separation of nearby solutions is well represented by the Characteristic Lyapunov Exponents, defined for an initial condition $\mathbf{x}_0$ and initial tangent vector $\boldsymbol{\xi}_0$ by:

$$l(\mathbf{x}_0, \boldsymbol{\xi}_0) := \lim_{t\to\infty} \frac{1}{t} \ln\left(\frac{\|\boldsymbol{\xi}(t)\|}{\|\boldsymbol{\xi}(0)\|}\right), \tag{2.39}$$

where $\boldsymbol{\xi}(t)$ is obtained by solving Eq. (2.37) and Eq. (2.38) simultaneously. Besides, the largest Lyapunov exponent of $\mathbf{w}_0$ is defined as the maximum of $l(\mathbf{w}_0, \boldsymbol{\xi})$ for $\boldsymbol{\xi} \neq 0$. The numerical computation of the Lyapunov exponents can be done following the method introduced in [BeneGGS80a, BeneGGS80b].

In [FroGL00] it has been shown that the regular motions in a quasi-integrable system (on KAM tori or inside the resonances) can be discriminated from the chaotic ones by computing the so called finite time chaos indicators in short time intervals of order $1/\sqrt{\varepsilon}$. The Fast Lyapunov Indicator (FLI) of $\mathbf{w}_0$ and $\boldsymbol{\xi}_0$ at time T, first introduced in [FroGL97a, FroLG97b], is defined by

$$FLI(\mathbf{w}_0, \boldsymbol{\xi}_0; T) = \max_{0\leq t\leq T} \log_{10}\left(\frac{\|\boldsymbol{\xi}(t)\|}{\|\boldsymbol{\xi}(0)\|}\right). \tag{2.40}$$

The value of the FLI grows approximately linearly in the time T for chaotic orbits, while for regular orbits it grows as a logarithm. Besides, the growth of the FLI follows such behaviors for regular and chaotic orbits independently of the choice of the initial tangent vector, unless for some specific directions. To avoid the issues related to the choice of specific initial tangent vectors, the following FLI has been defined (see [GuzL18]):

$$FLI(\mathbf{w}_0; T) = \max_{0\leq t\leq T} \max_{\boldsymbol{\xi}_0 : \|\boldsymbol{\xi}_0\|=1} FLI(\mathbf{w}_0, \boldsymbol{\xi}(0); T).$$

To save computational time, also the indicator:

$$FLI(\mathbf{w}_0; T) = \max_{0\leq t\leq T} \max_{1\leq j\leq n} FLI(\mathbf{w}_0, \boldsymbol{\xi}_j; T),$$

proved to be effective, where $\boldsymbol{\xi}_1, \cdots, \boldsymbol{\xi}_n$ is a orthonormal basis for the tangent space.

Particularly, the FLI distinguishes between regular motions of different nature: it is a sensitive tool of indicating the resonant and non-resonant regular orbits [FroGL00]. Therefore, the distribution of the resonances of a system can be detected with high detail by computing the FLI of grids of points of the phase-space. Particularly informative are the computations of the FLI on 2-dimensional grids, and represented using a color scale.

In the following we illustrate the properties of the FLI using as a model example the standard map:

$$\Phi(\phi, I) = (\phi + I \mod 2\pi, \quad I + \varepsilon \sin(\phi + I)),$$

where $(\phi, I) \in \mathbb{T} \times \mathbb{R}$ are the phase-space variables and $\varepsilon \geq 0$ characterizes the integrability of the system (see [LegGF16, GuzL23]). The fixed points of the standard map are $(\phi, I) = (0, 0)$ and $(\phi, I) = (\pi, 0)$. The fixed point $(\phi, I) = (\pi, 0)$ is stable for all small positive values of ε, and the fixed point $(\phi, I) = (0, 0)$ is hyperbolic, and therefore its stable and unstable manifolds are related to a set of chaotic orbits for the map.

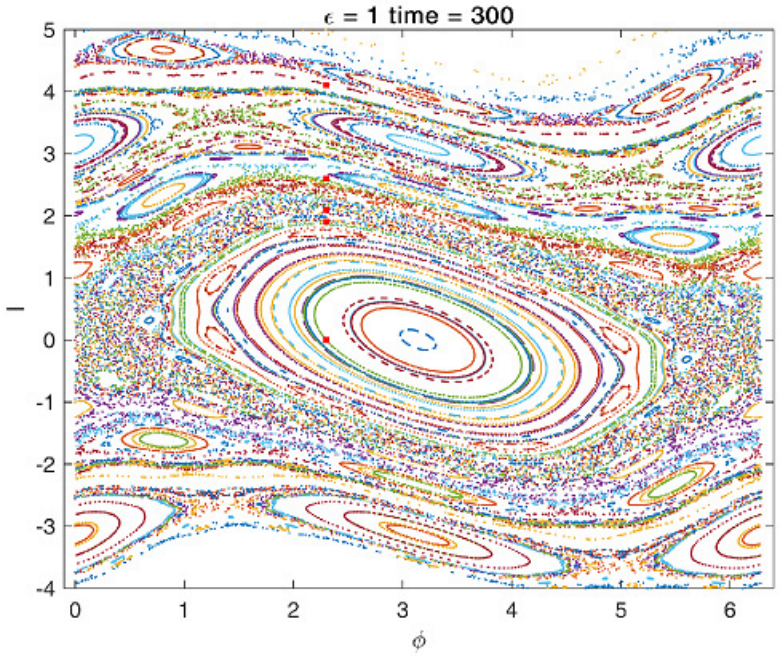

Figure 2.4: Phase portrait of the Standard map for $\varepsilon = 1$ obtained by computing numerically the orbits for a number of iterations $N = 300$. The five red squares at $(\phi, I) = (2.3, 0), (2.3, 1.9), (2.3, 2.1), (2.3, 2.6), (2.3, 4.1)$ identify initial conditions that will be studied in more detail. The initial values for the tangent vectors are: $\boldsymbol{\xi}^{(1)}(0) = \left(1/\sqrt{2}, 1/\sqrt{2}\right)$ and $\boldsymbol{\xi}^{(2)}(0) = \left(1/\sqrt{2}, -1/\sqrt{2}\right)$.

Fig. 2.4 represents the phase-portrait of the standard map computed up to $N = 300$ iterations for $\varepsilon = 1.0$. Five red squares in Fig. 2.4 identify initial conditions of orbits that we study in more detail.

Since the standard map defines a discrete dynamical system, its chaos indicators are defined by the iterations of the tangent map:

$$D\Phi(v_\phi, v_I) = (v_\phi + v_I, v_I + \varepsilon(v_\phi + v_I)\cos(\phi + I)),$$

where (v_ϕ, v_I) denotes the tangent vectors. Therefore, for an initial condition (ϕ_0, I_0) and for an initial tangent vector $\boldsymbol{\xi}_0 = (v_{\phi_0}, v_{I_0})$, the sequence $\boldsymbol{\xi}_t = (v_{\phi_t}, v_{I_t})$ is obtained by

$$\boldsymbol{\xi}_{t+1} = D\Phi\Big|_{\phi_t, I_t} \boldsymbol{\xi}_t$$

with

$$(\phi_{t+1}, I_{t+1}) = \Phi(\phi_t, I_t).$$

The FLI is then computed from the sequence $\boldsymbol{\xi}_t$. For example, for a basis $\boldsymbol{\xi}^{(1)}, \boldsymbol{\xi}^{(2)}$ of initial tangent vectors, we have:

$$FLI(\phi, I; T) = \max_{0 \le t \le T} \max_{j=1,2} \log_{10} \|\boldsymbol{\xi}^{(j)}(t)\|. \tag{2.41}$$

For comparison, we also represent the indicator

$$cle(\phi, I, t) = \frac{FLI(\phi, I, t)}{t},$$

which tends to the characteristic Lyapunov exponents for t going to infinity.

Fig. 2.5 illustrates the time evolution of the FLI and cle for orbits chosen in different regions of the phase-space, characterized by different dynamics. First of all, we remark that there is a sharp separation of time evolution of FLI between the strongly chaotic orbit (the black one) and the others. From the FLI evolution up to $T = 300$ we realize that another orbit (the purple one) is weakly chaotic, as it is evident when the iteration number becomes large than $T = 500$. Such sharp separation between the strong chaotic orbits and other orbits is difficult to be detected by the CLE in a short number of iterations. For regular orbits (the blue, brown and green one), the FLI grows slowly than for the chaotic orbits, and furthermore, the growth occurs at different rates depending on the type of regular orbit [FroGL00], for example, depending on whether it is a KAM torus or regular orbits belonging to resonances. Instead, with evidence the CLEs converge to zero as the number of iterations increases.

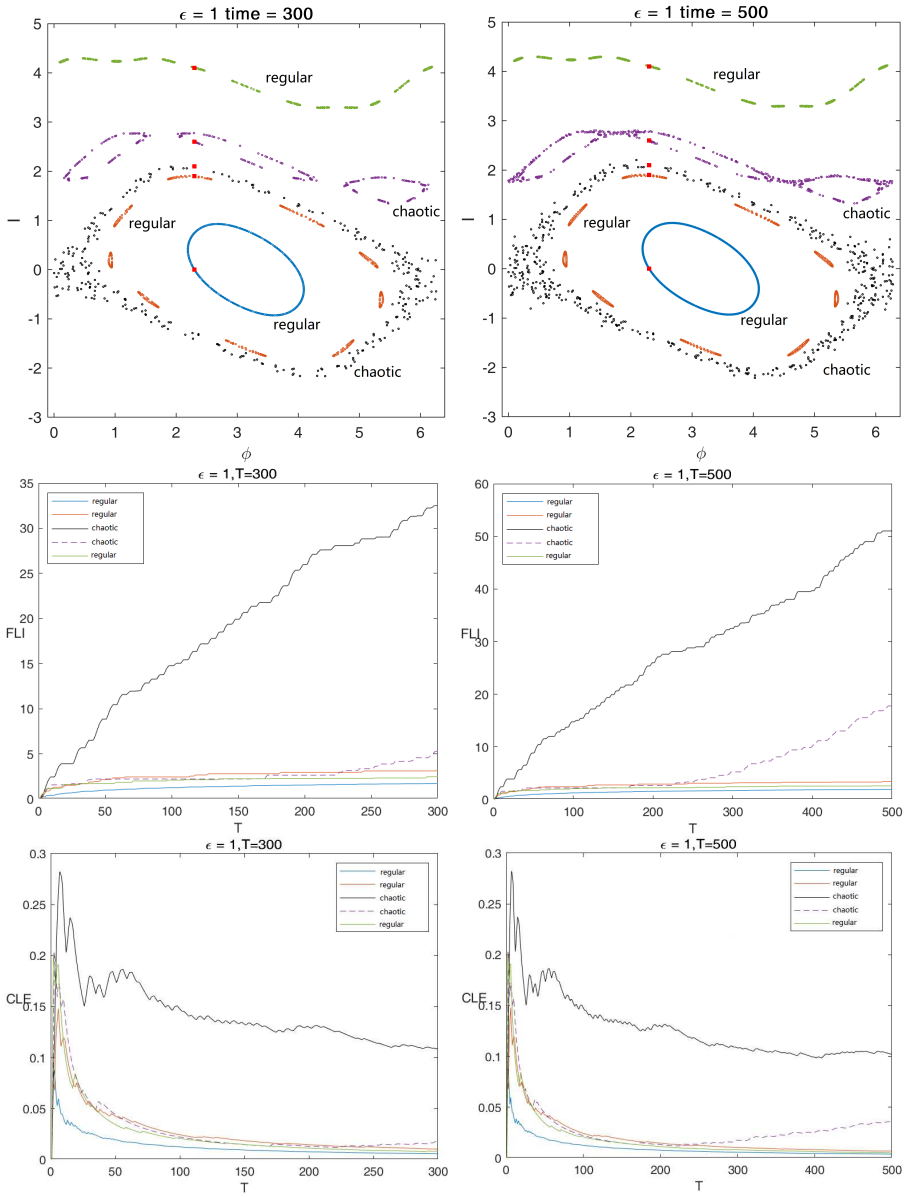

Figure 2.5: Selected orbits of the standard map and time evolution of the correspondent chaos indicators. Top panels: the selected orbits in the phase space. Center panels: evolution of the FLI for the orbits in the top panels. Bottom panels: representation of the cle for the same orbits in top panels.

In Fig. 2.6 the values of FLI are calculated on a grid of 629×751 initial data in the phase space for different iteration numbers. The orbits from Fig. 2.5 are also represented (the light blue points). The darker regions, characterized by the smaller values of the FLI, are full of regular motions while the yellow regions,

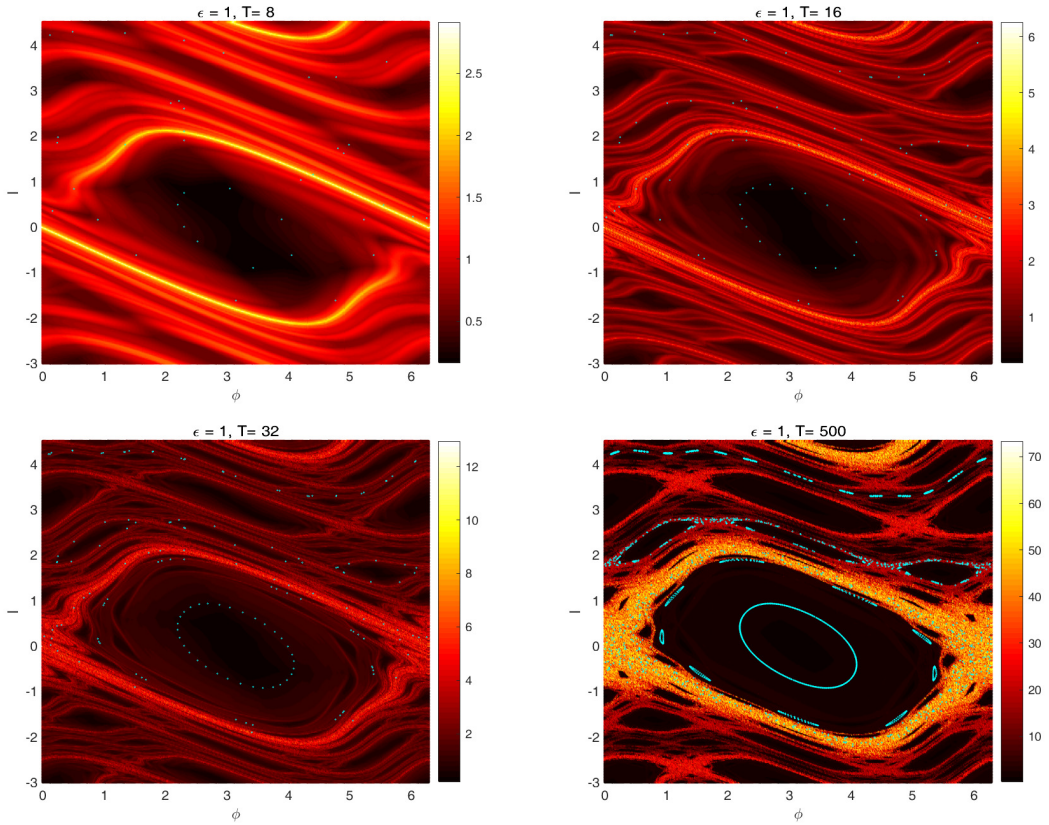

Figure 2.6: Representation of values of FLI on a grid of 629×751 initial conditions, with five selected orbits represented with light blue points.

characterized by the higher values of the FLI, identify the chaotic motions. Indeed, the identification of the strongly chaotic region and regular one is quite evident already in the top-left panel corresponding to only $T = 8$ iterations. From the bottom-right panel (corresponding to $T = 500$), we notice the strong chaotic orbit is scattered inside the chaotic region associated to the unstable fixed point $(\phi, I) = (0, 0)$. Besides, Fig. 2.6 also illustrates the finite pieces of the stable manifold of the unstable fixed point (for instance see the curves departing from $(\phi, I) = (0, 0)$ which in the top-left panel are shorter, due to the shorter time T, and are longer in the other panels). The ability of the FLI to identify the stable manifolds of hyperbolic invariant sets has been established in [GuzL14]. In fact, the FLI measures how fast two close orbits split from each other. For an orbit located very near at the stable manifold of a saddle fixed point, its time iterations will converge to the invariant set, with exponential growth of the norm of tangent vectors as long as the orbit will remain close to the hyperbolic set. Therefore, the value of the FLI will be larger the closer the orbit is to the stable manifold.

Therefore, points very close to the stable manifold of the fixed point $(\phi, I) = (0, 0)$, or of the other hyperbolic fixed points, will have higher value of FLI, hence brighter color in the figures.

2.5.2 FLI for the PCRTBP in MMR

In this Subsection we anticipate some examples of computations of the FLI for orbits in the MMR of the PCRTBP. Let us therefore consider the 1:2 MMR, the action-angle variables $S, N, \Theta, \sigma, \nu, \theta$ introduced in Eq. (2.22), and the Hamiltonian of the PCRTBP represented with these variables:

$$\widehat{\mathcal{H}} = \widehat{\mathcal{H}}_0(S, N, \Theta) + \varepsilon \widehat{\mathcal{H}}_1(S, N, \sigma, \nu, \theta).$$

Then we represent the values of regularized FLI in the plane of the resonant variables defined by:

$$x = \sqrt{2S}\cos(\sigma), \quad y = \sqrt{2S}\sin(\sigma). \tag{2.42}$$

As remarked before, the action variable N is a first integral of the averaged Hamiltonian. Different values of N will give us different kinds of dynamics. The examples shown in this Section are obtained by computing the FLI of initial conditions with $N = -1.24$, for which neither crossing orbits nor collisions are possible [Bea94]. In Fig. 2.7, left panel, we represent with a color scale the FLI computed for 500×500 initial conditions with $N = -1.24, \nu = \pi, \theta = 0$, and S, σ obtained from Eq. (2.42) and $T = 800$ units of the fictitious time of the LC regularization.

Since in this thesis we mainly consider the orbits of large eccentricity, following [LegGF11, GuzL13, LegG16, GuzL18], the FLI is computed using the non-averaged equations of motion of the CRTBP regularized at the secondary body P_1 with the Levi-Civita regularization (for the planar problem) and of the Kustaanheimo-Stiefel regularization (for the spatial problem), see Section 2.4.2 and 2.4.3.

Specifically the fast Lyapunov indicators computed in this thesis are defined from the variational dynamics of the equations of motion of the non-averaged CRTBP regularized at P_1 with the Levi-Civita or Kustaanheimo-Stiefel regularization. Let us denote with: u the LC or the KS variables; s the fictitious time related to the physical time by $dt = \|P - P_1\|ds$; $v = \frac{du}{ds}$; $\mathbf{w} = (u, v)$ the variables of the LC or KS state-space; $\boldsymbol{\xi} = (\boldsymbol{\xi}_u, \boldsymbol{\xi}_v)$ the tangent vector to the space of the variables $\mathbf{w} = (u, v)$. For any initial datum $\boldsymbol{\xi}_0$ of the equations of motion of the CRTBP regularized at P_1:

$$\frac{d\mathbf{w}}{ds} = F(\mathbf{w}), \tag{2.43}$$

and any initial tangent vector $\boldsymbol{\xi}_0$, we consider the solution $\mathbf{w}(s)$ of Eq. (2.43) with initial conditions $\mathbf{w}_0$, and the solution $\boldsymbol{\xi}(s)$ of the variational equations of (2.43):

$$\frac{d\boldsymbol{\xi}}{ds} = \frac{\partial F}{\partial \mathbf{w}}(\mathbf{w}(s))\boldsymbol{\xi},$$

with initial conditions $\boldsymbol{\xi}_0$. The regularized Fast Lyapunov Indicator of the initial condition $\mathbf{w}_0$, initial tangent vector $\boldsymbol{\xi}_0$ and fictitious time T is defined as:

$$FLI(\mathbf{w}_0, \boldsymbol{\xi}_0; T) = \max_{0 \le s \le T} \log_{10} \frac{\|\boldsymbol{\xi}(s)\|}{\|\boldsymbol{\xi}(0)\|}.$$

Instead, the selection of the initial conditions, the representation of the phase-portraits of the resonance, as well as the distribution of the regular and chaotic motions, is better obtained using the resonant action-angle variables introduced in Eq. 2.42 (see also Chapter 3).

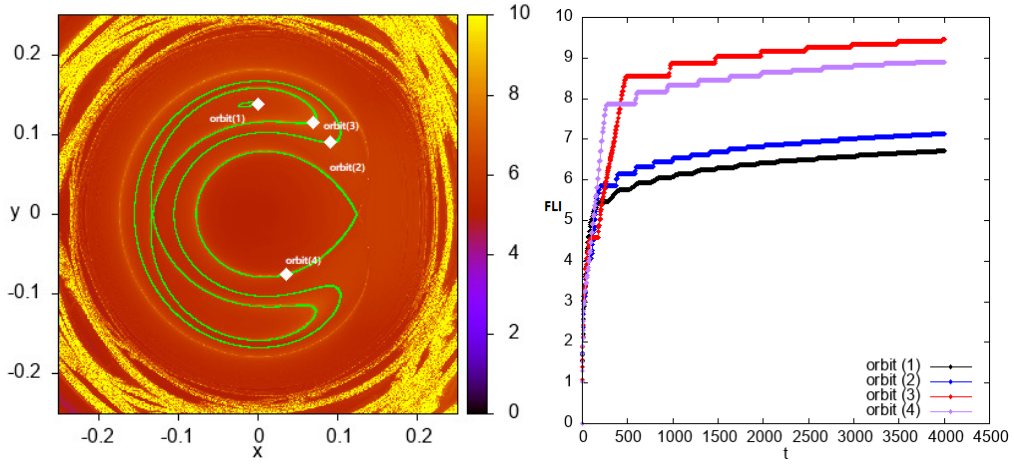

Figure 2.7: Left panel: Resonant phase structure of PCRTBP for $N = -1.24$ on $x - y$ plane with selected 4 orbits whose initial conditions are indicated with white squares. Right panel: FLI evolution of 4 selected orbits from left panels.

In Fig. 2.7, the green curves in the left panel are the projections of four orbits whose initial conditions are identified by the white squares. Orbit (1) is inside one of the asymmetric libration regions, orbit (2) is located inside the symmetric libration region, orbit (3) is quite close to the separatrix around $x < 0, y = 0$ (or $\sigma = \pi$), and orbit (4) is close to the separatrix around $x > 0, y = 0$ (or $\sigma = 0$). The time evolution of regularized FLI of the 4 orbits are plotted in the right panel. We appreciate that the evolution of FLI offers a good separation between the regular and chaotic orbits. In fact, after a short transient time, the FLI values for the librations (orbit (1) and (2)) remain smaller than the FLI values of the

orbits close to the separatrices of the resonance (orbit(3) and (4)). The regular or chaotic behavior of the orbits is detected by the FLI already at $T = 500$.

Chapter 3

The limits of canonical perturbation theory inside MMRs for crossing orbits and close encounters: the planar case

In this chapter, we study the limits of application of canonical perturbation theory, specifically the validity of the normal form approximations, for the study of the mean motion resonances of the planar circular restricted three-body problem in the domain of orbits which cross, or are close to cross, the orbit of the secondary body. First, we discuss analytic issues related to the definition of a MMR normal form within a domain of the phase-space to which these orbits belong; then, we compute with a numerical method the canonical transformations defining the MMR normal forms. The limits of validity of the averaging method are studied by supplementing the information provided by the phase-portrait representations of the normal form Hamiltonian with analyses concerning the preservation of the quasi-integrals of motion obtained through one step of perturbation theory, and the computation of fast Lyapunov indicators regularized with respect to the close encounters with the secondary body. We provide numerical explorations using as model examples the external 1:2 and 5:6 MMRs for values of the mass ratios which are representative of the Sun–Jupiter and Sun–Neptune cases. The choice of these model resonances has been done according to the different values of the resonant semi-major axis: the 5:6 resonance represents the limit case of a resonance very close to the semi-major axis of the planet, while the 1:2 resonance is more distant from this value. Both resonances are of first order to optimize the description of the analytic part; resonance of larger order may be considered with a proper re-definition of the resonant variables. Only external resonances are considered for two reasons. The first reason is that external resonant encounters had been identified by several authors to be relevant for the diffusion of Kuiper belt objects to the inner part

of the Solar system. The second reason is that we can use the same analytic framework, and simplify the discussion of the results. Internal resonances may be considered as well, with suitable modifications of the variables and the expansions. For the 1:2 MMR, the efficacy of the averaging method is established also for chaotic orbits of eccentricity up to $e \simeq 0.55$ (which is already quite a large value for the eccentricity; our methods can be applied also to larger values). The researches reported in this Chapter are original, and have been published in [LiuGuzzo25].

The Chapter is organized as follows: in Section 3.1 we first recall the definition of resonant variables and then we define and discuss the properties of the singular sets, as well as the sets of close encounters, represented with the resonant variables. We also show that the Fourier expansion of the perturbation with respect to the angle $\nu+\theta$ is well defined outside the singular set, and its finite truncations provide a good approximation outside a set of close encounters. In Section 3.2, we provide the formal definition of the averaging transformation to the MMR normal form and describe the algorithm which allows to numerically compute it also for crossing orbits. In Section 3.3, we provide explorations of the method to study motions with close encounters of P with P_1 for the 1:2 and 5:6 MMRs for values of the masses which are representative of the CR3BP defined by the Sun-Jupiter and Sun-Neptune masses. Section 3.4 is dedicated to the Conclusions.

3.1 Fourier expansions, singular sets and sets of close encounters

Let us consider a $p : q$ external MMR of order 1 (i.e. $q - p = 1$). We first recall the definition of the resonant action-angle variables which are adapted to the specific resonance, that we already introduced in Chapter 2 (see Eq. 2.22), for the planar CR3BP. Consider the canonical transformation from the modified Delaunay variables:

$$\begin{aligned} \Lambda &= \sqrt{a}, & \lambda &= M + \omega \\ \Phi &= \sqrt{a}(1 - \sqrt{1 - e^2}), & \varphi &= -\omega \\ \Lambda_1 \ , & & \theta &= \lambda_1, \end{aligned}$$

where the action Λ_1 conjugate to λ_1 is introduced to make autonomous the problem, to the action-angle variables $S, N, \Theta, \sigma, \nu, \theta$ defined by:

$$\begin{pmatrix} \sigma \\ \nu \\ \theta \end{pmatrix} = \begin{pmatrix} q & q-p & -p \\ \delta & \zeta & \zeta-\delta-1 \\ 0 & 0 & 1 \end{pmatrix} \begin{pmatrix} \lambda \\ \varphi \\ \lambda_1 \end{pmatrix}, \tag{3.1a}$$

$$\begin{pmatrix} S \\ N \\ \Theta \end{pmatrix} = \begin{pmatrix} \zeta & -\delta & 0 \\ p-q & q & 0 \\ p-q+1 & q-1 & 1 \end{pmatrix} \begin{pmatrix} \Lambda \\ \Phi \\ \Lambda_1 \end{pmatrix}, \tag{3.1b}$$

where $\delta, \zeta \in \mathbb{Z}$ satisfy

$$q\zeta + (p-q)\delta = 1.$$

Remark. (i) The angle σ defined in Eq. (3.1a) is the critical angle of the resonance: for a $p:q$ MMR it is the angle $q\lambda - p\lambda_1$ plus the angle $(q-p)\varphi$ which is necessary for $\sigma = q\lambda - p\lambda_1 + (q-p)\varphi$ to be invariant with respect to rotations of the axis of the nodes, and has the given expression in such a way to respect the D'Alembert rules. (ii) The angle ν is a fast angle: in fact, $q\nu$ is the sum of the fast angle $-p\lambda_1$ and the slow angles $q\zeta\varphi$ and $\delta(q\lambda - p\lambda_1)$. Moreover, the Hamiltonian of the planar problem depends on the fast angles ν, θ only through their sum $\nu+\theta$, which is a fast angle as well: in fact $q(\nu+\theta)$ is the sum of the fast angle λ_1 and the slow angles $q\zeta\varphi$ and $\delta(q\lambda - p\lambda_1)$. (iii) The examples considered in this chapter concern the 1:2 and 5:6 MMRs for which we use $\delta = -1$ and $\zeta = 0$.

With the action-angle variables defined by Eq. (3.1), the integrable part of the Hamiltonian of the PCR3BP is expressed by

$$\widehat{\mathcal{H}}_0(S, N, \Theta) := -\frac{1}{2(qS + \delta N)^2} + n_1(-pS + (\zeta - \delta - 1)N + \Theta),$$

and the perturbing function, which depends also on the angles σ and $\nu + \theta$, is represented as the Fourier series:

$$\begin{aligned} \widehat{\mathcal{H}}_1(S, N, \sigma, \nu+\theta) =& c_0(S, N, \sigma) + \sum_{k=1}^{\infty} c_k(S, N, \sigma)\cos(k(\nu+\theta)) \\ &+ \sum_{k=1}^{\infty} s_k(S, N, \sigma)\sin(k(\nu+\theta)), \end{aligned} \tag{3.2}$$

where

$$c_0(S,N,\sigma) := \widehat{\mathcal{H}}_1^{Res}(S,N,\sigma) = \frac{1}{2\pi}\int_0^{2\pi} \widehat{\mathcal{H}}_1(S,N,\sigma,\nu+\theta)d(\nu+\theta), \tag{3.3}$$

$$c_k(S,N,\sigma) = \frac{1}{\pi}\int_0^{2\pi} \widehat{\mathcal{H}}_1(S,N,\sigma,\nu+\theta)\cos[k(\nu+\theta)]d(\nu+\theta),\ k\geq 1 \tag{3.4}$$

$$s_k(S,N,\sigma) = \frac{1}{\pi}\int_0^{2\pi} \widehat{\mathcal{H}}_1(S,N,\sigma,\nu+\theta)\sin[k(\nu+\theta)]d(\nu+\theta),\ k\geq 1. \tag{3.5}$$

We remark that, for small values of the eccentricity e, the averaging transformations have been effectively constructed in the literature using Fourier expansions of the perturbing function H_1 defined by the modified Delaunay variables:

$$H_1 = \sum_{(k,m)\in\mathbb{Z}^2} c_{k,m}(\Lambda,\Phi)e^{i[k\lambda+(k+m)\varphi+m\lambda_1]}, \tag{3.6}$$

where the coefficients $c_{k,m}$ are conveniently expanded as Taylor series. A classical expansion of these coefficients reproduces the expansion in the eccentricity e, which of course is not effective when the eccentricity is large.

There are several reasons why the definition and convergence of the Fourier expansion (3.6) might fail in this case. At large eccentricities singularities of H_1 and its Fourier expansions appear: on the one hand, for large values of the eccentricity e the function H_1 is singular for values of the modified Delaunay variables such that:

$$\mathbf{r}(\Lambda,\Phi,\lambda,\varphi) = (\cos(\lambda_1),\sin(\lambda_1)), \tag{3.7}$$

which corresponds to a collision of P with P_1; on the other hand the coefficients of the Fourier expansion (3.6) and their partial derivatives may be singular also when

$$a(1-e) \leq r_1 \leq a(1+e) \tag{3.8}$$

i.e. for values of the modified Delaunay variables corresponding to an orbit of P which crosses or is tangent to the orbit of P_1. In fact, these coefficients are defined from the double-integrals:

$$\int_0^{2\pi}\int_0^{2\pi} H_1(\Lambda,\Phi,\lambda+\varphi,\lambda_1+\varphi)e^{-i[k\lambda+(k+m)\varphi+m\lambda_1]}d(\lambda+\varphi)d(\lambda_1+\varphi),$$

and if Λ,Φ correspond to a,e satisfying (3.8) there are values of λ,φ and λ_1 for which Eq. (3.7) is satisfied, and correspondingly the integrand is singular. This property of the Fourier expansions is responsible of the paradox that the expansion

(3.6) (or its partial derivatives) may be singular for values of $(\Lambda, \Phi, \lambda, \phi, \lambda_1)$ which do not correspond to a collision, but correspond to an intersection or tangency of the orbits of P and P_1. For the analytic characterization of these singularities we refer to the papers [GroM98, GroT12, FenGS22].

Several methods have been introduced in the literature to treat the problem of large eccentricities. For example, expansions of H_1 around libration points of the MMR normal form of large eccentricity are defined in the papers [FerS89, Fer87, RoigSFT97]; closed-form expansions are proposed and applied to the non-resonant problem in [RosE23, CavE22, MasE23]; numerical computations of the averaged Hamiltonian have been successfully used to study orbits in MMR having close-encounters with a planet, Jupiter or Neptune [Bea94, Tho98, Mor02, NesTFM02].

The key point for the development of the averaging method inside a MMR is that the double Fourier series (3.6) is not really needed to define averaging transformations and to compute the averaged Hamiltonian. The action-angle variables $S, N, \Theta, \sigma, \nu, \theta$ and the corresponding Fourier expansions (3.2) (and similar ones) have been specifically introduced in the literature for this purpose.

In fact, expansion (3.2), whose coefficients are obtained by integrating the perturbing function over only one angle, is more regular than the double Fourier series (3.6).

The coefficient c_0 in Eq. (3.3), which provides the averaged Hamiltonian, can been numerically computed, following for example Schubart's method (see [Schu64, Schu66, Moons94]). In particular, in the papers [Bea94, Tho98] the function c_0 had been numerically computed also for large values of the eccentricity outside a curve of the resonant phase-plane (S, σ), the 'singular set' defined in Subsection 2.1, where collisions of P with P_1 may occur. Since we are interested in computing also the averaging transformation (and not only the averaged Hamiltonian), we complete the analysis by computing also the coefficients c_k, s_k given by Eq.s (3.4) and (3.5). We first show that the coefficients $c_k(N, S, \sigma), s_k(N, S, \sigma)$ can be efficiently computed using a Fast Fourier Transform algorithm outside a neighborhood of the singular set. Then, we show that a suitable finite truncation of the Fourier expansion (3.2) approximates accurately the perturbing function $\widehat{H}_1$ outside a small neighbourhood of the singular set, which we call the 'set of close encounters'.

3.1.1 The singular set and the set of close encounters

We first characterize, for given values of N, the domains of the resonant phase-plane (S, σ) where close encounters or collisions of P with P_1 may occur. We find that, outside the singular set (already identified in the papers [Bea94, Tho98] as

a set where collisions may occur, and which will be defined precisely below), the Fourier expansion (3.2) of $\widehat{\mathcal{H}}_1$ is well defined and, outside a set of close encounters, the FFT representation of $\widehat{\mathcal{H}}_1$ is indeed an efficient representation that can be used to define the averaging transformations. We anticipate that such a set contains also points (N, S, σ) representing orbits of P which cross the orbit of P_1, for which the double Fourier series of $\widehat{\mathcal{H}}_1$ or its derivatives with respect to both angles σ and $\nu + \theta$ are singular.

To define the singular sets and sets of close encounters we consider the system of equations:

$$r = r_1 + d \tag{3.9a}$$

$$\omega + f = \lambda_1 + \alpha \tag{3.9b}$$

depending on the parameters d, α, where d represents the difference between the norms of the radius vectors of P and P_1, while α represents the difference between the true longitudes of P and P_1. We recall that here we use the notations for the CR3BP introduced in Chapter 2. In particular, $\mathbf{r}$ is the radius vector of P; $r = |\mathbf{r}|$; $\mathbf{r}_1$ is the radius vector of P_1 defined by $\mathbf{r}_1 = r_1 \left(\cos(n_1 t), \sin(n_1 t)\right)$ and we choose the units of measure such that $G = 1, m_0 = 1, r_1 = 1$.

Let us solve the system (3.9) for different values of d, α in the space of the MMR variables $N, S, \nu, \sigma, \theta$, and discuss the properties of the set of the solutions; the case $d, \alpha = 0$ identifies the collisions of P with P_1, while small values of $|d|, |\alpha|$ identify close encounters.

We restrict our analysis to the states of P represented by orbital elements a, e, f, ω with $0 < e < 1$. In such a case, Eq. (3.9a) has solutions only if a, e satisfy the inequalities:

$$a(1 - e) \leq r_1 + d \leq a(1 + e), \tag{3.10}$$

i.e. if $r_1 + d$ is smaller than or equal to the aphelion and larger than or equal to the perihelion. In such a case, Eq. (3.9a) has 1 or 2 solutions expressed in the form: $f = f_*^i(a, e, d)$ with $i = 1, 2$, where f_*^i are suitable functions of a, e, d. Equivalently, the solutions are expressed using the mean anomaly, rather than the true anomaly, in the form:

$$M = M_*^i(a, e, d). \tag{3.11}$$

Note that the case of 2 solutions occurs for crossing orbits while the case of 1 solution occurs for tangent orbits.

System (3.9) is therefore equivalent to the systems:

$$M = M_*^i(a, e, d) \tag{3.12a}$$

$$\omega + f_*^i(a, e, d) = \lambda_1 + \alpha, \tag{3.12b}$$

obtained for $i = 1, 2$. Let us represent the solutions of (3.12) using the variables $(S, N, \sigma, \nu, \theta)$. From equation (3.1), we obtain:

$$\begin{pmatrix} \lambda \\ \varphi \\ \lambda_1 \end{pmatrix} = \begin{pmatrix} 0 & p-q & 1+p-q \\ -1 & q & q-1 \\ 0 & 0 & 1 \end{pmatrix} \begin{pmatrix} \sigma \\ \nu \\ \theta \end{pmatrix} \tag{3.13}$$

and therefore, since $M = \lambda + \varphi = \sigma + p(\nu + \theta)$, equation (3.12a) becomes:

$$\sigma + p(\nu + \theta) = M_*^i(S, N, d). \tag{3.14}$$

Equation (3.12b) may be rewritten as:

$$\lambda_1 - \omega = f_*^i(a, e, d) - \alpha \tag{3.15}$$

and since $\lambda_1 - \omega = \theta + \varphi = \sigma + q(\nu + \theta)$, this equation becomes:

$$\sigma + q(\nu + \theta) = f_*^i(S, N, d) - \alpha. \tag{3.16}$$

Finally, the system (3.12) becomes

$$\begin{pmatrix} 1 & p \\ 1 & q \end{pmatrix} \begin{pmatrix} \sigma \\ \nu + \theta \end{pmatrix} = \begin{pmatrix} M_*^i(S, N, d) \\ f_*^i(S, N, d) - \alpha \end{pmatrix} \tag{3.17}$$

whose coefficient matrix has determinant equal to 1. Therefore, for each value of S, N, d, α, it is solved by the $(\sigma, \nu + \theta)$ satisfying:

$$\begin{pmatrix} \sigma \\ \nu + \theta \end{pmatrix} = \begin{pmatrix} q & -p \\ -1 & 1 \end{pmatrix} \begin{pmatrix} M_*^i(S, N, d) \\ f_*^i(S, N, d) - \alpha \end{pmatrix}. \tag{3.18}$$

The solutions of the system (3.9) are therefore represented in the variables $S, N, \sigma, \nu, \theta$ by the set

$$\begin{aligned} \mathcal{C}_{d,\alpha} = \{(S, N, \sigma, \nu, \theta) : \sigma = q M_*^i(S, N, d) - p f_*^i(S, N, d) + p\alpha, \\ \nu + \theta = -M_*^i(S, N, d) + f_*^i(S, N, d) - \alpha, i = 1, 2\}. \end{aligned} \tag{3.19}$$

It is also useful to define the projection of the set $\mathcal{C}_{d,\alpha}$ to the space of the variables (N, S, σ):

$$\mathcal{S}_{d,\alpha} = \left\{(S, N, \sigma) : \sigma = q M_*^i(S, N, d) - p(f_*^i(S, N, d) - \alpha), i = 1, 2\right\}. \tag{3.20}$$

In fact the set $\mathcal{S}_{0,0}$, which we call the 'singular set', contains the values N, S, σ for which there is at least a value of $\nu + \theta$ providing a collision of P with P_1. As a consequence, for $(S, N, \sigma) \in \mathcal{S}_{0,0}$ there are values of $\nu + \theta$ for which the integrands in the Eq.s (3.4), (3.5) defining the Fourier coefficients $c_k(S, N, \sigma), s_k(S, N, \sigma)$ are

singular. Instead, if $(S, N, \sigma) \notin \mathcal{S}_{0,0}$ the integrands are regular for all $\nu + \theta \in [0, 2\pi]$ and the Fourier development (3.2) can be used to define the averaging transformations.

For small values of $|d|, |\alpha|$ the set $\mathcal{S}_{d,\alpha}$ will be called a 'set of close encounters' and contains the values N, S, σ for which there is at least a value of $\nu+\theta$ providing a close encounter of P with P_1 characterized by the parameters d, α. While for $(S, N, \sigma) \in \mathcal{S}_{d,\alpha}$, with $(d, \alpha) \neq (0, 0)$ the function $\widehat{\mathcal{H}}_1(S, N, \sigma, \nu+\theta)$ is periodic and regular for all $\phi = \nu + \theta \in [0, 2\pi]$, so that the Fourier expansion of $\widehat{\mathcal{H}}_1$ is well defined, the number of terms of this expansion which are necessary in order to obtain a good approximation by means of the truncated series:

$$\langle \widehat{\mathcal{H}}_1 \rangle := c_0(S, N, \sigma) + \sum_{k=1}^{K} c_k(S, N, \sigma) \cos(k(\nu + \theta)) + \sum_{k=1}^{K} s_k(S, N, \sigma) \sin(k(\nu + \theta))$$

with some $K \in \mathbb{N}$, increases as $|d|, |\alpha|$ become small. Therefore, for any given cut-off K, we may use this finite Fourier approximations to implement the canonical perturbation theory only outside a neighborhood of the singular set made of sets of close encounters. Before addressing this problem we provide some representations of the sets $\mathcal{S}_{d,\alpha}$.

For fixed values of N the sets $\mathcal{S}_{d,\alpha}$ can be represented in the plane of the variables S, σ, or alternatively in the plane of the related variables $x = \sqrt{2S}\cos\sigma$, $y = \sqrt{2S}\sin\sigma$. First of all we highlight some symmetries hidden in the definition of the sets. As a matter of fact, the sets $\mathcal{C}_{d,\alpha}, \mathcal{S}_{d,\alpha}$ depend parametrically also on the value of the radius r_1 of the circular orbit (which is fixed to 1 by the choices of the units of measure). Considering $d \neq 0$ is equivalent to consider $r_1 \neq 1$ and $d = 0$, i.e. close encounters with a circular orbit of radius $r_1 + d$ rather than with a circular orbit of radius r_1. Therefore, by introducing the sets $\mathcal{C}^{r_1}_{d,\alpha}, \mathcal{S}^{r_1}_{d,\alpha}$ where r_1 is a parameter not necessarily fixed to 1, we have:

$$\mathcal{C}^{r_1}_{d,\alpha} = \mathcal{C}^{r_1+d}_{0,\alpha} \quad , \quad \mathcal{S}^{r_1}_{d,\alpha} = \mathcal{S}^{r_1+d}_{0,\alpha}.$$

Next, if $(a, e, f, \omega, \theta)$ solve the system (3.9) with parameters d, α, then $(a, e, f, \omega - \alpha, \theta)$ solve the system (3.9) with parameters $d, 0$. Therefore, if $(N, S, \sigma) \in \mathcal{S}^{r_1}_{d,\alpha}$ then $(N, S, \sigma - p\alpha) \in \mathcal{S}^{r_1}_{d,0}$ and we have:

$$\mathcal{S}^{1}_{d,\alpha} = \mathcal{S}^{1+d}_{0,\alpha} = \mathcal{R}(-p\alpha)\mathcal{S}^{1+d}_{0,0} \tag{3.21}$$

where $\mathcal{R}(-p\alpha)$ operates on the set $\mathcal{S}^{1+d}_{0,0}$ a translation of the variable σ by an angle $-p\alpha$ (and in the plane of the variables x, y makes a rotation of an angle $-p\alpha$), and the geometry of all the sets of close encounters $\mathcal{S}_{d,\alpha}$ are obtained by modifying the geometry of the sets $\mathcal{S}^{r_1}_{0,0}$ according to equation (3.21).

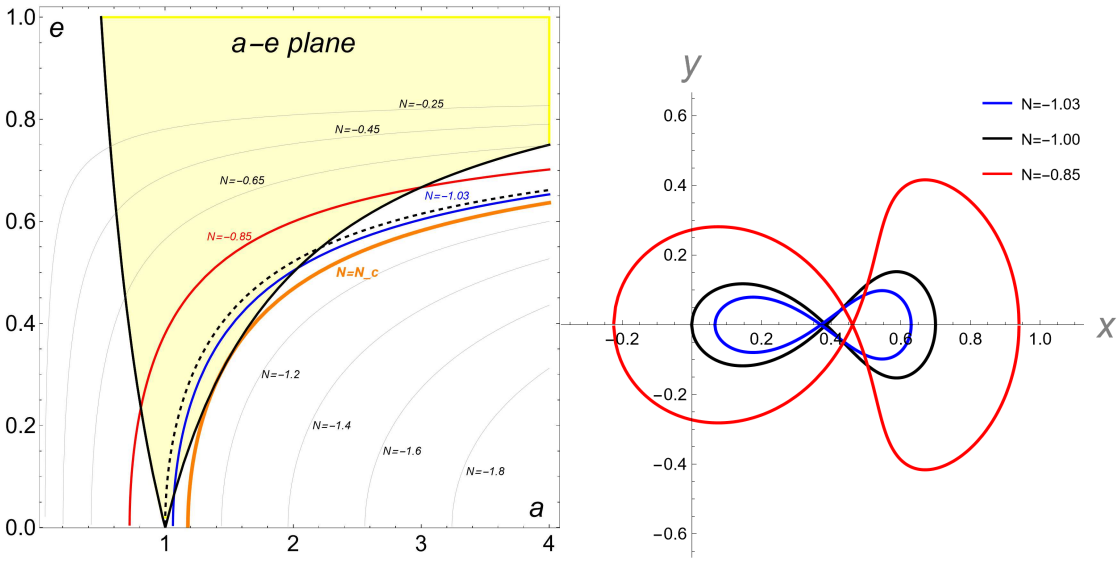

Figure 3.1: Left panel: representation in the $a-e$ plane of different level sets of the action $N = \sqrt{a}((p-q)+q(1-\sqrt{1-e^2}))$ defined for the 1:2 resonance: the dashed line corresponds to $N = 1$; the bold orange line corresponds to $N = N_c \sim -1.0852$; the red and blue lines correspond to $N = -0.85, -1.03$ (the corresponding singular sets are represented in the right panel); the other level sets are represented in gray; the curves of pericenters $a(1-e) = 1$ and of apocenters $a(1+e) = 1$ are represented in black. The region $a(1-e) \leq 1 \leq a(1+e)$, which contains the values of semi-major axis and eccentricity of the orbits which intersect or are tangent to the orbit of P_1, is represented by the yellow area. From the picture we appreciate that there is a critical value of N, denoted as $N_c \sim -1.0852$, such that the orbits with $N < N_c$ do not intersect and are not tangent to the orbit of P_1. Right panel: Representation of the singular sets $\mathcal{S}_{0,0}$ for the 1:2 resonance and $N = -0.85, -1, -1.03$ in the plane of the variables x, y defined in Eq. (3.22).

Let us therefore describe the properties of the singular sets $\mathcal{S}_{0,0}$; for definiteness we consider the case of the 1:2 resonance, and represent the sets in the plane of the resonant variables:

$$x = \sqrt{2S}\cos\sigma, \quad y = \sqrt{2S}\sin\sigma. \tag{3.22}$$

In the left panel of Fig. 3.1 we represent the level sets λ_N of the action $N = \sqrt{a}((p-q)+q(1-\sqrt{1-e^2}))$ in the $a-e$ plane, together with the curves of equation $a(1-e) = 1$, $a(1+e) = 1$. The singular set, with evidence, is non empty only for values of N such that the corresponding set λ_N intersects the area above the curves $a(1-e) = 1$, $a(1+e) = 1$. In such a case, we identify three interesting cases:

- when $N > -1$ the curve λ_N (red curve in the left panel) intersects both the curves of apocenters $a(1+e) = 1$ and of pericenters $a(1-e) = 1$ (black curves). Since apocenters are identified by $M = f = \pi$, from Eq. (3.18) the singular set contains a point with $\sigma = (q-p)\pi = \pi$; similarly, the intersection with the curve of pericenters provides instead a point in the singular set with $\sigma = 0$. Therefore, the singular set extends on both half-planes $x > 0$ and $x < 0$ (see Fig. 3.1, right panel).

- when $N < -1$ (and larger than the critical value N_c for which λ_c is tangent to the curve of pericenters) the curve λ_N (blue curve) intersects only the curve of pericenters. In this case the singular set belongs only to the half-plane $x > 0$ (see Fig. 3.1, right panel).

- for $N = -1$ the singular set belongs only to the half-plane $x \geq 0$ and contains the origin of the plane xy (see Fig. 3.1, right panel).

In Fig. 3.2 we also represent two families of sets $\mathcal{S}_{d,\alpha}$ which are obtained by changing the parameters d or α up to the border of the Hill's sphere of planet Jupiter[1].

3.1.2 Singular sets and Fourier expansions

According to the discussion of Subsection 3.1.1, the integrands appearing in the equations (3.3) (3.4) and (3.5) are regular for all the values of (S, N, σ) which do not belong to a singular set. Correspondingly, the coefficients c_k, s_k are regular also when computed for the points of the crossing orbits which do not belong to these sets. In this Subsection we check the efficiency of the truncated Fourier representations:

$$\langle \widehat{\mathcal{H}}_1 \rangle := c_0(S,N,\sigma) + \sum_{k=1}^{K} c_k(S,N,\sigma)\cos(k(\nu+\theta)) + \sum_{k=1}^{K} s_k(S,N,\sigma)\sin(k(\nu+\theta)) \tag{3.23}$$

for (S, N, σ) in sets that do not include the singular set $\mathcal{S}_{0,0}$ and a suitable set of close encounters, but includes orbits of P which cross the orbit of P_1. We first need a method to compute the coefficients c_k, s_k for any specific value of $(S, N, \sigma) \notin \mathcal{S}_{0,0}$ without using the double Fourier expansions of $\mathcal{H}_1$ with respect to both angles σ and $\nu + \theta$.

[1]For simplicity, differently from the usual definition, in this chapter we define the radius of the Hill's sphere equal to $\sqrt[3]{\frac{m_1}{m_0+m_1}}$.

Figure 3.2: Representation of the set of close encounters $\mathcal{S}^1_{d,\alpha}$ in the plane of the variables x, y defined in Eq. (3.22) for the 1:2 resonance, $m_1 = 10^{-3}$, and $N = -1.00$. The left panel represents three sets $\mathcal{S}^1_{d,0}$: the singular set for $d = 0$ (purple), the set of close encounters for $d = \sqrt[3]{\mu}$ (blue), where $\mu = m_1/(m_0 + m_1)$, and for $d = -\sqrt[3]{\mu}$ (black). The right panel represents three sets $\mathcal{S}^1_{0,\alpha}$: the singular set for $\alpha = 0$ (purple), the set of close encounters for $\alpha = \arcsin \sqrt[3]{\mu}$ (blue) and for $\alpha = -\arcsin \sqrt[3]{\mu}$ (black).

We remark that the reconstruction of Hamiltonian models from Fourier expansions of the perturbing functions have been often used in recent works, see for example [Mog22, MasL23]. In this paper, we compute the coefficients of the Fourier expansions (3.23) by adapting to the present case the numerical method first developed by Schubart (see [Schu64, Schu66, Moons94]). First, we need to figure out how to compute the value of $\widehat{\mathcal{H}}_1$ for any given value of S, N, σ and $\nu + \theta$. Indeed, the perturbation $\mathcal{H}_1$ is easily expressed with the orbital elements (a, e, λ, ω) and the longitude λ_1 of P_1

$$\mathcal{H}_1(a, e, \omega, f, \lambda_1) = -\left(\frac{1}{\sqrt{r^2 + 1 - 2r\cos(\psi)}} - r\cos(\psi) \right)$$

where $r = a(1 - e\cos(E))$, E is eccentric anomaly of P, and $\psi := (f + \omega) - \lambda_1$ is the difference between the longitudes of P and P_1. According to the definition of modified Delaunay variables and equations (2.22), the values of S, N determine

the values of semi-major axis a and eccentricity e:

$$\begin{aligned} a &= (qS - N)^2 \\ e &= \sqrt{1 - \left(1 - \frac{(q-p)S}{qS - N}\right)^2}. \end{aligned} \tag{3.24}$$

Meanwhile, the values of $\sigma, \nu + \theta$ determine the value of the mean anomaly:

$$M = \lambda + \varphi = \sigma + p(\nu + \theta). \tag{3.25}$$

By computing numerically the solution E of Kepler's equation $M = E - e \sin E$ one computes the value of eccentric anomaly. Finally, the value of $\cos \psi$ is computed as follows. First we have:

$$\cos \psi = \cos(-\sigma - q(\nu + \theta)) \cos f - \sin(-\sigma - q(\nu + \theta)) \sin f, \tag{3.26}$$

and next we compute $\tan f$ using the standard formulae (see, for example, [MurDer00]).

$$\tan \frac{f}{2} = \sqrt{\frac{1+e}{1-e}} \tan \frac{E}{2}. \tag{3.27}$$

As a consequence the value of $\widehat{\mathcal{H}}_1(S, N, \sigma, \nu + \theta)$ is computed for any given value of $(S, N, \sigma, \nu + \theta)$.

For any given value of S, N, σ, the values of the coefficients $c_k(S, N, \sigma)$ and $s_k(S, N, \sigma)$ are then computed using the Fast Fourier Transform algorithm. Precisely, by considering a suitably refined grid of values for the angle $\phi = \nu + \theta$:

$$\phi_j = \frac{j}{K} 2\pi, \quad j = 0, \cdots, K - 1$$

with $K = 2^n$, the FFT of the sequence $\widehat{\mathcal{H}}_1(S, N, \sigma, \phi_j), j = 0, \cdots, K - 1$ provides a numerical approximation for the integrals:

$$\int_0^{2\pi} \widehat{\mathcal{H}}_1(S, N, \sigma, \phi) e^{ij\phi} d\phi$$

for $j = -\frac{K}{2}, \cdots, \frac{K}{2}$. From standard trigonometric formulas, we then compute an approximation for the coefficients c_k, s_k. To implement first order canonical perturbation theory we also compute with FFT the Fourier expansion of the derivatives of $\widehat{\mathcal{H}}_1(S, N, \sigma, \nu + \theta)$ with respect to S, N, σ and $\nu + \theta$.

In Figs. 3.3, 3.4, 3.5 we provide an example of the efficiency of this computation, where we consider the 1:2 and 5:6 mean motion resonances and a value of

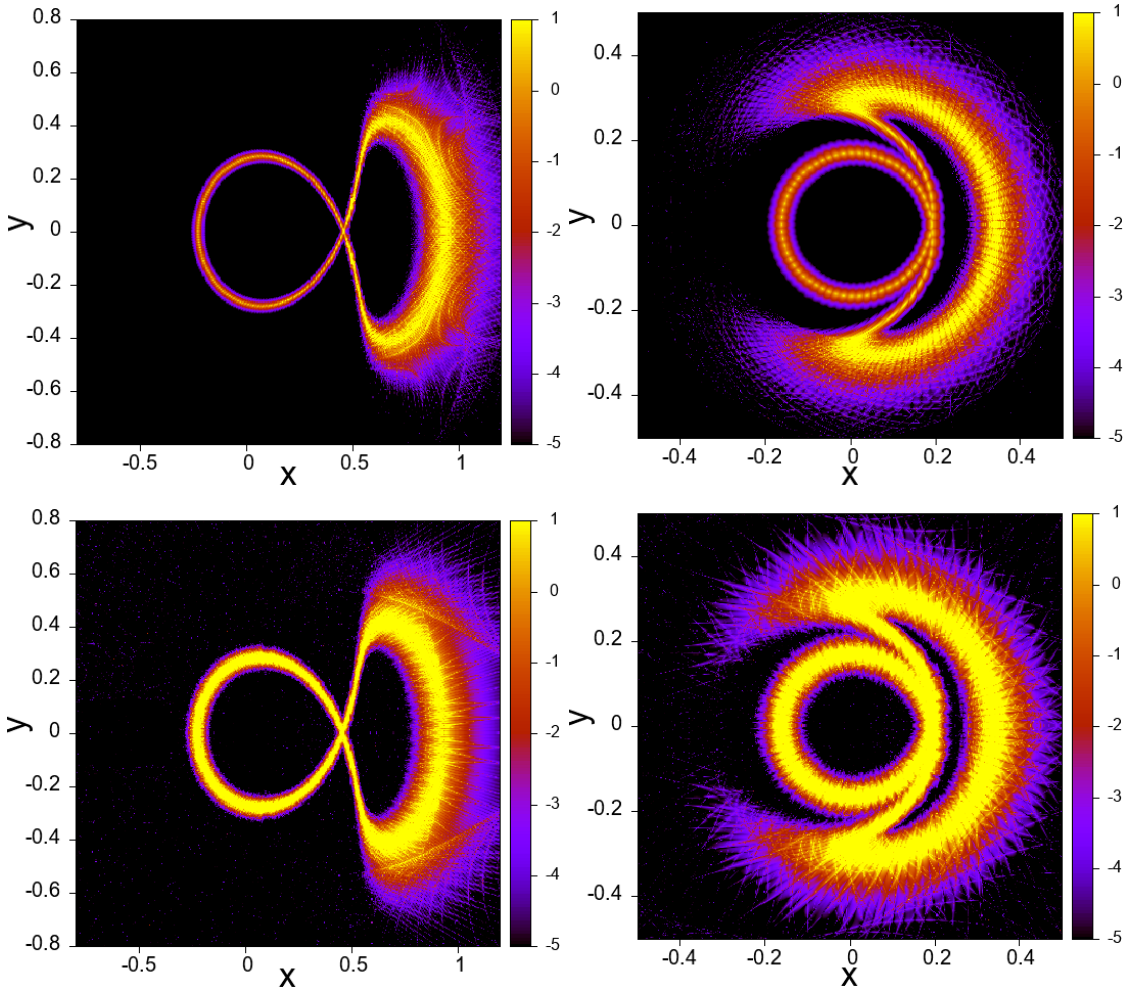

Figure 3.3: Efficiency of the Fourier representation of Eq. (3.23). In the panels we represent with a color scale the value of $\log_{10}|\mathcal{E}|$, where $\mathcal{E}$ is defined in Eq. (3.29), computed on a refined grid of 500×500 points of the plane of the variables x, y defined in Eq. (3.22). The rows represent the indicator computed for $\widehat{\mathcal{H}}_1$, $\frac{\partial \widehat{\mathcal{H}}_1}{\partial S}$, respectively, for $N = -0.85$, and for the 1:2 MMR (left panels) and 5:6 MMR (right panels). The Fourier series is computed by applying the FFT using a sampling of $K = 512$ points; the indicator $\mathcal{E}$ is computed by sampling the variables $\phi \in [0, 2\pi]$ with $J = 300$ points. The indicators computed for the derivative $\frac{\partial \widehat{\mathcal{H}}_1}{\partial N}$ is represented in Fig. 3.4, and the derivatives $\frac{\partial \widehat{\mathcal{H}}_1}{\partial \sigma}$, $\frac{\partial \widehat{\mathcal{H}}_1}{\partial \phi}$ are represented in Fig. 3.5.

$N = -0.85$, for which there is a large singular set in the x-y plane. We compare the values of the function $\widehat{\mathcal{H}}_1$ and its partial derivatives with the values of the truncated Fourier series of $\widehat{\mathcal{H}}_1$ (and its partial derivatives) defined in Eq. (3.23) and

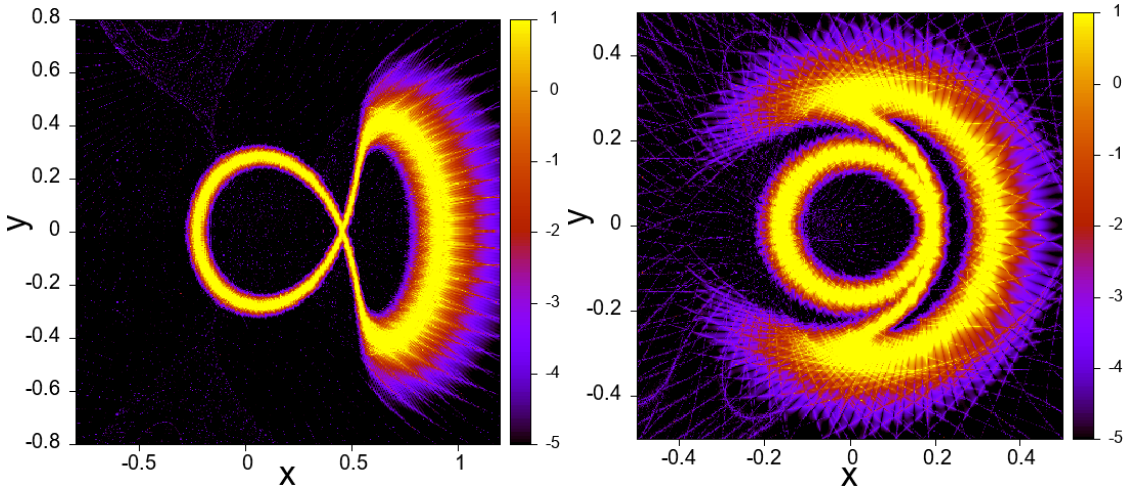

Figure 3.4: Efficiency of the Fourier representation of Eq. (3.23), see Fig. 3.3, for the derivatives $\frac{\partial \widehat{\mathcal{H}}_1}{\partial N}$.

computed with the numerical method described above, on a three-dimensional grid of points $(N, S, \nu, \sigma, \theta)$ with $N = -0.85$; the values of S, σ are defined by sampling the variables $x = \sqrt{2S}\cos\sigma$, $y = \sqrt{2S}\sin\sigma$ in a regularly spaced grid of 500×500 values in the intervals $x, y \in [0, 0.8]$ (corresponding to orbits of eccentricity ranging from $e = 0$ to $e = 0.6...$); $\phi = \nu + \theta$ is sampled in $[0, 2\pi]$ with a regular grid of J values.

For each value of x, y in the grid, we compute an indicator of the efficiency of the Fourier representation of the functions:

$$\widehat{\mathcal{H}}_1, \frac{\partial \widehat{\mathcal{H}}_1}{\partial S}, \frac{\partial \widehat{\mathcal{H}}_1}{\partial N}, \frac{\partial \widehat{\mathcal{H}}_1}{\partial \sigma}, \frac{\partial \widehat{\mathcal{H}}_1}{\partial \phi}, \tag{3.28}$$

defined by relative error:

$$\mathcal{E} := \max_j \frac{|\mathcal{U}(S, N, \sigma, \phi_j) - < \mathcal{U} > (S, N, \sigma, \phi_j)|}{|\mathcal{U}(S, N, \sigma, \phi_j)|}, \tag{3.29}$$

where $\mathcal{U}$ represents any of the functions (3.28), and $\langle \mathcal{U} \rangle$ its finite Fourier approximation defined by K.

On the panels of the figures, for each value of x, y we represent the value of the indicator $\mathcal{E}$ with a color scale. We notice that only close to the singular set the Fourier representation of $\widehat{\mathcal{H}}_1$ and its derivatives has relative error larger than 10^{-5}, thus validating their use of perturbation theory outside a neighborhood of the singular set.

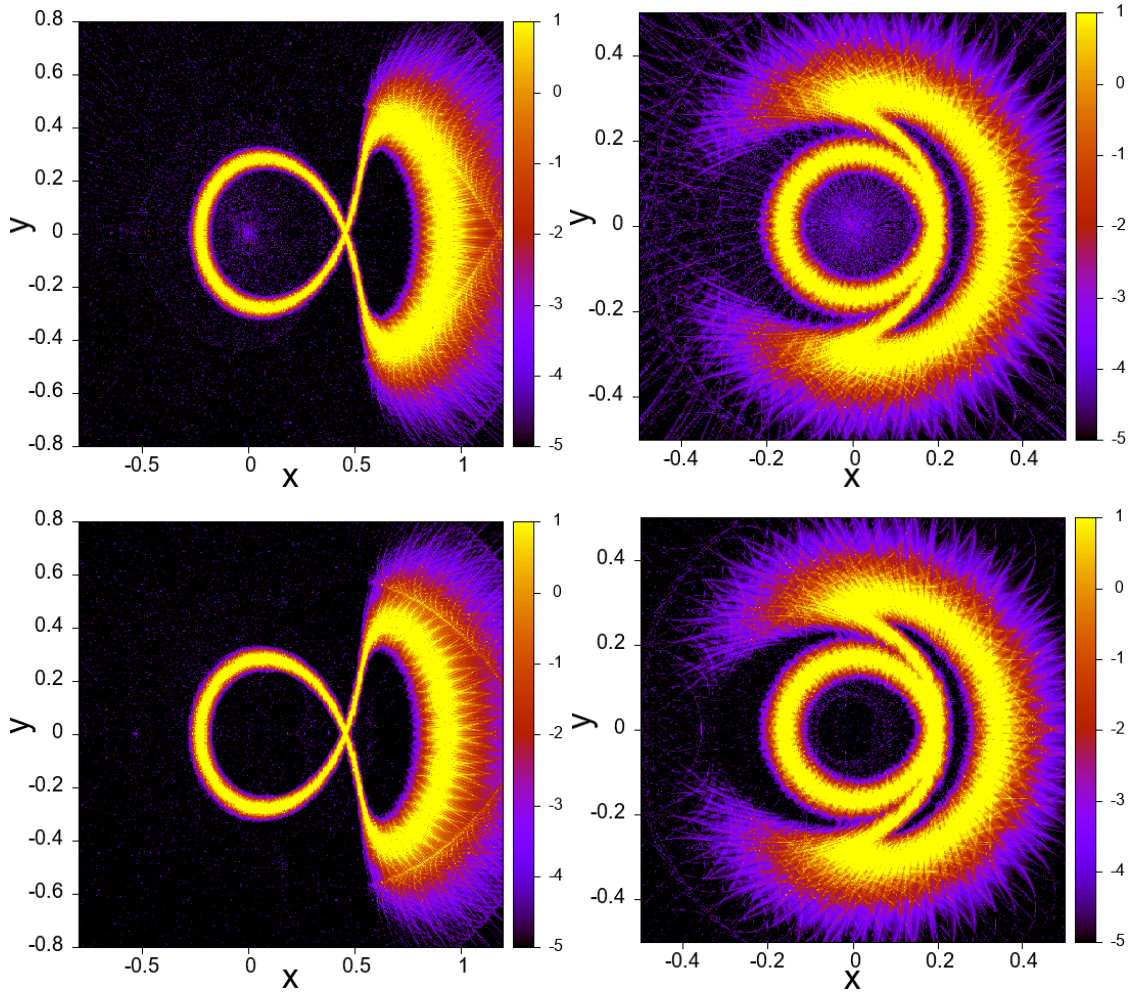

Figure 3.5: Efficiency of the Fourier representation of Eq. (3.23), as in Fig. 3.3 and 3.4: each row represents the value of $\log_{10}|\mathcal{E}|$ computed for $\frac{\partial\widehat{\mathcal{H}}_1}{\partial\sigma}$ and $\frac{\partial\widehat{\mathcal{H}}_1}{\partial\phi}$.

A very different situation is observed by computing the errors of the double Fourier representation, see Fig. 3.6: we clearly appreciate that for most points of sampling the errors of the representation are very big [2].

[2]The tiny stripes in the pictures describe the periodicities in the error functions.

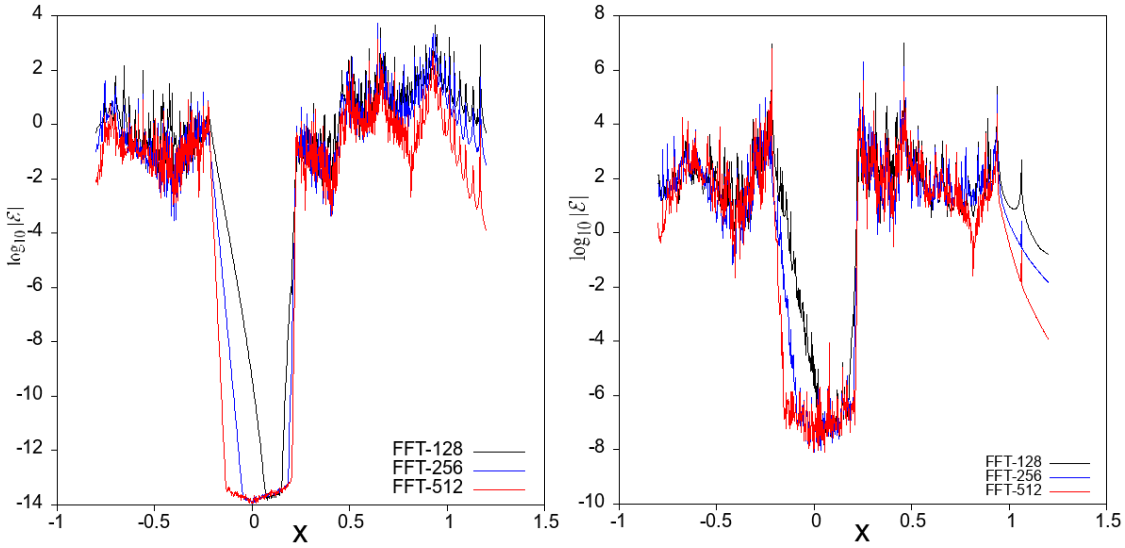

Figure 3.6: Errors of the double Fourier representation of the function $\widehat{\mathcal{H}}_1$. In the panels we represent the value of $\log_{10}|\mathcal{E}|$ with $\mathcal{U}$ equal to $\widehat{\mathcal{H}}_1$ (left panel) and $\frac{\partial \widehat{\mathcal{H}}_1}{\partial S}$ (right panel), computed on a refined grid of 500 points of the variable x and a fixed value of $y = 0.01$. We consider the 1:2 MMR, $N = -0.85$. The three curves correspond to $K = 128$ (black), $K = 256$ (blue), and $K = 512$ (red). The indicator is computed by sampling the variable $\phi \in [0, 2\pi]$ with $J = 300$ points.

3.2 Definition of the averaging transformation

Let us consider the perturbation $\widehat{\mathcal{H}}_1$ expanded as indicated in Section 3.1, Eq. (3.2):

$$\widehat{\mathcal{H}}_1 = c_0(S, N, \sigma) + \sum_{k=1}^{\infty} c_k(S, N, \sigma)\cos(k(\nu+\theta)) + \sum_{k=1}^{\infty} s_k(S, N, \sigma)\sin(k(\nu+\theta))$$

for $(S, N, \sigma) \notin \mathcal{S}_{0,0}$ and all values of $\nu + \theta$. Notice that the expansion (3.2) is well defined even if S, N correspond to an orbit of P crossing the orbit of P_1, but the value of σ is such that no collisions exist for all $\nu + \theta$.

We therefore proceed by defining a non-singular averaging canonical transformation $\mathcal{C}$, conjugating the Hamiltonian

$$\widehat{\mathcal{H}} = \widehat{\mathcal{H}}_0 + \varepsilon\widehat{\mathcal{H}}_1$$

to its resonant normal form:

$$\tilde{\mathcal{H}} = \widehat{\mathcal{H}}^{Res}(N, S, \Theta, \sigma) + \varepsilon^2\widehat{R}(S, N, \sigma, \nu+\theta) \tag{3.30}$$

$$\widehat{\mathcal{H}}^{Res} := \widehat{\mathcal{H}}_0(N, S, \Theta) + \varepsilon\widehat{\mathcal{H}}_1^{Res}(S, N, \sigma), \tag{3.31}$$

so that the averaged Hamiltonian $\widehat{\mathcal{H}}^{Res}$ depends on the actions and on the resonant angle σ, while the dependence on the fast angle $\nu+\theta$ is relegated to the remainder $\varepsilon^2\widehat{R}$.

Remark. When resonance overlapping is absent, the dynamics in MMR is approximated with the dynamics of the integrable Hamiltonian $\widehat{\mathcal{H}}^{Res}$, namely the averaged Hamiltonian, which is obtained from the normal form Hamiltonian $\tilde{\mathcal{H}}$ by neglecting the term $\varepsilon^2\widehat{R}$. The analysis of the dynamics of the averaged Hamiltonian has been done in the literature by noticing that N, Θ are first integrals for the Hamiltonian flow of $\widehat{H}^{Res}$. In particular, for given values of N, the Hamiltonian flow follows the level curves of $\widehat{\mathcal{H}}^{Res}$ (the values of Θ are irrelevant) in the plane of the variables S, σ (or related coordinates). For $N > N_c$, the averaged Hamiltonian is not defined on the singular set [Bea94, MorTM95, Tho98], thus breaking the integrability of the problem and opening the door to the generation of complex orbits. To study these complex orbits we compute, in addition to the averaged Hamiltonian, the averaging transformations in the domain where they are not singular.

We define the averaging transformation $\mathcal{C}$ as the Hamiltonian flow at time 1 of the generating function $\varepsilon\chi$, where χ is given by:

$$\chi = \sum_{k\geq 1} \left[b_k(S, N, \sigma) \sin(k(\nu+\theta)) + d_k(S, N, \sigma) \cos(k(\nu+\theta)) \right]$$

where the coefficients b_k and d_k are defined by:

$$b_k = \frac{c_k}{k\left(\frac{\partial \widehat{\mathcal{H}}_0}{\partial N} + \frac{\partial \widehat{\mathcal{H}}_0}{\partial \Theta}\right)}, \quad d_k = -\frac{s_k}{k\left(\frac{\partial \widehat{\mathcal{H}}_0}{\partial N} + \frac{\partial \widehat{\mathcal{H}}_0}{\partial \Theta}\right)}.$$

The Lie transform of $\widehat{\mathcal{H}}$ provides the resonant normal form Hamiltonian:

$$\tilde{\mathcal{H}} = \exp(\mathcal{L}_{\varepsilon\chi})\widehat{\mathcal{H}} = \widehat{\mathcal{H}}_0 + \varepsilon\widehat{\mathcal{H}}_1 + \varepsilon\{\widehat{\mathcal{H}}_0, \chi\} + \mathcal{O}(\varepsilon^2)$$

where $\{\cdot,\cdot\}$ denotes the Poisson brackets, $\mathcal{L}_{\varepsilon\chi}\cdot := \{\cdot, \varepsilon\chi\}$ the Lie derivative with respect to χ, and

$$\exp(\mathcal{L}_{\varepsilon\chi}) = \sum_{s\geq 0} \frac{1}{s!}\mathcal{L}^s_{\varepsilon\chi}$$

is the Lie transform of a function defined by the Hamiltonian $\varepsilon\chi$ at time 1. From standard Hamiltonian perturbation theory the coefficients b_k and d_k have been chosen in order to simplify the first order term $\varepsilon\widehat{\mathcal{H}}_1 + \varepsilon\{\widehat{\mathcal{H}}_0, \chi\}$ as much as possible.

Indeed, since we have:

$$\begin{aligned}\{\widehat{\mathcal{H}}_0, \chi\} &= -\frac{\partial \widehat{\mathcal{H}}_0}{\partial S}\frac{\partial \chi}{\partial \sigma} - \frac{\partial \widehat{\mathcal{H}}_0}{\partial N}\frac{\partial \chi}{\partial \nu} - \frac{\partial \widehat{\mathcal{H}}_0}{\partial \Theta}\frac{\partial \chi}{\partial \theta} \\ &= -\sum_{k\in\mathbb{Z}} \left(\frac{\partial \widehat{\mathcal{H}}_0}{\partial S}\right) \left[\frac{\partial b_k}{\partial \sigma}\sin(k(\nu+\theta)) + \frac{\partial d_k}{\partial \sigma}\cos(k(\nu+\theta))\right] \\ &\quad - \sum_{k\in\mathbb{Z}} \left(\frac{\partial \widehat{\mathcal{H}}_0}{\partial N} + \frac{\partial \widehat{\mathcal{H}}_0}{\partial \Theta}\right) [k b_k \cos(k(\nu+\theta)) - k d_k \sin(k(\nu+\theta))]\end{aligned}$$

we obtain:

$$\widehat{\mathcal{H}}_1 + \{\widehat{\mathcal{H}}_0, \chi\} = c_0(S, N, \sigma) - \left(\frac{\partial \widehat{\mathcal{H}}_0}{\partial S}\right) \sum_{k_1\neq 0} \left[\frac{\partial b_k}{\partial \sigma}\sin(k(\nu+\theta)) + \frac{\partial d_k}{\partial \sigma}\cos(k(\nu+\theta))\right]$$

Therefore, at order ε in the Hamiltonian, we remain with the sum of c_0, which does not depend on the angle $\nu+\theta$, and a term depending on σ but proportional to the function $\frac{\partial \widehat{\mathcal{H}}_0}{\partial S}$, which is small in the domain of the $p:q$ resonance, up to order $\sqrt{\varepsilon}$. Therefore, the normal form Hamiltonian has the form [3]:

$$\tilde{\mathcal{H}} = \widehat{\mathcal{H}}_0(S, N, \Theta) + \varepsilon \widehat{\mathcal{H}}_1^{Res}(S, N, \sigma) + \mathcal{O}(\varepsilon^{\frac{3}{2}}). \tag{3.32}$$

We remark that, only apparently, the averaging that we have defined here is less effective than the normal form written in Eq. (3.30), whose remainder is indicated as $O(\varepsilon^2)$. The coefficient ε^2 in Eq. (3.30) comes from the series development of the Lie transform with respect to the small parameter ε, but does not take into account that the functions multiplying ε^2 contain small divisors that, in the domain of the resonance, are bounded from below by suitable powers of ε; as a consequence, the real bound for the norm of the remainder is in the open interval $(\varepsilon, \varepsilon^2)$, as for the normal form provided in Eq. (3.32). The precise estimate of the remainders of the normal forms can be done within the framework of the Nekhoroshev theorem, which allows to iterate the construction of the normal form up to remainders which are exponentially small with respect to the perturbation parameter ε (we refer to [MorG97, Mor02] for detailed discussions about the application of the Nekhoroshev theorem to restricted three-body problems).

The canonical transformation from the normal form variables (indicated with a

[3] Please notice that the second term in the previous equation is here multiplied by ε, and therefore is represented as $\mathcal{O}(\varepsilon^{3/2})$. Also, to use a lighter notation, we drop the tildes from the normal form variables.

$\sim$ symbol) to the original ones may be computed as usual using the Lie transform,

$$\begin{aligned}
S &= \exp(\mathcal{L}_\chi^\varepsilon)\tilde{S} = \tilde{S} - \varepsilon\frac{\partial\chi}{\partial\tilde{\sigma}} + \mathcal{O}(\varepsilon^2), \qquad \sigma = \exp(\mathcal{L}_\chi^\varepsilon)\tilde{\sigma} = \tilde{\sigma} + \varepsilon\frac{\partial\chi}{\partial\tilde{S}} + \mathcal{O}(\varepsilon^2)\\
N &= \exp(\mathcal{L}_\chi^\varepsilon)\tilde{N} = \tilde{N} - \varepsilon\frac{\partial\chi}{\partial\tilde{\nu}} + \mathcal{O}(\varepsilon^2), \quad \nu = \exp(\mathcal{L}_\chi^\varepsilon)\tilde{\nu} = \tilde{\nu} + \varepsilon\frac{\partial\chi}{\partial\tilde{N}} + \mathcal{O}(\varepsilon^2)\\
\Theta &= \exp(\mathcal{L}_\chi^\varepsilon)\tilde{\Theta} = \tilde{\Theta} - \varepsilon\frac{\partial\chi}{\partial\tilde{\theta}} + \mathcal{O}(\varepsilon^2), \qquad \theta = \tilde{\theta}
\end{aligned} \tag{3.33}$$

where the higher order terms $\mathcal{O}(\varepsilon^2)$ will not be included in the explicit computations of Section 4, and the derivatives of χ with respect to resonant variables are computed using the formulas:

$$\begin{aligned}
\frac{\partial\chi}{\partial S} &= \sum_{k\geq 1}\frac{\partial b_k}{\partial S}(S,N,\sigma)\sin\left(k(\nu+\theta)\right) + \sum_{k\geq 1}\frac{\partial d_k}{\partial S}(S,N,\sigma)\cos\left(k(\nu+\theta)\right)\\
\frac{\partial\chi}{\partial N} &= \sum_{k\geq 1}\frac{\partial b_k}{\partial N}(S,N,\sigma)\sin\left(k(\nu+\theta)\right) + \sum_{k\geq 1}\frac{\partial d_k}{\partial N}(S,N,\sigma)\cos\left(k(\nu+\theta)\right)\\
\frac{\partial\chi}{\partial \sigma} &= \sum_{k\geq 1}\frac{\partial b_k}{\partial \sigma}(S,N,\sigma)\sin\left(k(\nu+\theta)\right) + \sum_{k\geq 1}\frac{\partial d_k}{\partial \sigma}(S,N,\sigma)\cos\left(k(\nu+\theta)\right)\\
\frac{\partial\chi}{\partial\nu} = \frac{\partial\chi}{\partial\theta} &= \sum_{k\geq 1} k b_k(S,N,\sigma)\cos\left(k(\nu+\theta)\right) - \sum_{k\geq 1} k d_k(S,N,\sigma)\sin\left(k(\nu+\theta)\right)
\end{aligned}$$

where the derivatives of b_k and d_k with respect to S, N, σ can be obtained from derivative of c_k and s_k which are computed numerically as follows. Let $D_k := k\left(\frac{\partial\widehat{\mathcal{H}}_0}{\partial N} + \frac{\partial\widehat{\mathcal{H}}_0}{\partial\Theta}\right)$, then we have

$$\begin{aligned}
\frac{\partial b_k}{\partial S} &= \frac{1}{D_k^2}\left(\frac{\partial c_k}{\partial S}D_k - c_k\frac{\partial D_k}{\partial S}\right), \qquad \frac{\partial b_k}{\partial N} = \frac{1}{D_k^2}\left(\frac{\partial c_k}{\partial N}D_k - c_k\frac{\partial D_k}{\partial N}\right)\\
\frac{\partial d_k}{\partial S} &= -\frac{1}{D_k^2}\left(\frac{\partial s_k}{\partial S}D_k - s_k\frac{\partial D_k}{\partial S}\right), \qquad \frac{\partial d_k}{\partial N} = -\frac{1}{D_k^2}\left(\frac{\partial s_k}{\partial N}D_k - s_k\frac{\partial D_k}{\partial N}\right)
\end{aligned}$$

and

$$\frac{\partial b_k}{\partial\sigma} = \frac{1}{D_k}\frac{\partial c_k}{\partial\sigma}, \quad \frac{\partial d_k}{\partial\sigma} = -\frac{1}{D_k}\frac{\partial s_k}{\partial\sigma}$$

where the derivatives of c_k and s_k with respect to action variables S, N, σ are obtained from the Fourier expansions of the derivatives of $\widehat{\mathcal{H}}_1$ with respect to S, N, σ.

3.3 Numerical explorations

In this Section we provide an example of the analysis of the dynamics in a selected MMR for increasing values of the action N (corresponding to increasing values of the eccentricity) up to values that include orbits of P crossing the orbit of P_1 and beyond. We consider values of the mass ratios which are representative of the Sun-Jupiter and Sun-Neptune cases, but since the circular restricted three-body problem represents an approximation of the real problem, we prefer to use the approximated values for the mass ratios $10^{-3}, 0.0000515139$. A complete analysis of the dynamics of the 1:2 MMR with Jupiter is provided up to values of the eccentricity $e \sim 0.55$; some comparisons with the 1:2 and 5:6 MMR with Neptune will also be supplied.

Note that in the numerical explorations we compute the time evolutions of the averaged variables for the complete Hamiltonian of the restricted three-body problem (not only the averaged one). Therefore, the effects of the remainders of the normal forms show up, and those quantities which are constant in the normal form approximation such as the values of averaged action N and of the averaged Hamiltonian, indeed may evolve with time.

3.3.1 Analysis of the 1:2 MMR with Jupiter

In this Subsection we describe the dynamics in the selected 1:2 MMR for $\varepsilon = 10^{-3}$ and for increasing values of the action N up to values that include orbits of P crossing the orbit of P_1 and beyond (correspondingly, we consider increasing values of the eccentricity up to $e \sim 0.55$). For the 1:2 MMR the critical value of N for the appearance of tangent and crossing orbits is $N_c \sim -1.0852$. The study will be done by comparing the phase-portraits of the averaged Hamiltonian (see Eq. (3.31)):

$$\widehat{\mathcal{H}}^{Res} := \widehat{\mathcal{H}}_0(N, S, \Theta) + \varepsilon \widehat{\mathcal{H}}_1^{Res}(S, N, \sigma)$$

in the resonant plane $x = \sqrt{2S}\cos\sigma, y = \sqrt{2S}\sin\sigma$ with the computation of regularized Fast Lyapunov Indicators for large grids of initial conditions of the same plane. For selected initial conditions we also compare the time evolution of the averaged variables $\tilde{N}, \tilde{S}, \tilde{\sigma}$, defined in Eq. (3.33), with the time evolution of N, S, σ. We identify the dynamical regimes described below for some representative values of N (for different resonances and different values of the mass ratios the regimes appear at different values of N, see Subsection 4.4.2 for examples).

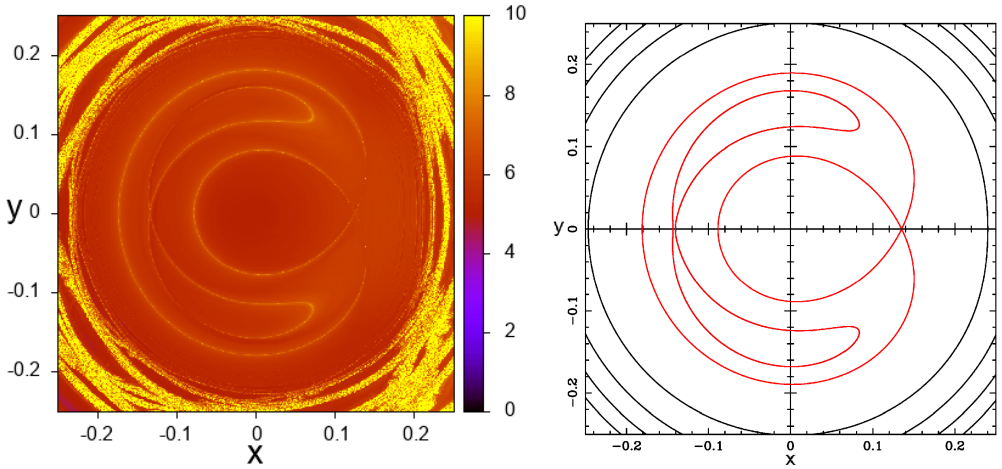

Figure 3.7: Left panel: phase portrait of 1:2 MMR with Jupiter for $N = -1.24$. Right panel: values of the regularized FLI computed on the x-y plane for $T = 800$ (initial conditions: x, y given by the position on the panel, $N = -1.24$, $\nu = \pi$, $\theta = 0$). Numerical examples of resonant dynamics are represented in Fig. 3.8.

The isolated resonance regime. When the values of N are small enough, the singular set is empty so there are no orbits of P tangent to or crossing the orbit of P_1, and close encounters of P with P_1 are not possible. This regime has been studied for a long time, and it is well known that the averaged Hamiltonians represent accurately the resonant dynamics. The effects of the normal form remainder, which acts as a small perturbation of the averaged Hamiltonian, can be studied using Hamiltonian perturbation theory: chaotic motions appear in a neighborhood of the separatrix of the normal form, while the persistence of resonant librations and circulations as invariant tori could be studied using KAM theorem. This regime has been identified in [Bea94] for the moderately large value of $N = -1.24$ of the 1:2 MMR with Jupiter. For this value, we compare the phase-portrait of the resonance with the picture obtained by computing the values of the regularized FLI for $x, y \in [-0.25 : 0.25]$ (corresponding to $e \in [0, 0.217..]$; see Fig. 3.7). The left panel of Fig. 3.7 (the phase-portrait) provides the localization of the equilibria as well as of the separatrices joining the unstable equilibria of the averaged Hamiltonian $\widehat{\mathcal{H}}^{Res}$ for the variables S, σ; the right panel reports the values of the regularized FLI computed by numerically integrating the equations of motion of the CR3BP represented with the Levi-Civita regularization up the time $T = 800$ (see subsection 3.3.3 for technical details and references about the regularized FLI).

The distribution of the values of the FLI inside the disk $|(x, y)| \leq 0.2$ is in agreement with the computation of the phase-portrait of the averaged Hamilto-

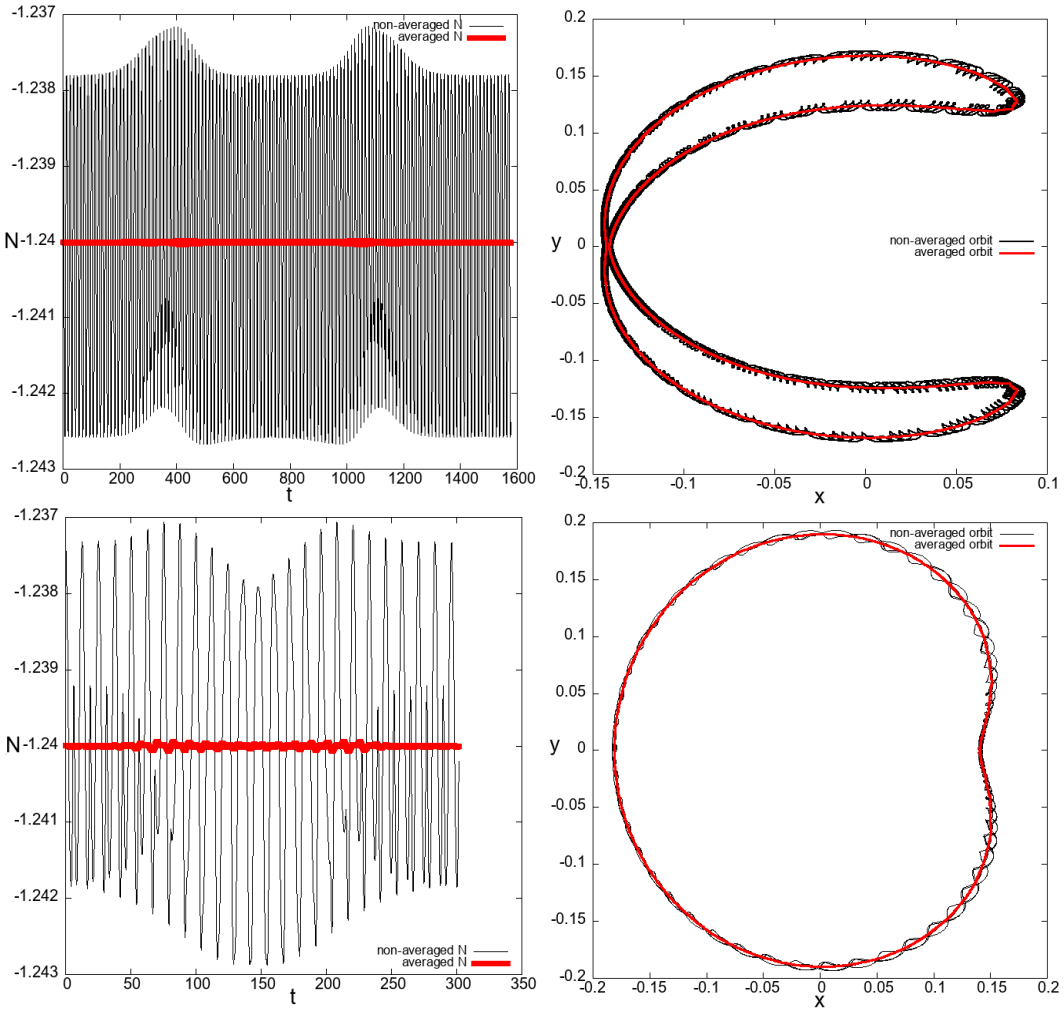

Figure 3.8: Top panels: time evolution of averaged (red) and non-averaged (black) value of N for a sample orbit (left panel) whose projection on the x-y plane is represented on the top-right panel (initial conditions: $\tilde{x} = -0.141, \tilde{y} = 0$); along the numerical integration we find $|P - P_1| \geq 0.5$. Bottom panels: same computations as in the top panels but for the orbit with initial condition $\tilde{x} = 0.141, \tilde{y} = 0$; along the numerical integration we find $|P - P_1| \geq 0.3$. The phase-portrait is given in Fig. 3.7.

nian: the separatrices are replaced by a yellow set (which identify the orbits with initial conditions providing the largest values of the FLI) which, in the complete equations of motion of the CR3BP, identify chaotic motions generated by the stable/unstable manifolds of resonant hyperbolic invariant tori. These manifolds are embedded in a region of regular motions, identified by orange color in the pic-

ture. The effect of nearby resonances is seen as the appearance of a large region of chaotic motions (still identified by yellow color in the picture) for $|(x, y)| > 0.2$.

These computations provide the indication that the averaging method is effective for the resonant motions inside the disk $|(x, y)| \leq 0.2$. In the panels of Fig. 3.8 we represent the time evolution of the original and averaged actions $N, \tilde{N}$ and the projection of the original and averaged variables (x, y) and $(\tilde{x}, \tilde{y})$ on the phase-plane, for two selected initial conditions inside the 1:2 resonance. The sharp reduction of oscillations in the time evolution of $\tilde{N}$, and also in the projection of the averaged orbits, confirm the efficiency of the averaging method for this regime.

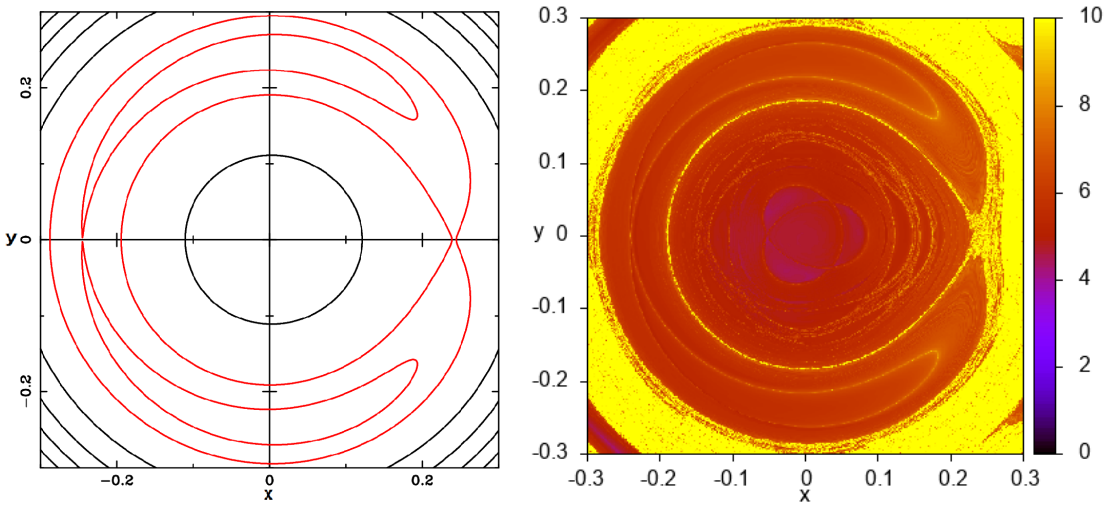

Figure 3.9: Left panel: Phase-portrait of 1:2 MMR with Jupiter for $N = -1.20$. Right panel: values of the regularized FLI computed on x-y plane for $T = 800$ (and $\nu = \pi$, $\theta = 0$). Numerical examples of resonant dynamics are represented in Fig. 3.10.

A regime in which the external separatrix belongs to an extended chaotic region. As the value of N slightly increases, we find that the region of regular motions separating the external separatrix from the large chaotic region disappears and incorporates the stable/unstable manifolds corresponding to the unstable equilibrium point of the resonance identified at $\sigma = 0$. This is evident already for $N = -1.20$, for which we represent phase portrait and the values of the regularized FLI in the panels of Fig. 3.9. In this regime, we expect that the averaging method is more effective for the resonant motions which are suitably far from the large external chaotic region. The top and bottom panels of Fig. 3.10 represent the time evolution of the original and averaged actions $N, \tilde{N}$ and the

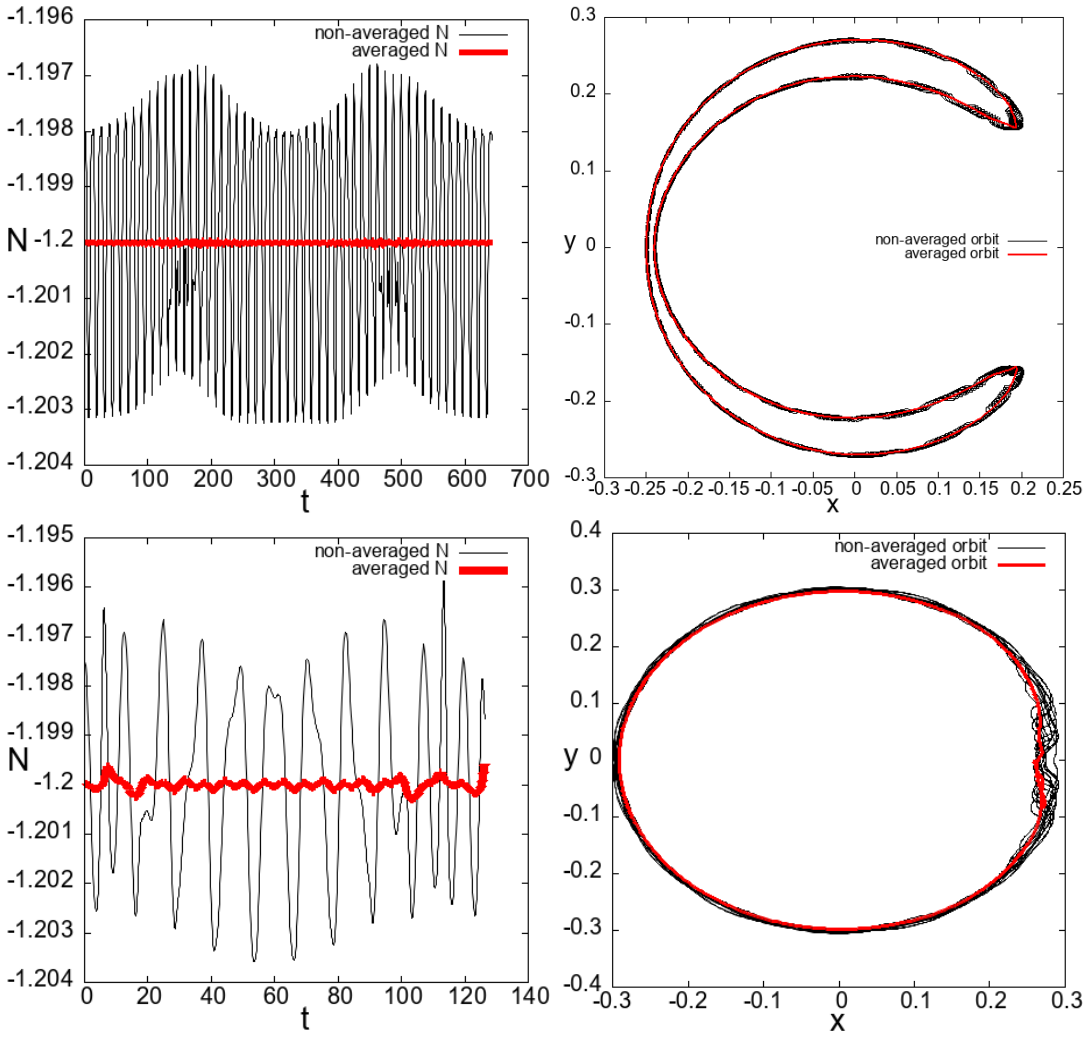

Figure 3.10: Numerical examples of resonant dynamics related to the phase-portrait and the regularized FLI representation of Fig. 3.9. Top panels: time evolution of averaged and non-averaged value of N for a sample orbit (left panel) whose projection on the x-y plane is represented on the top-right panel (the initial condition is $\tilde{x} = -0.240, \tilde{y} = 0$); along the numerical integration we find $|P - P_1| \geq 0.48$. Bottom panels: same computations as in the top panels but for a different orbit (the initial condition is $\tilde{x} = 0.260, \tilde{y} = 0$); along the numerical integration we find $|P - P_1| \geq 0.2$.

projection of the original and averaged variables (x, y) and $(\tilde{x}, \tilde{y})$ on the phase-plane, for two selected initial conditions inside the resonance. Indeed, from the sharp reduction of the oscillations that we observe in the top panels in the time evolution of $\tilde{N}$, and in the projection of the averaged orbit, we appreciate the

efficiency of the averaging method for this orbit. It is interesting to remark that also for the chaotic orbit of the bottom panels, which is embedded in the large chaotic area, we still notice a reduction of the oscillations in the time evolution of $\tilde{N}$ with respect to N, even if the efficiency of such a reduction is smaller with respect to the previous case. Also the averaged projected orbit represented in the bottom-right panel shows some irregularities which were not present in the orbit represented in the top-right panel.

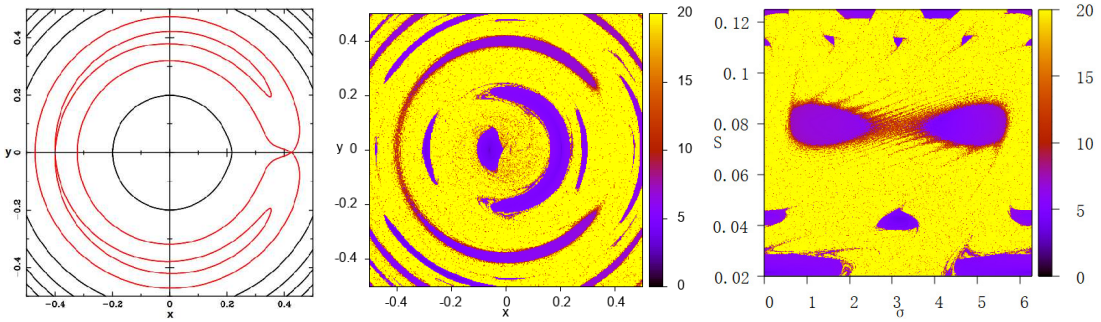

Figure 3.11: Left panel: Phase-portrait of 1:2 MMR with Jupiter for $N = -1.10$. Center panel: values of the regularized FLI computed for $T = 800$ represented on the x-y plane ($\nu = \pi$, $\theta = 0$). Right panel: values of the FLI represented on the σ-S plane (the interval of the action S is adapted to the 1:2 resonance).

A regime in which also the internal separatrix merges to the extended chaotic region. As N further increases, we find that also the stable/unstable manifolds associated to the hyperbolic torus with $\sigma = \pi$ are embedded in the large chaotic region, and regular motions are found only in the two regions of resonant librations. We find that this regime occurs for values of N which are below the critical value $N_c \sim -1.085$ for the appearance of the singular set (see also Fig. 3.20). Therefore, even if the singular set is empty, we may have close encounters which possibly produce variations of N which increase its value above N_c. In this case, we find that chaotic diffusion and close encounters play a relevant role to shape the dynamics, which is only marginally represented by the phase-portrait of the averaged Hamiltonian. Nevertheless we find that, except for the time intervals where deep close encounters of P with P_1 occur, the canonical transformation defined in Section 3.2 remains still effective, and can be used to study these chaotic diffusions.

In Fig. 3.11 we represent the phase-portrait of the averaged Hamiltonian (left panel) and the values of the regularized FLI for $N = -1.10$ (center and left panels). We clearly appreciate the large chaotic region of the resonant phase-plane as well

as the two regions of motions which are phase–protected from close encounters (these regions are more evident in the FLI representation of the σ-S plane of the right panel).

To display the effects of chaotic diffusion and close encounters we consider an orbit in the chaotic region whose initial condition is very close to the regular region of orbits which are phase-protected from close encounters. So, initially this orbit is phase-protected from deep close encounters, but later on the chaotic diffusion removes the phase-protection and deep close encounters occur. In the top-left panel of Fig. 3.12 we represent the time evolution of the orbit in the time interval $[0, 1800]$, in which the orbit shows a chaotic alternation of resonant librations and circulations which are phase-protected from deep close encounters (in this time interval we have $|P - P_1| \geq 0.4$).

Even in this chaotic scenario canonical perturbation theory remains effective and can be used to study the chaotic diffusion of N and $\widehat{\mathcal{H}}^{Res}$. In fact, the top-right panel of Fig. 3.12 shows a sharp reduction in the oscillations of the averaged action $\tilde{N}$ with respect to the non-averaged action N. The effectiveness of canonical perturbation theory is enough to represent the chaotic diffusion of $N, \widehat{\mathcal{H}}^{Res}$: while the oscillations of the original action variable N are so large to mask its chaotic diffusion, the variations of the averaged action $\tilde{N}$, represented with a zoom in the bottom-left panel, show a chaotic deviation for the reference value $N = -1.10$.

The alternation of resonant librations and circulations is due to the chaotic diffusion of the value of the averaged Hamiltonian (3.30), represented in the bottom-right panel of Fig. 3.12 (violet line): the evolution of this function is characterized by time intervals where it has almost constant values, followed by an oscillation at the end of which the function stabilizes on a different quasi-constant value. The sequence of these quasi-constant values appears to be random, and this kind of chaotic diffusion is qualitatively similar to the Arnold diffusion detected in the single resonances of a model Hamiltonian system in the paper [GuzEP20], Figs. 1, 5-7. On the same panel, we also represent the value of the averaged Hamiltonian corresponding to the separatrix, computed for each value of $\tilde{N}(t)$ (green line). The computation shows that, in the considered time interval, the chaotic diffusion moves the value of the averaged energy above or below the reference value for the separatrix, thus showing the efficacy of canonical perturbation theory in representing the phenomenon of adiabatic change of resonant librations into resonant circulations and back.

We remark that the accumulation of the chaotic diffusion in the values of the averaged Hamiltonian may remove the phase-protection from close encounters, while the chaotic diffusion of N may increase its value above N_c. This happens for the orbit represented in Fig. 3.13 on a longer time interval: in the top-left

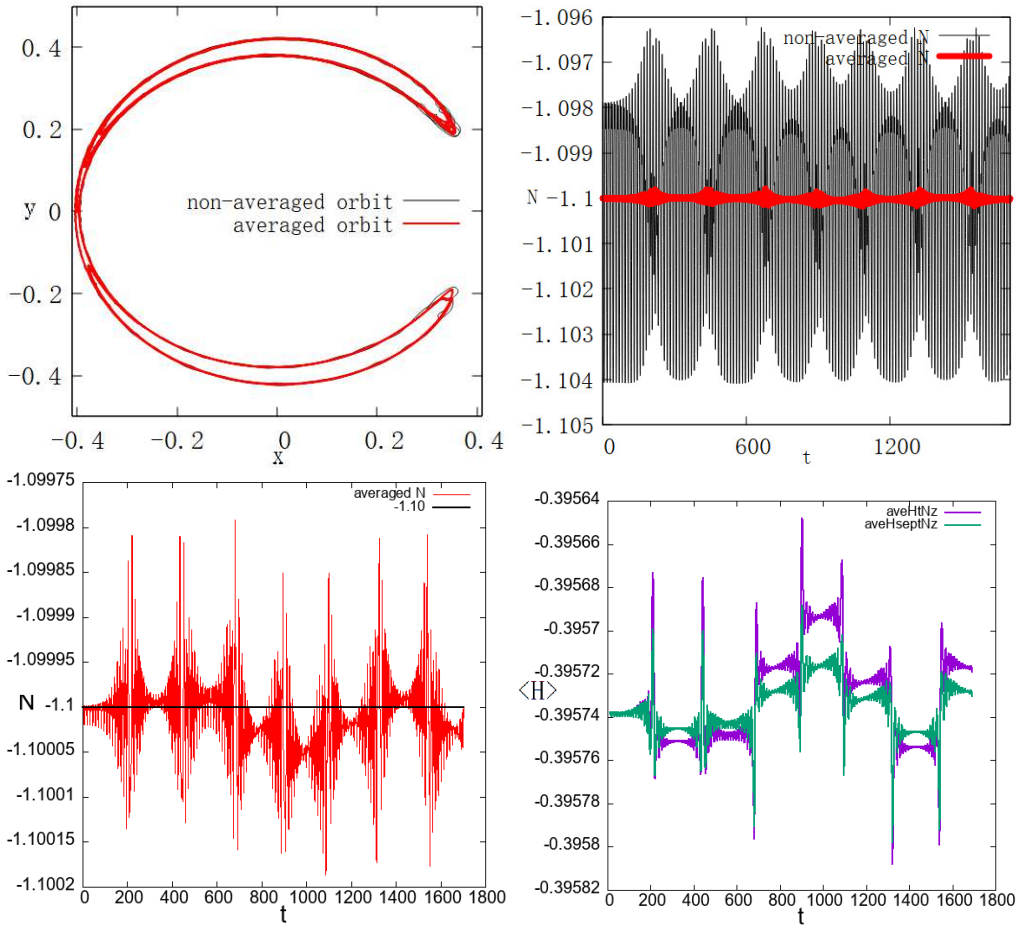

Figure 3.12: Top-left panel: Projection on the x-y plane of a sample orbit of the 1:2 MMR with Jupiter for $N = -1.10$ (initial conditions: $\tilde{x} = -0.400, \tilde{y} = 0$), and for $t \in [0, 1800]$; the non-averaged values (x, y) are plotted with a black line, the averaged values $(\tilde{x}, \tilde{y})$ with a red line. Top-right panel: time evolution of the averaged (red line) and non-averaged (black line) values of N. Bottom-left Panel: zoomed in view of the time evolution of the averaged values of N. Bottom-right panel: time evolution of the averaged Hamiltonian (violet line) and its value corresponding to the separatrix computed for each value of $\tilde{N}(t)$ (green line); to better appreciate the chaotic diffusion a running average of the numerical data has been applied (with window $\Delta t = 100$).

panel we represent the same orbit for a longer time interval (blue for $t < 3000$ and red for $t > 3000$), while in the top-right panel (blue for $t \leq 3000$ and red for $t > 3000$) we see that the distance from P_1 is experiencing smaller and smaller local minima with a close encounter at about $t = 3000$ and a deeper one at the

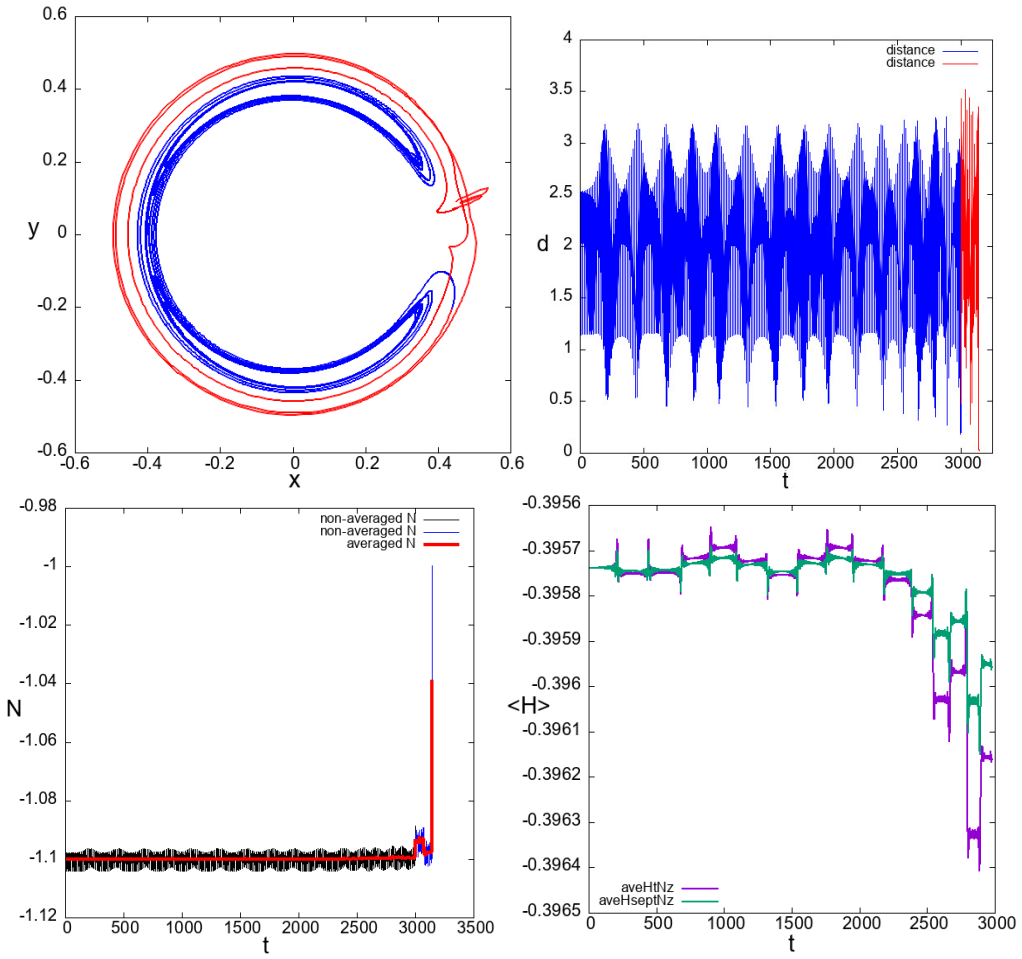

Figure 3.13: Analysis of the same orbit of Fig. 3.12 for a longer time interval. Top panels: projection of the averaged values $(\tilde{x}, \tilde{y})$ (left) and time evolution of the distance $d := \|P - P_1\|$ (right). Bottom-left panel: time evolution of the non averaged (black and blue) and averaged (red) values of N. Bottom-right panel: time evolution of the averaged Hamiltonian (violet line) and of the value of the averaged Hamiltonian corresponding to the separatrix. Projections of the orbits on the σ-S plane are represented in Fig. 3.14.

end of the interval. In the bottom-left panel we appreciate the chaotic diffusion of $\tilde{N}$ (bottom-left panel, non averaged indicated by black line for $t < 3000$ and blue line for $t > 3000$, and averaged N by red line). In the bottom-right panel we represent the time evolution of the averaged Hamiltonian (violet line) and of the value of the averaged Hamiltonian corresponding to the separatrix, computed for each value of $\tilde{N}(t)$ (green line); a running average of the numerical data has been applied with window $\Delta t = 100$. It is remarkable that the canonical transformation

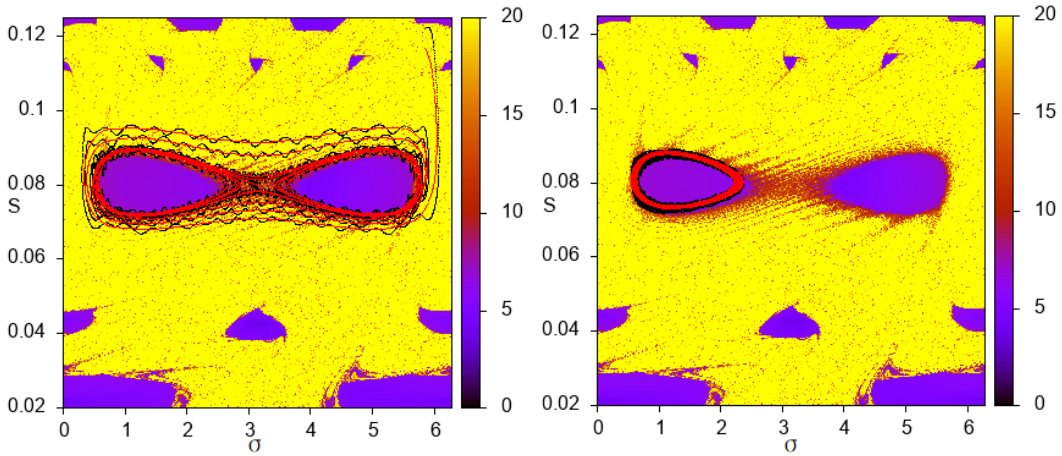

Figure 3.14: Projections of orbits from Fig. 3.13. Left panel: projection of the non averaged (black) and averaged (red) orbit on the σ-S plane (with values of the regularized FLI on the background). Right panel: projection on the σ-S plane of the non averaged (black) and averaged (red) orbit of an initial condition in the region of regular resonant librations.

defined in Section 3.2 is still effective (since it still reduces the oscillations of $\tilde{N}$ with respect to the oscillations of N) except for $t > 3000$ where we find the close encounters. In the left panel of Fig. 3.14 we represent the projection on the resonant phase-plane (σ, S) of the non-averaged (black line) and averaged (red line) values of σ, S; the values of the regularized FLI are represented in the background. We clearly appreciate the chaotic increments of the amplitude of the resonant circulations, leading to the deep close encounters. The efficacy of perturbation theory in removing the oscillations from the projected orbit is clear as well. In the right panel of of Fig. 3.14 we represent the projection on the resonant phase-plane (σ, S) of the non-averaged (black line) and averaged (red line) values of σ, S for a different orbit, whose initial condition is located in the region of the regular resonant librations.

The regime of crossing orbits. For values of N far beyond the critical value N_c, such as $N = -0.85$, we have orbits which cross the the orbit of P_1 (far from the tangency), and in the phase-portrait (Fig. 3.15, right panel) we have the appearance of a curve corresponding to the singular set $\mathcal{S}_{0,0}$ defined in Eq. (3.20). The computation of the regularized FLI (Fig. 3.15, left panel) shows a large chaotic region, with the only regular resonant motions which are phase-protected from close encounters surviving in it, which are better identified in the bottom panels of Fig. 3.16 (where the FLI are represented in the σ-S plane). In these panels we also identify the set of close encounters $\mathcal{S}_{d,0}$, with $d = \pm\mu^{\frac{1}{3}}$ (green and

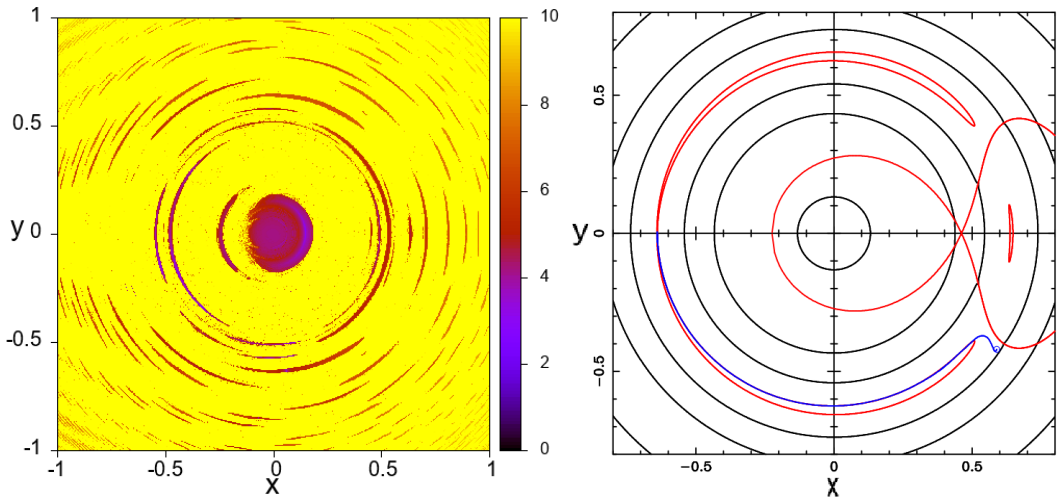

Figure 3.15: Dynamics in the 1:2 MMR with Jupiter for $N = -0.85$. Left panel: values of the FLI computed on the x-y plane for $T = 800$. Right panel: projection of the averaged orbit (blue line) on the x-y phase portrait with the singular set (initial conditions: $\tilde{x} = -0.640, \tilde{y} = 0$); the initial value for the eccentricity of this orbits is $e \sim 0.55$. See Fig. 3.16 for additional information.

blue lines) as well as the set corresponding to the points of the plane of Fig. 3.2 (left column), identifying the domain where the Fourier transform of the perturbation was inaccurate for more than 10 per cent (the black area). For Jupiter, the border of this area corresponds closely to the sets delimited by $\mathcal{S}_{\mu^{\frac{1}{3}},0}$ and $\mathcal{S}_{-\mu^{\frac{1}{3}},0}$. It is remarkable that the chaotic motions extend to a larger distance from $\mathcal{S}_{0,0}$. Also in this regime, we have orbits that initially are phase-protected from close encounters, but then approach the singular set and have a large variation of N (right panel of Fig. 3.15 and bottom-left panels of Fig. 3.16). The canonical transformation defined in Section 3.2 remains effective up to the deep close encounter (top and bottom-left panels of Fig. 3.16).

3.3.2 Comparisons with the Sun-Neptune case and the 5:6 resonance

For a given $p : q$ resonance, by reducing the value of the mass-ratio ε we reduce the amplitude of the resonance, the radius of the Hill's sphere and the chaos due to the nearby resonances. For example, in Fig. 3.17, we represent the values of the regularized FLI on the plane of the resonant action-angle variable σ-S for the 1:2 MMR, $N = -1.06$, $\varepsilon = 10^{-3}$ (left panel) and $\varepsilon = 0.0000515139$ (right panel). Apart from the properties which scale with ε in a straightforward way (such as the amplitudes of the separatrices of the resonance and of the region of

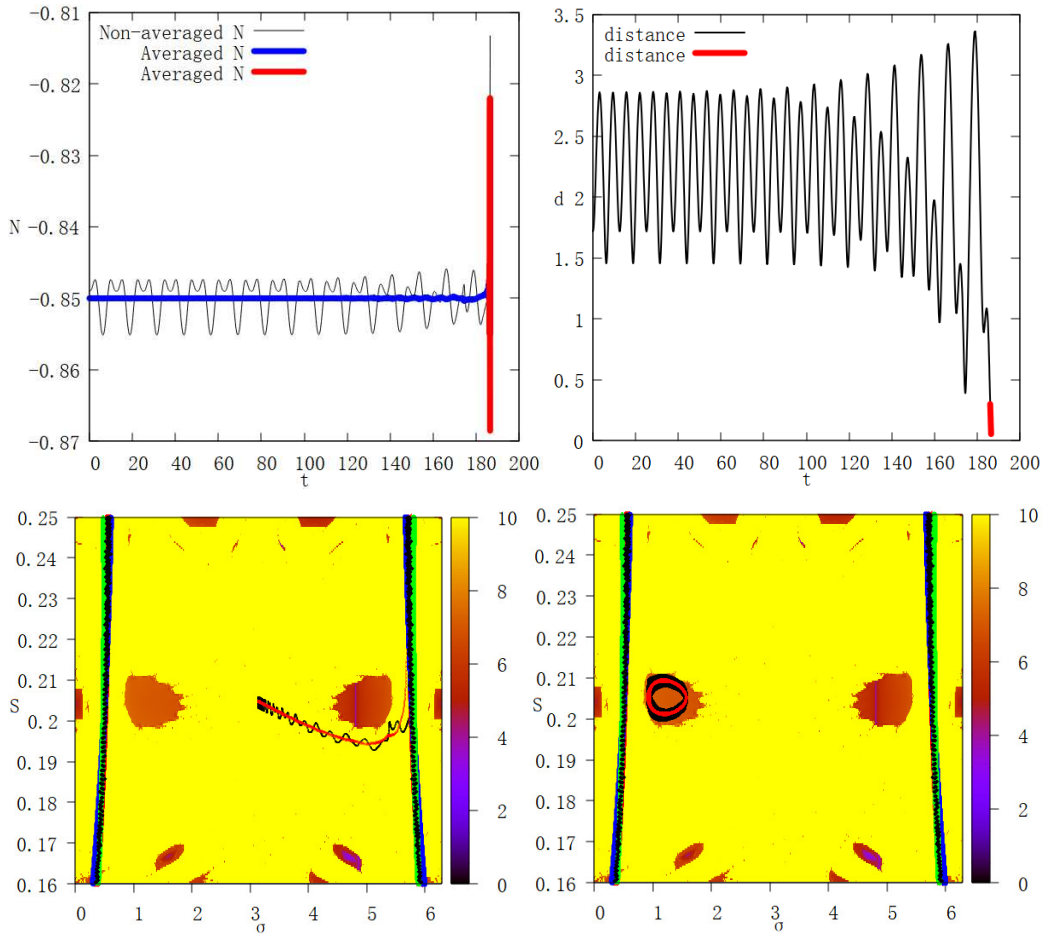

Figure 3.16: Dynamics in the 1:2 MMR with Jupiter for $N = -0.85$ (see also Fig. 3.15). Top-left panel: time evolution of the non averaged (black line) and averaged (blue for $t \leq 186$, red for $t > 186$) values of N. Top-right panel: time evolution of the distance $d = \|P - P_1\|$ (blue for $t \leq 186$, red for $t > 186$). Bottom-left panel: projection of the non averaged (black) and averaged (red) orbit on the (σ, S) plane; the values of the regularized FLI are plotted on the background. Bottom-right: projection of the non averaged (black) and averaged (red) orbit on the (σ, S) plane for a regular libration. Note that bottom panels also illustrate the sets of close encounters (see the text for more information).

close encounters in the right panel), the panels reveal that for this value of N the dynamics of the Neptune case is still in the regime where the resonance is isolated from the other ones (at variance with the Jupiter case): the separatrices of the resonant normal form are surrounded by a region of regular resonant circulations. Chaotic motions appear close to the set of close encounters for both values of ε.

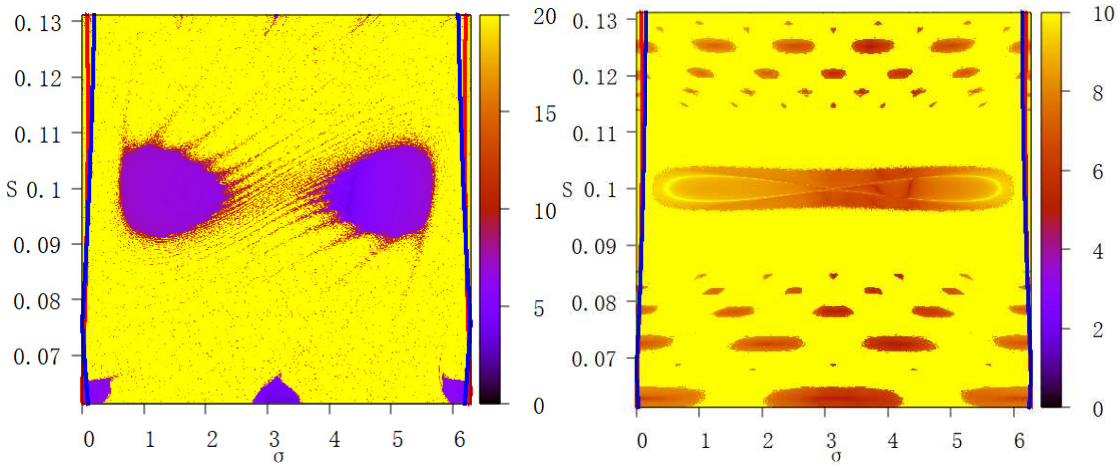

Figure 3.17: Values of the FLI computed on the plane of the resonant action-angle variable σ-S for the 1:2 MMR and for $N = -1.06$ (left panel for Jupiter, $T = 800$; right panel for Neptune, $T = 4000$). Also the curves corresponding the the sets of close encounters computed for $d = \pm\mu^{\frac{1}{3}}$ are represented in red and blue.

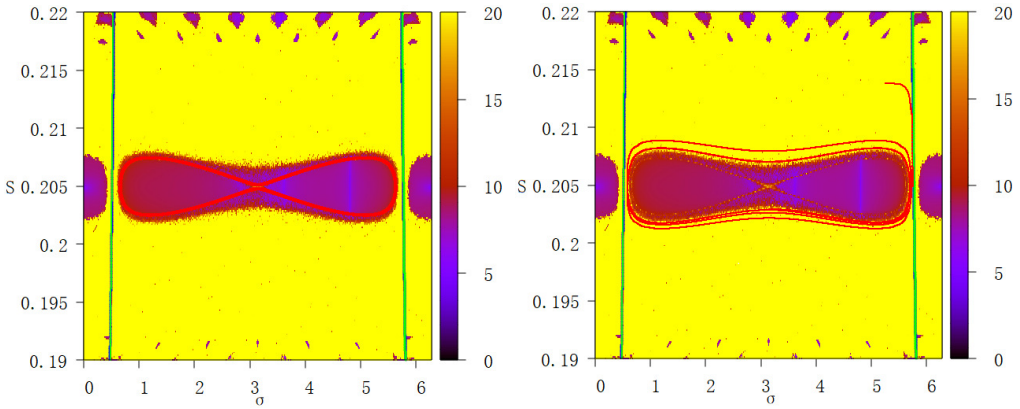

Figure 3.18: Dynamics in the 1:2 MMR resonance with Neptune for $N = -0.85$. Projection of averaged (red lines) orbits on the resonant phase-plane σ-S, with the values of the regularized FLI represented on the background. The left panel refers to a resonant circulation, and the the right panel is related to a chaotic orbit which initially is phase-protected from close encounters. The green and the blue lines represent the set of close encounters computed for $d = \pm\mu^{1/3}$. Additional information is represented in Fig. 3.19.

This happens also for the large value of $N = -0.85$: in Fig. 3.18 we represent the values of the regularized FLI in the plane of the resonant action-angle variables σ-S for the Neptune case and $N = -0.85$, with the projections of two orbits, a regular

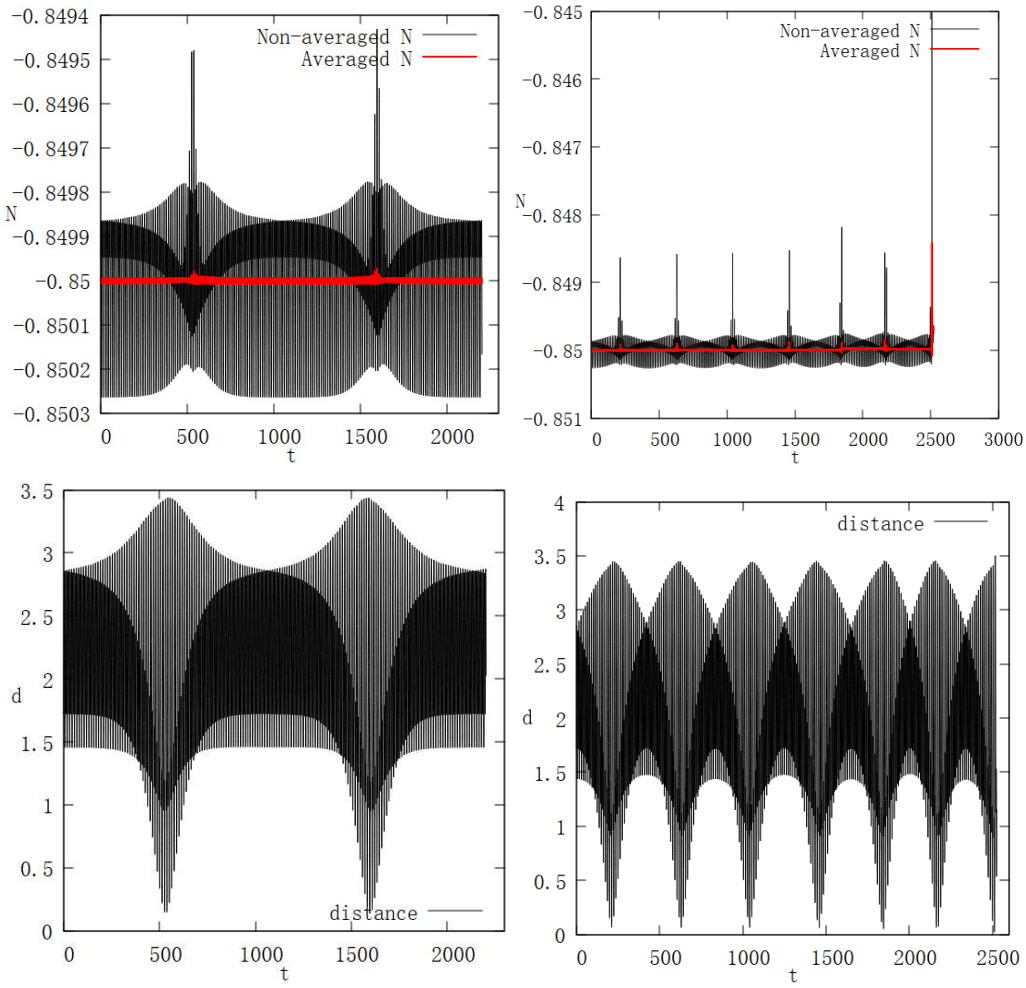

Figure 3.19: Dynamics in the 1:2 MMR resonance with Neptune for $N = -0.85$. All the panels in the left column refer to a resonant circulation (left panel of Fig. 3.18), in the right column to a chaotic orbit which initially is phase-protected from close encounters (right panel of Fig. 3.18). Top panels: time evolution of the non averaged (black line) and averaged (red line) values of N. Bottom panels: time evolution of the distance $d = \|P - P_1\|$.

resonant circulation (left panel) and a chaotic orbit (right panel). For the Neptune case, regular orbits experiencing close encounters exist (bottom-left panel of the Fig. 3.19: the regular orbit experiences close encounters at $d \sim 0.13$). The chaotic orbit (see right panels of Fig. 3.19) shows the same behavior of the chaotic orbits previously discussed for the Jupiter case: initially the orbit circulates around the resonance, with close encounters repeating at $d \sim 0.06$, and when a deep close encounter at $d \sim 0.02$ occurs the orbit experiences a larger chaotic instability.

The efficacy of the canonical transformation defined in Section 3.2 is confirmed for the regular orbits and for the chaotic orbit up to the deep encounter.

A global comparison of the dynamics in the 1:2 MMR with Jupiter and Neptune is provided in Fig. 3.20, where the regularized values of the FLI are represented for both cases for fixed values of S, corresponding to the center of the resonance, while $\sigma \in [0, 2\pi]$ (horizontal axis) , $N \in [-1.20, -0.65]$ (vertical axis) and $\nu, \theta = 0$. The prevalence of chaotic instability for the Jupiter case (left panel) with respect to the Neptune case (right panel) is evident.

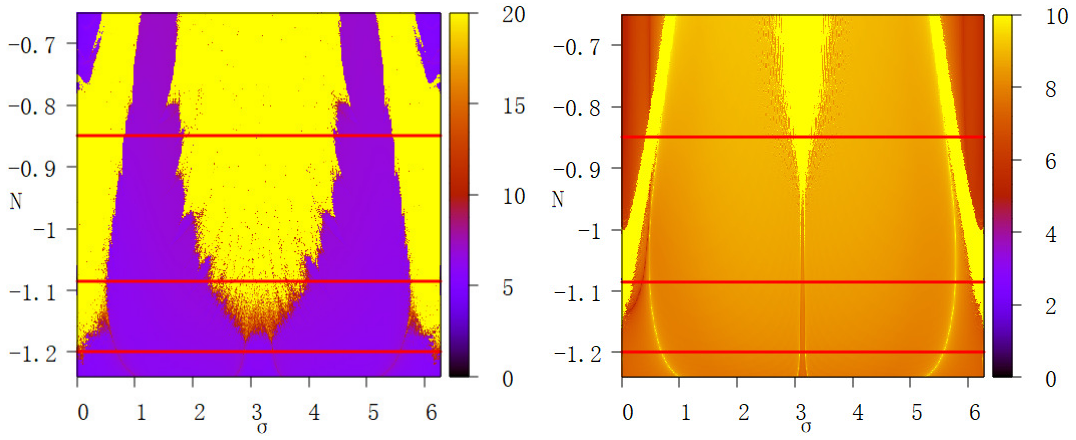

Figure 3.20: Comparison of the dynamics in the 1:2 MMR resonance with Jupiter (left panel) and Neptune (right panel): representation of the values of the regularized FLI for the initial conditions $\sigma \in [0, 2\pi]$ (horizontal axis), $N \in [-1.20, -0.65]$ (vertical axis), S solves $\partial \widehat{\mathcal{H}}_0 / \partial S = 0$, $\nu, \theta = 0$. The reference red lines are plotted for $N = -1.20, -1.085, -0.85$.

Finally, we consider the 5:6 MMR which, due to its vicinity to the singular value $a = 1$, is more perturbed by P_1 than the 1:2 MMR and close encounters and collisions are possible for much lower values of the eccentricity. For this reason, we only consider the Neptune case, for which we compute the regularized values of the FLI for $N \simeq -1.02276$ (the critical value for this resonance) and analyze two orbits, a regular resonant libration, and a chaotic orbit which initially is phase-protected from close encounters (see Fig. 3.21 for the representation of regularized FLI and Fig. 3.22 for the representation of N and of the distance). The FLI computation reveals the prevalence of chaotic motions (at variance with the 1:2 MMR with Neptune), while the efficacy of the canonical transformation defined in Section 3.2 is confirmed up to the occurrence of a deep close encounter.

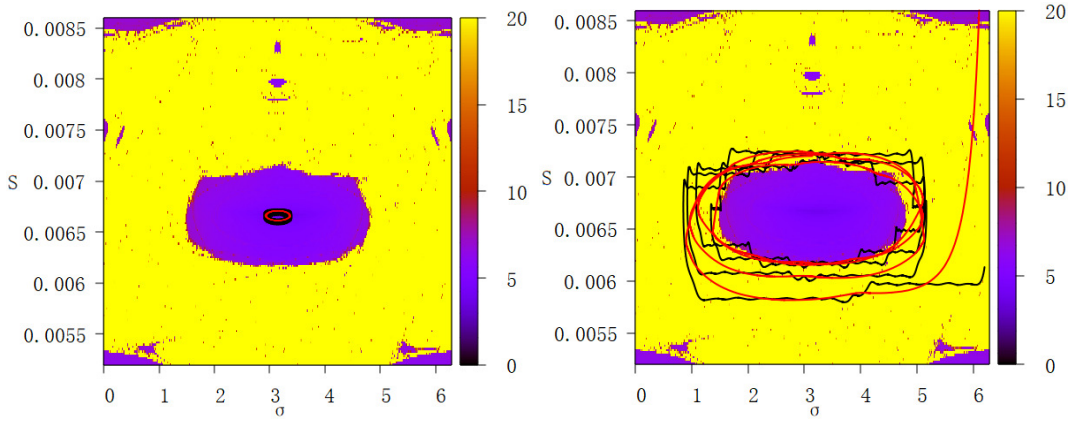

Figure 3.21: Dynamics in the 5:6 MMR resonance with Neptune for $N = -1.0227631265461785$, namely, the critical case (see also Fig. 3.22). Two panels illustrate the projection of averaged (red lines) and non averaged (black lines) orbits on the resonant phase-plane σ-S, with the values of the regularized FLI represented on the background. Left panel refers to a resonant libration and the right panel shows a chaotic orbit which initially is phase-protected from close encounters.

3.3.3 Technical details

We provide below some technical details about the numerical computations of this Chapter.

- The phase-portraits of the averaged Hamiltonian are obtained from numerical computations of the integral[4]:

$$\widehat{\mathcal{H}}_1^{Res}(S,N,\sigma) = \frac{1}{2\pi}\int_0^{2\pi}\left(-\frac{1}{\sqrt{r^2+1-2r\cos\psi}} + r\cos\psi\right)d\nu \qquad (3.34)$$

  which may be represented is closed form. Indeed, using the formulas (3.24), (3.25), (3.26), (3.27) and Kepler's equation the integrand is first represented as an explicit function of N, S, E, σ, where E is the eccentric anomaly. Next, from the relation obtained from Kepler's equation:

$$(\zeta-\delta)\sigma + p(\nu+\theta) = E - e\sin E$$

  we change the integration variable from ν to E. The level curves of $\widehat{\mathcal{H}}^{Res}(S,N,\sigma)$ in the plane of the resonant variables $x = \sqrt{2S}\cos\sigma, y = \sqrt{2S}\sin\sigma$

[4]Please notice that this is the same definition as Eq. (3.3), since the integration in $d\nu$ provides the same results as the integration in $d(\nu+\theta)$

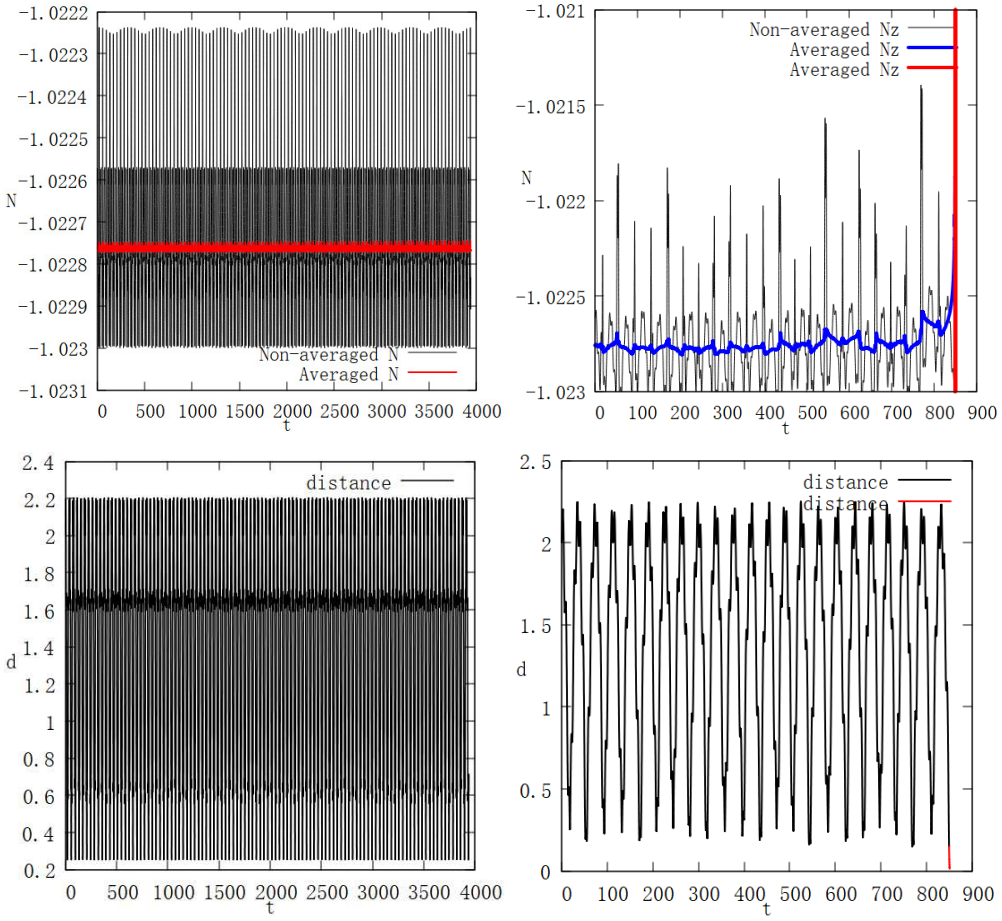

Figure 3.22: Dynamics in the 5:6 MMR resonance with Neptune for $N = -1.0227631265461785$, namely, the critical case. All the panels in the left column refer to the resonant libration of Fig. 3.21, in the right column to a chaotic orbit (right panel of Fig. 3.21) which initially is phase-protected from close encounters. Bottom panels: time evolution of the non averaged (black line) and averaged (red line) values of N. Bottom panels: time evolution of the distance $|P - P_1|$.

are then obtained from the computation of $\widehat{\mathcal{H}}^{Res}(S, N, \sigma)$ on a large grid of points of the plane x, y using the subroutine PGCONT provided by the PGPLOT library.

- With given values of a, e, d, the value of $f_*^i(a, e, d)$ can be computed from

equation 3.9a with $r = \frac{a(1-e^2)}{1+e\cos f}$:

$$f_*^i(a,e,d) = \pm \arccos\left(\frac{r_1 + d - a(1-e^2)}{e(r_1+d)}\right), \tag{3.35}$$

from which one can the values of $M_*^i(a,e,d)$. Or equivalently, one can obtain $M_*^i(a,e,d)$ from the eccentric anomaly $E_*^i(a,e,d)$ with $r = a(1-e\cos E)$:

$$E_*^i(a,e,d) = \pm \arccos\left(\frac{a-(r_1+d)}{ae}\right), \tag{3.36}$$

then according to Kepler's Equation

$$M_*^i(a,e,d) = E_*^i - e\sin E_*^i. \tag{3.37}$$

- The orbits of the CR3BP are numerically computed using the Levi-Civita regularization at the secondary body P_1. The numerical integrator is an explicit Runge-Kutta method of order 6.

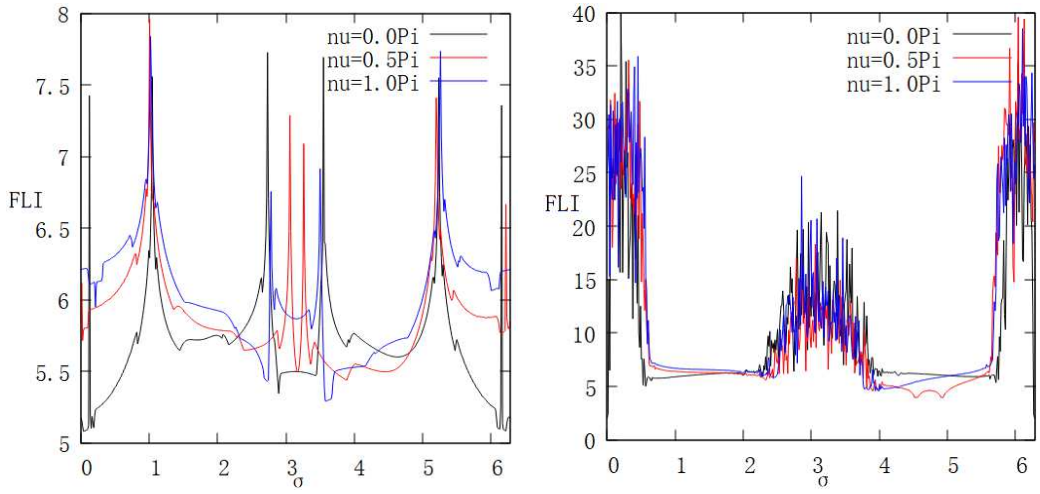

Figure 3.23: Values of the regularized FLI for the 1:2 MMR with Jupiter for $N = -1.24$ and $T = 800$ (left panel) and for $N = -1.10$ and $T = 800$ (right panel). The other initial conditions are: $\sigma \in [0, 2\pi]$, $\theta = 0$ and $\nu = 0, \pi/2, \pi$ (black, red and blue lines respectively), while S solves $\partial\widehat{\mathcal{H}}_0/\partial S = 0$.

- The regularized Fast Lyapunov Indicators (defined as in [CelSLF11, GuzL13], see also [GuzL23] and references therein) are computed from the variational equations of the CR3BP written using the Levi-Civita regularization at the secondary body P_1, depending on the value of N, on refined grid of initial

conditions in the x, y or the σ, S planes (see Chapter 2). The other initial conditions $N, \nu + \theta$ are the same for all the points of the grid. The action N is the most relevant parameter for the distribution of the values of the FLI, while the angle $\nu + \theta$ is a fast phase which is arbitrarily fixed. The computation of the phase-portraits of the averaged Hamiltonians do not depend on the value of $\nu + \theta$, while the computations of the FLI depend on it and therefore provide a section of the real dynamics for the specific value of the fast phase. The initial conditions of the FLI computations of the Figs. 3.7, 3.9, 3.11, and 3.14, 3.15, 3.16, 3.17, 3.18 are computed for $\nu = \pi$ and $\theta = 0$ (which means that P is at the apocenter and $\sigma = \varphi$), while for comparison with other values of ν Fig. 3.21 is computed for $\nu, \theta = 0$ and Fig. 3.23 compares the values of the FLI for $\nu = 0, \pi/2, \pi$. In particular, in Fig. 3.23 we appreciate the correspondence of most of the structures revealed by the FLI, with a phase displacement of the position of the peaks corresponding to the separatrices of the equilibria of the resonant normal form.

- The Fast Fourier Transform has been computed using the algorithm described in Numerical Recipes in Fortran.

3.4 Conclusions

In this Chapter, we show that using a numerical method it is possible to construct effective canonical transformations for the MMR of the planar circular restricted three-body problem also for the large values of eccentricity for which the orbits of P cross the orbit of the secondary body P_1. After a detailed analysis of the analytic issues which are raised by the definition of these transformations, the efficacy of the averaging method is confirmed also for the orbits which cross the orbit of the secondary body, except when the orbits enter a neighborhood of the set where the Fourier transform of the perturbation with respect to the fast angle of the resonance is singular. Quite unexpectedly, the averaging method proved to be effective also when large parts of the resonant phase-plane were affected by chaotic diffusion, as it has been revealed by the computation of the regularized FLI. A possible reason is that chaos due to close encounters is localized in time and space, so during the relatively long time intervals where the orbits do not experience close encounters, the averaging method is effective, and chaos will show up only in the future. In these regimes, already one step of perturbation theory is sufficient to reveal the properties of these chaotic diffusions which occur with small random almost-stepwise variations of the quasi-integrals of motion N and of the averaged Hamiltonian similarly to the Arnold diffusion detected in [GuzEP20]. Chaotic

diffusion in particular is effective in removing phase-protection mechanisms, leading to possible deep close encounters. Within deep close encounters, as expected, this resonant averaging is not effective, and other perturbation methods could be employed (such as the perturbation theory developed in [Guzzo24]) and used to complement the previous analysis.

Chapter 4

Explorations of chaotic diffusions triggered by multiple close encounters in a MMR: the spatial case

In this Chapter we consider the spatial circular restricted three-body problem and we study the individual and cumulative effects of close encounters in an external MMR. In this case we have a four degrees of freedom system in the extended phase space, and after averaging the fast angles the averaged Hamiltonian has two degrees of freedom. Indeed, the MMR normal form Hamiltonian in the SCRTBP is composed of three systems of different time scales: the shorter one is of order $\mathcal{O}(1)$ and characterizes the close encounters of P with P_1, and the other ones are of order $\mathcal{O}(1/\sqrt{\varepsilon})$ characterizing the resonant motions and $\mathcal{O}(1/\varepsilon)$ for the secular evolution. If the value of ε is small, the slower variables change slowly and can be regarded as fixed in first approximation. In successive approximations, the couplings between slow and fast variables are studied, to investigate the emergence of chaos and diffusion. We first analyze the collision and the singular sets of the spatial CRTBP expressed using the action-angle variables defined for a given MMR. On the resonant planes we identify an indicator, called Minimum Resonant Distance (MRD) which in the SCRTBP is the relevant parameter to determine the effect of a close encounter. Afterward, using a combined analysis that leverages the computation of the approximate first integrals, of Fast Lyapunov Indicators, of the singular sets, and of adiabatic theory, we provide examples of chaotic diffusion which, in addition to the crossings of a separatrix, are due to the accumulation of effects of weak close encounters. In particular, we will provide examples of how a deep close encounter may determine the extraction from a main resonance, such as the 1:2 mean motion resonance with Neptune, and the subsequent cascade of close encounters determines a slower chaotic diffusion between the nearby resonances.

This Chapter is structured as follows. In Section 4.1 we recall the definition of the MMR resonant normal form, the averaging transformation, the semi-secular and the secular phase planes, and we provide the definition of singular sets and lines of small MRD in the semi-secular plane. In Section 4.2 we provide examples of regular and chaotic motions: we distinguish the case of N much smaller than the critical value N_c (for which collisions are not possible within the MMR); N close to N_c; N much larger than N_c, and we highlight the role of sequences of close encounters for producing chaotic diffusion. All the examples are provided for the sample external 1:2 MMR. Conclusion are provided in Section 4.4. In the Appendix we provide some details about the adiabatic invariants and the definition of Fast Lyapunov Indicators.

4.1 The averaged Hamiltonian, the singular set and the line of MRD

To represent the averaged Hamiltonian we first recall the resonant action-angle variables introduced in Eq. (2.22) for a $p : q$ external MMR of order $q-p = 1$ (see for examples [Mor02, MilB98]):

$$\begin{pmatrix} \sigma \\ \alpha \\ \nu \\ \theta \end{pmatrix} = \begin{pmatrix} q & q-p & 0 & -p \\ 0 & 1 & -1 & 0 \\ -1 & 0 & 0 & 0 \\ 0 & 0 & 0 & 1 \end{pmatrix} \begin{pmatrix} \lambda \\ \varphi \\ \gamma \\ \lambda_1 \end{pmatrix}, \tag{4.1a}$$

$$\begin{pmatrix} S \\ A \\ N \\ \Theta \end{pmatrix} = \begin{pmatrix} 0 & 1 & 1 & 0 \\ 0 & 0 & p-q & 0 \\ p-q & q & q & 0 \\ 0 & p & p & 1 \end{pmatrix} \begin{pmatrix} \Lambda \\ \Phi \\ \Gamma \\ \Lambda_1 \end{pmatrix}, \tag{4.1b}$$

where in particular $\theta = \lambda_1$ and $\nu = -\lambda$ are fast angles, $\sigma = q\lambda - p\lambda_1 - (q-p)(\Omega+\omega)$ is the critical angle of the resonance, and $\alpha = -\omega$ is a secular angle. With these variables, the Hamiltonian of the spatial circular restricted three-body problem is represented as the sum of the integrable part:

$$\widehat{\mathcal{H}}_0 = -\frac{1}{2(qS-N)^2} + n_1(-pS+\Theta), \tag{4.2}$$

and of the perturbing function $\varepsilon\widehat{\mathcal{H}}_1$ dependent on $S, A, N, \sigma, \alpha, \nu+\theta$, which is expressed by the Fourier expansion:

$$\begin{aligned}\widehat{\mathcal{H}}_1 =& c_0(S,A,N,\sigma,\alpha) + \sum_{k=1}^{\infty} c_k(S,A,N,\sigma,\alpha)\cos(k(\nu+\theta)) \\ &+ \sum_{k=1}^{\infty} s_k(S,A,N,\sigma,\alpha)\sin(k(\nu+\theta))\end{aligned} \tag{4.3}$$

with

$$c_0 := \frac{1}{2\pi}\int_0^{2\pi} \widehat{\mathcal{H}}_1(S,A,N,\sigma,\alpha,\nu+\theta)\mathrm{d}(\nu+\theta) \tag{4.4}$$

and, for $k \geq 1$:

$$c_k := \frac{1}{\pi}\int_0^{2\pi} \widehat{\mathcal{H}}_1(S,A,N,\sigma,\alpha,\nu+\theta)\cos[k(\nu+\theta)]\mathrm{d}(\nu+\theta) \tag{4.5}$$

$$s_k := \frac{1}{\pi}\int_0^{2\pi} \widehat{\mathcal{H}}_1(S,A,N,\sigma,\alpha,\nu+\theta)\sin[k(\nu+\theta)]\mathrm{d}(\nu+\theta). \tag{4.6}$$

From (4.2) and (4.3) one defines the averaged Hamiltonian of the SCRTBP:

$$\widehat{\mathcal{H}}^{Ave} = \widehat{\mathcal{H}}_0(S,N,\Theta) + \varepsilon c_0(S,A,N,\sigma,\alpha) \tag{4.7}$$

whose dynamics is related to the dynamics of the three-body problem only in a domain of the variables $(S, A, N, \Theta, \sigma, \alpha, \nu, \theta)$ where a close-to-the-identity canonical transformation $\mathcal{C}_\chi$ (hereafter called averaging transformation) conjugates the original Hamiltonian to the resonant normal form:

$$\widehat{\mathcal{H}}^{Res} := \widehat{\mathcal{H}}^{Ave}(S,A,N,\sigma,\alpha) + \varepsilon^2\widehat{R}(S,A,N,\sigma,\alpha,\nu+\theta), \tag{4.8}$$

where the dependence on the fast angle $\nu+\theta$ is relegated to the remainder $\varepsilon^2\widehat{R}$.

Note that, for the averaged Hamiltonian, the actions N and Θ are constants of motion, of which Θ is related to the auxiliary variable Λ_1 and N is a function of the semi-major axis, the eccentricity and the inclination. For the averaged Hamiltonian we will ignore Θ and retain the first integral N. The averaged system will be parameterized by N:

$$N = \sqrt{a}\left[p - q\sqrt{1-e^2}\cos(i)\right]. \tag{4.9}$$

Remark. The level sets of N have been already described in Chapter 2. In the following section we only consider the 1:2 resonance, and its level curves will be discussed again. Since the dynamics is inside MMRs i.e. the semi-major axis a is assumed to be close to the resonant value, fixed values of N would lead to a restriction of the eccentricity and inclination.

4.1.1 Definition of the averaging transformation

The definition of the averaging transformation in the spatial problem is similar to that already discussed for the planar case. In fact, the averaging transformation $\mathcal{C}_\chi$ is defined and computed using the Lie method as the time-ε Hamiltonian flow of a generating function:

$$\chi = \sum_{k\geq 1} \left[b_k \sin(k(\nu+\theta)) + d_k \cos(k(\nu+\theta)) \right], \tag{4.10}$$

whose coefficients $b_k(N, S, A, \sigma, \alpha)$ and $d_k(N, S, A, \sigma, \alpha)$ are given by

$$b_k = \frac{c_k}{k\left(\frac{\partial \widehat{\mathcal{H}}_0}{\partial N} + \frac{\partial \widehat{\mathcal{H}}_0}{\partial \Theta}\right)}, d_k = -\frac{s_k}{k\left(\frac{\partial \widehat{\mathcal{H}}_0}{\partial N} + \frac{\partial \widehat{\mathcal{H}}_0}{\partial \Theta}\right)}. \tag{4.11}$$

The similarities with the planar case arise from the Fourier series expansion of the perturbing function, conducted exclusively in the angle $\nu+\theta$, and in the numerical method which is used to compute the Fourier coefficients. In fact, the canonical transformation is effectively computed with the Lie method by numerically computing the Fourier coefficients c_k, s_k of the perturbing function (see Eq. (4.3)) as well as their derivatives, using the method of Schubart [Schu64, Schu66] by extending to the spatial case the implementation of the planar case (see Chapter. 3 and [LiuGuzzo25]). The numerical computation of $\mathcal{C}_\chi$ will be used to compare the time evolution of the non-averaged variables with the time evolution of the averaged ones (the transformation from non-averaged ones to the averaged ones has been given for the PCRTBP, and can be immediately extended to the SCRTBP, see Eq. (3.33)).

In the domain of the phase-space where $\widehat{\mathcal{H}}_0 + \varepsilon\widehat{\mathcal{H}}_1$ is conjugate to $\widehat{\mathcal{H}}^{Res}$, the dynamics in the MMR is approximated with the dynamics of the averaged Hamiltonian $\widehat{\mathcal{H}}^{Ave}$ which is obtained from the resonant form (4.8) by neglecting the remainder $\varepsilon^2\widehat{R}$. The analysis of the dynamics of the averaged Hamiltonian has been done in the literature by noticing that N, Θ are first integrals for the Hamiltonian flow of $\widehat{\mathcal{H}}^{Ave}$, and therefore one proceeds by studying the dynamics in the reduced phase-space of the variables S, A, σ, α. Moreover, the conjugate variables A, α have slow variation, since their time derivatives (obtained from the Hamilton

equations of $\widehat{\mathcal{H}}^{Ave}$) are proportional to ε, while the conjugate variables S, σ have faster variation in the domain of the MMR (typically they evolve on timescale of order $1/\sqrt{\varepsilon}$). Therefore, the phase-portraits of $\widehat{\mathcal{H}}^{Ave}$ obtained for fixed N, A, α provide a first approximation of the dynamics which is valid for a time interval much smaller than $1/\varepsilon$. For longer times the theory of adiabatic invariants ([Wis83, Nei87, NeiSido04, Sido06, SidoNAZ14, MilB98, EfimS20, Sido24, FerS89, Mor02, NesTFM02, Sail16, Gal20, FenGS22, Pan25]) has been used to study the secular evolution of the variables A, α, predicting the existence of regular as well as of chaotic motions.

For $N > N_c$ (actually, also for $N \leq N_c$ whenever $N \simeq N_c$) the possibility of close encounters adds an additional source of instability since the conservation of the averaged Hamiltonian may be broken, thus enlarging the possibility of generating complex orbits and chaotic diffusion. Therefore, when analyzing the resonant dynamics characterized by multiple close encounters, a crucial question is related to identifying the domain where the conjugation of $\widehat{\mathcal{H}}_0 + \varepsilon\widehat{\mathcal{H}}_1$ to its normal form Hamiltonian $\widehat{\mathcal{H}}^{Res}$ is not defined due to the singularities of the perturbing function.

Two prerequisites for the existence of the averaging transformation $\mathcal{C}_\chi$ are: the regularity of the Fourier expansion (4.3); $\varepsilon\widehat{\mathcal{H}}_1$ is indeed a perturbation of $\widehat{\mathcal{H}}_0$. Both these requirements are not satisfied in a specific domain of the reduced phase-space variables S, A, N, σ, α due to the gravitational singularities of the perturbation. In fact, the integrands appearing in Eqs. (4.4,4.5,4.6) are singular when they are computed on $S, A, N, \sigma, \alpha, \nu, \theta$ in the collision set:

$$\mathcal{C} = \{\xi = (S, A, N, \sigma, \alpha, \nu, \theta) : \mathbf{r}_{|\xi} = (\cos\theta, \sin\theta, 0)\},$$

which contains the states of P with radius vector corresponding to a collision of P with P_1 ($\mathbf{r}$ denotes the radius vector $P - P_0$ represented by ξ). As a consequence, the Fourier coefficients c_k, s_k (or their derivatives) are not defined on the set of the reduced phase-space variables:

$$\mathcal{S} = \{(S, A, N, \sigma, \alpha) : \exists\ \nu, \theta \text{ with } (S, A, N, \sigma, \alpha, \nu, \theta) \in \mathcal{C}\},$$

which is the singular set for the spatial CRTBP.

4.1.2 Characterization of the collision and singular sets

In this Section we characterize the collision set $\mathcal{C}$ and the singular set $\mathcal{S}$ in the space of the resonant action-angle variables $(S, A, N, \sigma, \alpha, \nu, \theta)$ of the spatial CRTBP.

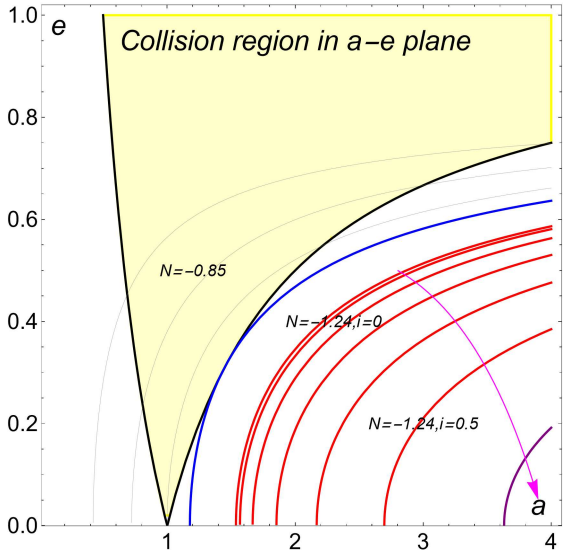

Figure 4.1: Level curves of N defined in Eq. (4.9) for the 1:2 MMR, for different values of the inclination i. The yellow region represents the solutions to Eq. (4.16). The blue and gray curves are level curves of N for $i = 0$. All the red curves are level curves of $N = -1.24$ with the inclination increasing from $i = 0$ to $i = 34.4°$ (the pink curve denotes the direction in which the inclination increases). For a fixed value of N, the level curves move far away from the collision region as the value of inclination increases. For the 1:2 MMR we have the critical value is $N_c \simeq -1.08524$.

This discussion is here presented for the external $p : q$ MMRs of order 1, i.e. $q = p + 1$.

We first consider the collision set, containing all the states of P determined by the values of $S, N, A, \sigma, \alpha, \nu, \theta$ for which the corresponding radius vector $\mathbf{r} = P - P_0$ satisfies:

$$\mathbf{r} = (\cos\theta, \sin\theta, 0). \tag{4.12}$$

Since Eq. (4.12) is easily represented explicitly using the orbital elements a, e, i, f, ω, Ω, we first represent the values of the actions:

$$S = \sqrt{a}\left[1 - \sqrt{1-e^2}\cos(i)\right], \tag{4.13}$$

$$A = (p-q)\sqrt{a}\sqrt{1-e^2}\left[1 - \cos(i)\right], \tag{4.14}$$

$$N = \sqrt{a}\left[p - q\sqrt{1-e^2}\cos(i)\right], \tag{4.15}$$

which identify the values of a, e, i. For simplicity, we only consider values of the

actions corresponding to $a > 1$ (external resonances), $e \in (0, 1)$ (eccentric orbits) and $i \in (0, \pi/2)$ (inclined prograde orbits).

For the given resonance, there exists a critical value N_c which is negative and such that for $N < N_c$ the singular and the collision sets are empty (see Fig. 4.1). Then we consider $N \in (N_c, 0)$. A necessary condition for $(S, A, N, \sigma, \alpha) \in \mathcal{S}$ is that S, A, N, α identify a Keplerian ellipse with orbital parameters a, e, i, ω that ensure the intersection of the ellipse with the orbit of P_1 (the case of tangent orbits is not considered for simplicity). Therefore, S, A, N must determine values of a, e, i with

$$a(1 - e) < 1 < a(1 + e). \tag{4.16}$$

For $a > 1$ (since we are considering the external resonance), and considering for simplicity the strict inequality, Eq. (4.16) becomes:

$$a(1 - e) < 1. \tag{4.17}$$

For any given value of $N \in (N_c, 0)$, condition (4.17) is satisfied if (A, S) belongs to a two-dimensional subset of $\mathbb{R}^2$. In fact, after some algebraic manipulations of Eq.s (4.13,4.14,4.15) condition $a(1-e) < 1$ is satisfied by the solutions A, S of the system:

$$\begin{aligned} &A < 0, \quad qS - N > 0, \quad \frac{S + A}{qS - N} < 1 \\ &a = (qS - N)^2, \quad e = \sqrt{1 - \left(1 - \frac{S + A}{qS - N}\right)^2} \\ &a(1 - e) < 1 \end{aligned}$$

After the actions S, A, N have been chosen such that a, e, i satisfy condition (4.17) with $i \in (0, \pi/2)$, we have to characterize the values of the angles which indeed, for these values of a, e, i, provide a solution to Eq. (4.12). Since the inclined orbits of P may cross the orbit of P_1 only at the nodes, we have a solution to Eq. (4.12) corresponding to a collision at the ascending node if $f, \omega, \Omega, \theta$ satisfy the system:

$$\frac{a(1 - e^2)}{1 + e\cos(f)} = 1, \tag{4.19a}$$

$$\omega + f = 0, \tag{4.19b}$$

$$\theta - \Omega = 0, \tag{4.19c}$$

and a similar system for the collision at the descending node. Eq. (4.19a) has two solutions $f = f_*^i(S, A, N), i = 1, 2$, which correspond to two values for the mean

anomaly $M = M_*^i(S, A, N)$. Therefore, $f, \omega, \Omega, \theta$ solve the Eq.s (4.19a,4.19b,4.19c) providing a collision at the ascending node (a similar system holds for the descending node) if:

$$\begin{aligned} f &= f_*^i(S, A, N), \\ \omega &= -f_*^i(S, A, N), \\ \Omega &= \theta. \end{aligned} \tag{4.20}$$

By inverting the transformation (4.1a) and performing few algebraic simplifications, the solutions (4.20) are mapped to

$$\begin{pmatrix} \sigma \\ \alpha \\ \nu + \theta \end{pmatrix} = \begin{pmatrix} q & p & -p \\ 0 & -1 & 0 \\ -1 & -1 & 1 \end{pmatrix} \begin{pmatrix} M_*^i(S, A, N) \\ -f_*^i(S, A, N) \\ 0 \end{pmatrix}. \tag{4.21}$$

Therefore, when S, A, N determine a, e, i satisfying (4.16) with $i \in (0, \pi/2)$, there exists a discrete set of functions $\hat{\alpha}(S, A, N), \hat{\sigma}(S, A, N), \hat{\nu}(S, A, N)$ such that S, A, N, σ, α with:

$$\begin{aligned} \sigma &= \hat{\sigma}(S, A, N), \\ \alpha &= \hat{\alpha}(S, A, N), \end{aligned} \tag{4.22}$$

is in the singular set, and if moreover:

$$\nu + \theta = \hat{\nu}(S, A, N),$$

$(S, A, N, \sigma, \alpha, \nu, \theta)$ is in the collision set.

From the parameterizations (4.22), we obtain that the intersection of the singular set with the four-dimensional reduced phase-space of variables (S, A, σ, α) for given values of $N > N_c$ is a two-dimensional set. Moreover, for fixed values of the slow variables (A, α), the intersection of the singular sets $\mathcal{S}$ with the plane of the resonant variables (S, σ), when non-empty, typically consists of isolated points. These points will be called *singular points*. This property establishes a significant distinction of the collision set of the spatial problem and that of the planar one, where the singular set typically forms a curve in the space of resonant variables (S, σ).

In Fig. 4.2 we provide graphical representation of the projection of the singular set on the three-dimensional spaces S, A, σ and S, A, α, for $N = -0.85 > N_c$ (left column). We also represent in the two-dimensional planes S, σ and S, α the curves obtained by fixing the value of A (right column), distinguishing between the intersections occurring at the ascending or descending node and the solutions identified by the two different indices $i = 1, 2$ in Eq. (4.21) (a similar representation holds for the descending node).

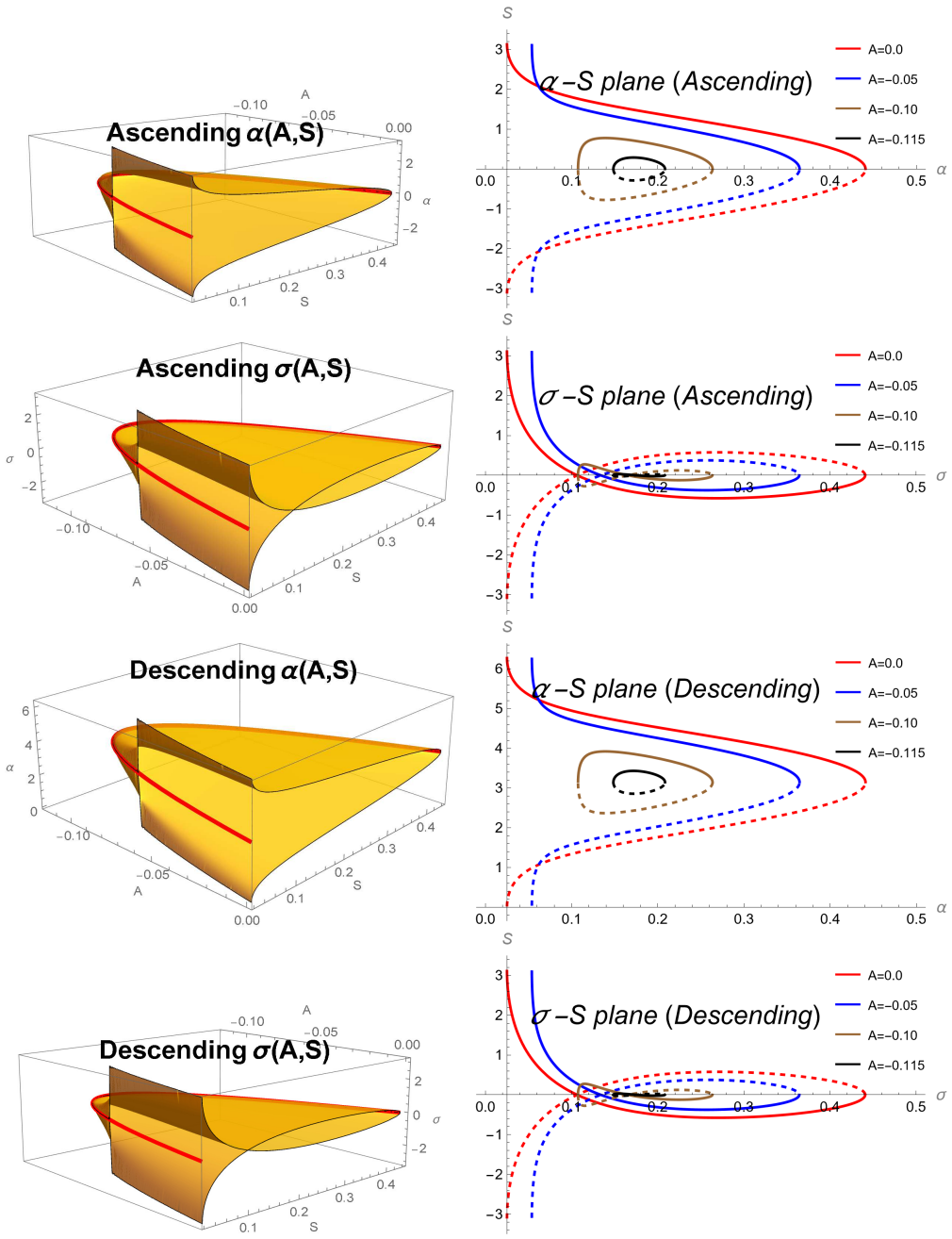

Figure 4.2: Projections of the two branches of the singular sets defined by the intersection at the ascending and descending nodes on three and two dimensional subset of variables, for $N = -0.85$. Left panels: three-dimensional illustration of $\sigma = \sigma(S, A, N), \alpha = \alpha(S, A, N)$, respectively. Right panels: representation of the singular sets in (S, σ) and (S, α) planes for different values of A. The continuous and dashed curves refer to the value of the index $i = 1, 2$ identifying the two solutions (4.21) for the ascending node; same notation for the descending node.

From the panels, we can observe the intricate changes in the points of the singular set, as the values of certain variables changes. The complex patterns of these changes reveal the multifaceted nature of the singular set's structure. For example, let us consider the intersections of the singular set with the plane (S, σ) for fixed values of (A, N, α), with $N = -0.85, A = -0.05$: in the top-right panel the blue curve identifies the values of (S, α) for which $\alpha = \hat{\alpha}(S, A, N)$ (obtained for the ascending node). Therefore, if we fix the value of α, we have one value of $S = S_*$ provided by the solution with $i = 1$ or $i = 2$. If we consider the curve $\sigma = \hat{\sigma}(S, A, N)$ (defined by the same value of i) depicted in the second right-panel from the top for the same value of A, for $S = S_*$ we have one value of σ for which $(S, A, N, \sigma, \alpha)$ is in the singular set. Another point may be found by repeating the procedure for the descending node.

4.1.3 The perturbing function and the singular set

The perturbing function $\varepsilon\widehat{\mathcal{H}}_1$ is not a perturbation of $\widehat{\mathcal{H}}_0$ in a neighbourhood of the collision set defined by small values of the function:

$$\|P - P_1\|(S, A, N, \sigma, \alpha, \nu + \theta).$$

Moreover, the Fourier representation of the $\widehat{\mathcal{H}}_1$ is singular at all $(S, A, N, \sigma, \alpha)$ in the singular set, and correspondingly any truncated Fourier series:

$$\langle\widehat{\mathcal{H}}_1\rangle := c_0 + \sum_{k=1}^{K} c_k \cos(k(\nu + \theta)) + \sum_{k=1}^{K} s_k \sin(k(\nu + \theta)), \tag{4.23}$$

with large truncation order K, fails to represent the perturbing function in a neighbourhood of the singular set defined by small values of:

$$\mathrm{MRD}(S, A, N, \sigma, \alpha) = \min_{\nu+\theta\in[0,2\pi]} \|P - P_1\|(S, A, N, \sigma, \alpha, \nu + \theta), \tag{4.24}$$

which we call Minimum Resonant Distance (MRD) for a point $(S, A, N, \sigma, \alpha)$. With evidence, $\mathrm{MRD}(S, A, N, \sigma, \alpha) = 0$ if $(S, A, N, \sigma, \alpha) \in \mathcal{S}$. Please note that the MRD may be positive for some values of its argument also when the orbit of P intersects the orbit of P_1, i.e. when the Minimum Orbital Intersection Distance (MOID) is equal to zero.

Although in the plane of the resonant variables (σ, S), for fixed values of N, A, α, we typically have a few isolated singular points, their neighborhoods defined by small values of the MRD can extend in the phase-portrait significantly beyond these isolated points.

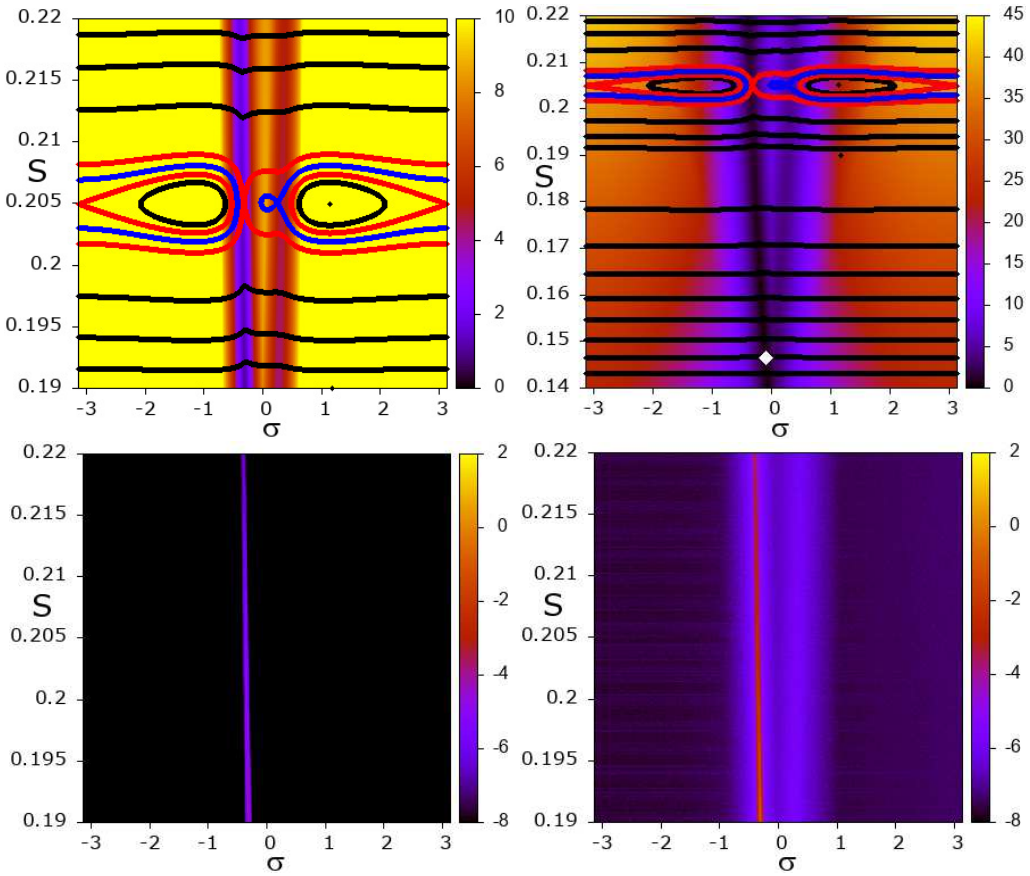

Figure 4.3: Top panels: level curves of the averaged Hamiltonian represented on the (σ, S) plane for the Sun-Neptune case mass ratio, and computed for $N = -0.85, A = -0.05, \alpha = 1.3319$ for different ranges of S. The level curves have been obtained by computing numerically the integral (4.27) on a 2-dimensional grid of values, and using the library PGPLOT. The ratio between the MRD and r_N is also represented on the background of the panels using two different color scales. The white square in the top-right panel indicates a singular point. Bottom panels: verification of the correctness of the Fourier representation (4.23) of the disturbing function for $K = 2^9$. The panels represent with a color scale the value of $\log_{10} \mathcal{E}$ computed with $\mathcal{U} = \widehat{\mathcal{H}}_1$ (bottom-left panel) and $\mathcal{U} = \frac{\partial \widehat{\mathcal{H}}_1}{\partial S}$ (bottom-right panel) for N, A, α as in the top panels, and σ, S in a two dimensional grid of values. For each value of σ, S in the grid, the coefficients c_k, s_k in (4.23) are obtained from a Fast Fourier Transform of the values of $\widehat{\mathcal{H}}_1$ computed on a regular grid of values of $\nu + \theta$, and afterwards their derivatives with respect to an action variable are obtained numerically using a difference method.

Let us discuss this property with reference to a specific case, depicted in Fig. 4.3, where on the top-panels we represent the level curves of the averaged Hamiltonian on the plane (σ, S) for a fixed value of N, A, α (the pictures are obtained for $N = -0.85, A = -0.05, \alpha = 1.3319$), and on the background for each value of σ, S we represent with a color scale the value of the MRD in units of

$$r_N = \mu_N^{1/3}, \tag{4.25}$$

where $\mu_N := \frac{\varepsilon}{1+\varepsilon}$ denotes the reduced mass of Neptune.

The left-panel is centered at the resonance, while in the right-panel we consider a larger interval of S to localize also the singular point at $S \simeq 0.1465$ and $\sigma \simeq -0.089$ (indicated with a white box in the top-right panel). We observe that from the singular point there emanates a V-shape set of points characterized by small values of the MRD: very small MRD for the left branch (between $1.4r_N$ and $1.7r_N$ in the resonance region), moderately small MRD for the right branch (between $4.5r_N$ and $5r_N$ in the resonance region). The region of smaller values of the MRD is also characterized by folds in the level curves of the averaged Hamiltonian. At this regard, we recall that folds in the phase-portrait of the resonant variables have been represented also in different MMRs (see, for example, [GroM98, NesTFM02]).

To test the correctness of the truncated Fourier representation (4.23) we compute the values of $\widehat{\mathcal{H}}_1$ (and its partial derivatives) with the values of the truncated Fourier series $\langle \widehat{\mathcal{H}}_1 \rangle$ (and its partial derivatives, respectively) defined in Eq. (4.23). In the bottom panels of Fig. 4.3 we report the results obtained for N, A, α fixed to the values considered for the top panels, while S and σ are in a regularly spaced grid of 500×500 values in the intervals $\sigma \in [0, 2\pi]$ and $S \in [0.19, 0.22]$. For each value of σ, S in the grid, we compute an indicator of the efficiency of the truncated Fourier representation of $\widehat{\mathcal{H}}_1$ and its partial derivatives defined by:

$$\mathcal{E} := \max_{\nu+\theta \in [0,2\pi]} \left| \mathcal{U}(S, A, N, \sigma, \alpha, \nu + \theta) - \langle \mathcal{U} \rangle (S, A, N, \sigma, \alpha, \nu + \theta) \right|, \tag{4.26}$$

where $\mathcal{U}$ is the disturbing function $\widehat{\mathcal{H}}_1$ or its partial derivatives and $\langle \mathcal{U} \rangle$ its truncated Fourier representation.

In the bottom-left panel of Fig. 4.3 we represent with a color scale the values of $\mathcal{E}$ defined for $\mathcal{U} = \widehat{\mathcal{H}}_1$: we clearly appreciate a very small error $\mathcal{E}$ of the Fourier representation except for the set of points in the left branch with very small MRD. On the points of the right branch with moderately small MRD the Fourier representation of perturbing function is accurate, though with a larger error of $\mathcal{E} \simeq 10^{-5}$ when considering the partial derivative $\mathcal{U} = \frac{\partial \widehat{\mathcal{H}}_1}{\partial S}$ (bottom-right panel). In fact, the partial derivatives are more singular than the perturbing function itself. We do not report the indicator computed for the partial derivatives with respect to the other variables, since the panels would be very similar to the bottom-right one.

These results suggest that the truncated Fourier representation can be used to construct the averaged transformation, except for a neighborhood of the set characterized by very small MRD values (such as the left branch in Fig. 4.3), identifying deep close encounters of P with P_1. Conversely, for moderately small values of the MRD (such as those represented in the right branch in Fig. 4.3), which identify weaker close encounters, the Fourier transform can still be used; however, the effectiveness of the averaging method needs to be tested in this case, as the values of the perturbing function and its derivatives are higher.

Remark: For the panels of Fig. 4.3 both the averaged Hamiltonian and the Fourier expansion (4.3) have been computed from numerical computations of the perturbing function using Schubart's method [Schu64, Schu66]. Precisely, the phase portraits of the averaged Hamiltonian (as in Fig. 4.3, top panels) are obtained by numerically computing the integral:

$$\widehat{\mathcal{H}}^{Ave} = \widehat{\mathcal{H}}_0 + \frac{\varepsilon}{2\pi}\int_0^{2\pi} \widehat{\mathcal{H}}_1 \mathrm{d}(\nu+\theta), \tag{4.27}$$

where the integral gives us the coefficient c_0 (see Eq. 4.4), while the coefficients c_k, s_k and their derivatives are computed using a Fast Fourier Transform of the values of $\varepsilon\widehat{\mathcal{H}}_1$ and a difference method.

4.2 Examples of resonant Lidov-Kozai dynamics and close-encounters

In this Section we provide examples of orbits in the 1:2 MMR with Neptune for values of N ranging from $N = -1.24$, i.e. below the critical value $N_c \simeq -1.08$, to $N = -0.85$ above the critical value. The aim is to show the increment of the complexity of the orbits when close encounters become possible. In particular, we will describe the dynamics of orbits which are extracted from the resonance, and due to the accumulation of the effects of a sequence of weak close encounters migrate towards nearby MMR. Our explorations consider inclined orbits, from low inclinations of few degrees up to larger inclinations of about 30 degrees.

4.2.1 Below the critical value

We consider the value of $N = -1.24$ (which is well below the critical value $N_c \simeq -1.08$) for which no close encounters of P with P_1 are possible (this value has been chosen for reference with previous studies for the planar case, see [LiuGuzzo25] for the Sun-Neptune case and [Bea94, LiuGuzzo25] for the Sun-Jupiter case).

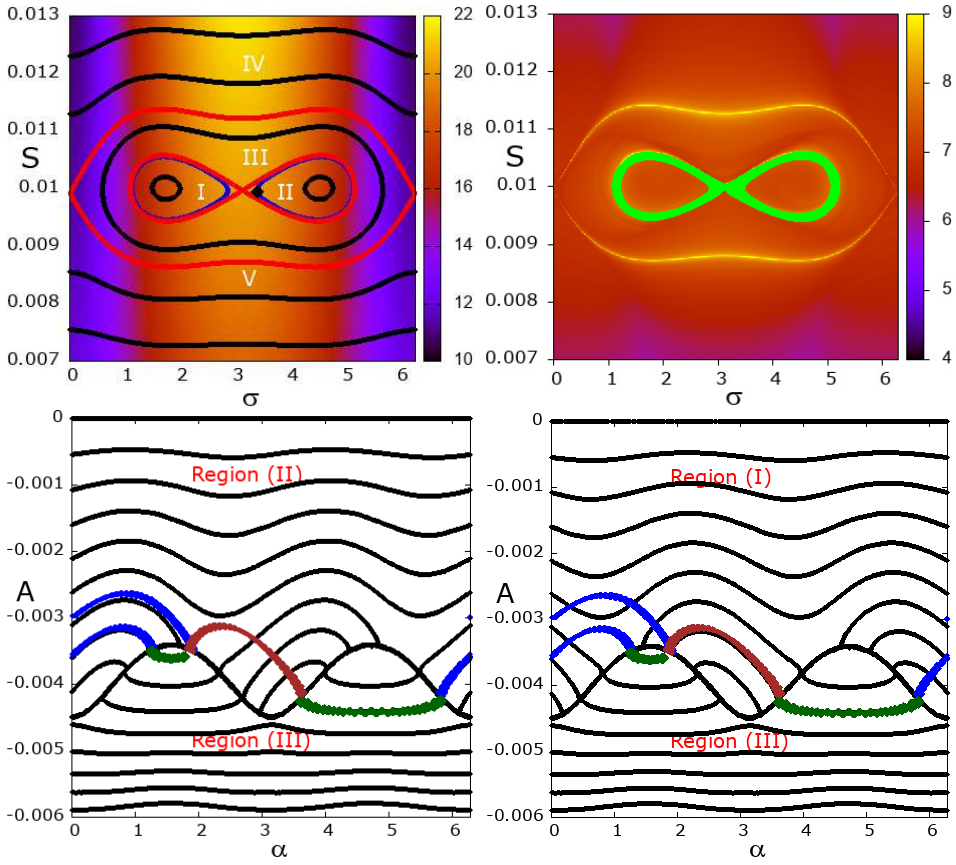

Figure 4.4: Adiabatic dynamics for $N = -1.24$, $A = -0.003$ and $\alpha = 0$. Top-left panel: level curves of the averaged Hamiltonian in the (σ, S) plane (the separatrices are represented in red) and classification of five different regions of libration and circulation labelled from I to V. The ratio between the MRD and r_N (defined in Eq. (4.25)) is represented on the background using a color scale. The black square in region II indicates the initial conditions for an orbit represented in the other panels. Top-right panel: regularized FLI in the (σ, S) plane (initial conditions for N, A, α as above, $\nu, \theta = 0$; FLI computed up to $T = 4000$ units of the regularized fictitious time, see Eq. (4.32)) represented with a color scale. The projection of the orbit (after the averaging transformation) with initial conditions for σ, S indicated by the black square in the left panel (computed up to $T = 153096$) is represented in green. Bottom panels: projection of the same orbit (after the averaging transformation) on the plane (α, A) using different colors to indicate the orbit's belonging to region I (red), II (blue) and III (green). The level curves of the adiabatic invariant defined in Eq. (4.29) by fixing the value of the averaged Hamiltonian (to the value corresponding to the fixed initial condition), for the different regions I,II,III are also represented. The bold black-curve is due to the different definition of $\mathcal{I}$ at the two sides of the separatrices. The time range represented is $t \in [0, 397712]$. At $t = 0$ the orbit is in region II at $A = -0.003$, $\alpha = 0$, and follows a level curve of $\mathcal{I}$ corresponding to region II (blue) represented in the left-panel, until it crosses the separatrix to enter region I, and following the corresponding level curve of $\mathcal{I}$ represented in the right panel (red curve). Afterwards there is another crossing of the separatrix to enter region III (green) where it follows the corresponding level curve of $\mathcal{I}$ represented in both panels, and finally it returns to region II (blue curve, close to level curves of the left panel). See also Fig. 4.5 for more information.

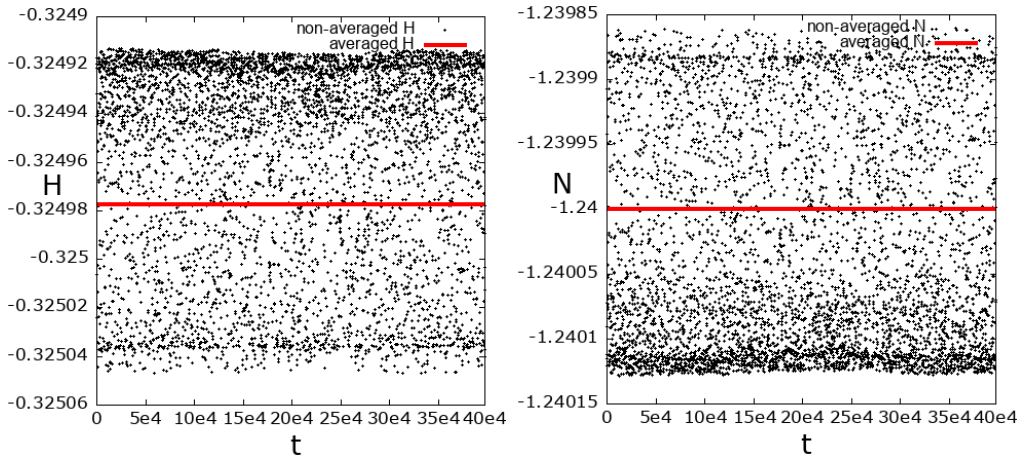

Figure 4.5: Adiabatic dynamics for $N = -1.24, A = -0.003$ and $\alpha = 0$ (see also Fig. 4.4). Left panel: conservation of $\widehat{\mathcal{H}}^{Ave}$ computed with non-averaged and averaged variables. Right panel: conservation of the action N before and after averaging.

For this value of N, the resonance is separated from nearby resonances by a region of regular motions at $i = 0$ (planar case). This remains true for low inclinations, as in the case of Fig. 4.4 and Fig. 4.5 (for $N = -1.24, S \simeq 0.01, A = -0.003$ we have $a \simeq 1.587, e \simeq 0.105, i \simeq 3.966$ deg.). The top-left panel of Fig. 4.4 represents the level curves of the averaged Hamiltonian as well as the MRD, which is larger than $10\, r_N$ (we recall that r_N is defined in Eq. (4.25)) for all the points of the panel; in the top-right panel of Fig. 4.4 we represent with a color scale the values of the FLI computed for initial conditions with N, A, α as in the top-left panel, $\nu = 0, \theta = 0$, and σ, S in a two-dimensional grid of values (the FLI is here defined and computed using the equations of motion of the spatial CRTBP written using the Kustaanheimo-Sfiefel regularization at P_1, see Section 2.4.3 for details). The distribution of the values of the regularized FLI is in agreement with the computation of the phase-portrait of the averaged Hamiltonian: the separatrices are replaced by a set, identified by the largest values of the FLI, which in the complete equations of motion of the spatial CRTBP identify chaotic motions, possibly crossing the separatrices of the averaged Hamiltonian. These chaotic motions are embedded in a region of regular motions, identified by orange color in the picture, providing the indication that the resonance is separated from the nearby MMRs. Therefore, the averaging method is effective and the averaged Hamiltonian represents accurately the resonant dynamics. The time evolution of a sample chaotic orbit with initial condition σ, S indicated by the black square in the top-left panel, is also represented (with $N, A, \alpha, \nu, \theta$ are chosen as indicated above). The projection of the orbit (after the canonical transformation) on the σ, S plane is represented

in the top-right panel by a green curve: the orbit projects to a neighborhood of the separatrix separating region I,II and III of the phase-portrait, indicating a chaotic evolution. The long-term evolution of the secular variables A, α (after the averaging transformation) is represented in the bottom panels of Fig. 4.4, and is well described by the resonant Lidov-Kozai dynamics which is obtained as an application of the theory of adiabatic invariants [Wis83, Nei87, Nei87b, NeiSido04]. According to this theory (whose main aspects are summarized in Section 4.3.2, the time evolution of the variables (α, A) follows closely the level curves of the adiabatic invariant $\mathcal{I}$ (see Eq. (4.29)) on the plane of variables (α, A), defined for a circulation or libration region, until they approach or cross a value corresponding to the boundary of the region. In the bottom panels we use different colors to indicate the orbit's belonging to region I (brown), II (blue) and III (green). The level curves of the adiabatic invariant defined in Eq. (4.29) by fixing the value of the averaged Hamiltonian (to the value corresponding to the fixed initial condition), for the different regions I,II,III are also represented. The bold black curve is due to the different definitions of $\mathcal{I}$ at the two sides of the separatrices. At $t = 0$ the orbit is in region II at $A = -0.003, \alpha = 0$, and follows a level curve of $\mathcal{I}$ corresponding to region II (blue) represented in the left-panel, until it crosses the separatrix to enter region I, and following the corresponding level curve of $\mathcal{I}$ represented in the right panel (brown curve). Afterwards there is another crossing of the separatrix to enter region III (green) where it follows the corresponding level curve of $\mathcal{I}$ represented in both panels, and finally it returns to region II (blue curve, close to level curves of the left panel). The multiple crossing of a separatrix has been identified in previous papers as a source of chaos (adiabatic chaos or geometric chaos, depending on the context). The panels of the Fig. 4.5 show the very good conservation of the averaged Hamiltonian and of the action N for the same orbit, confirming the efficacy of the averaging method.

4.2.2 Near the critical value

We consider the value of $N = -1.10$ which, although below the critical value $N_c \simeq -1.08$, is sufficiently close to it to make close encounters between P and P_1 possible. We highlight two different kinds of chaotic motions.

The first one, represented in Fig. 4.6 and 4.7, is very similar to the example shown in Section 4.2.1, with chaotic dynamics produced by the crossing of separatrices and without close encounters playing any significant role (the MRD is larger than $10\, r_N$ along the orbit, see Fig. 4.6, top-left panel). A choice of an initial condition close to the separatrix between regions I,II,III produces a chaotic orbit crossing several times the separatrix, and the secular evolution is well described by the adiabatic approximation (bottom panels of Fig. 4.6). The time evolution

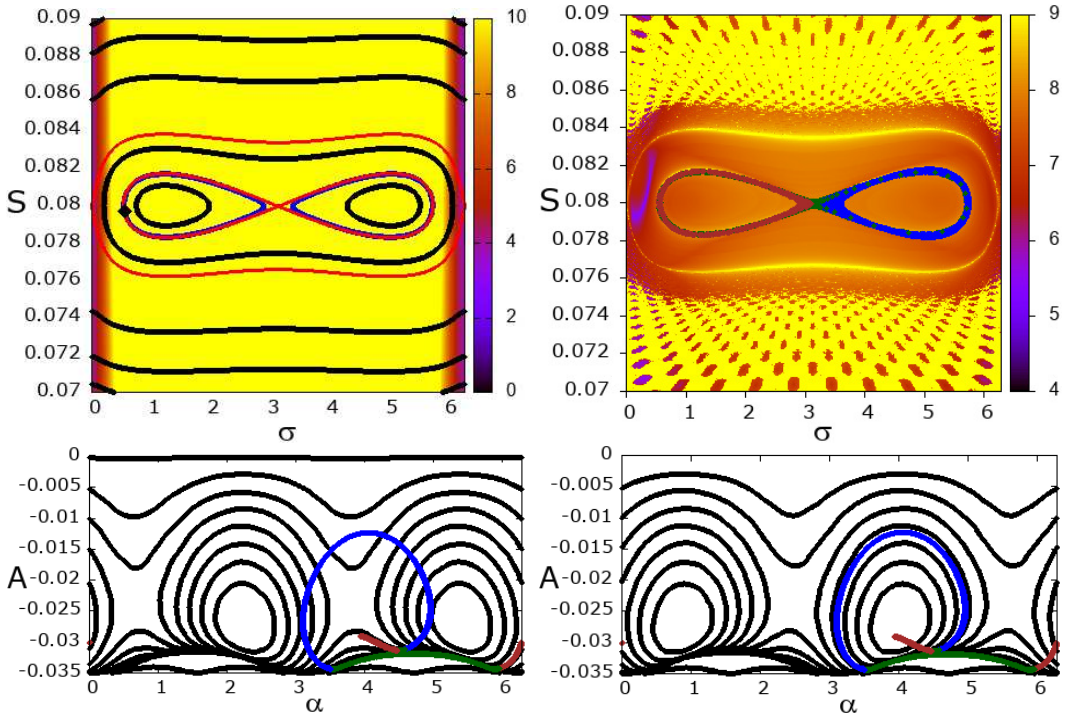

Figure 4.6: Top-left panel: level curves of the averaged Hamiltonian in the (σ, S) plane and classification of the regions of libration and circulation from I to V. The ratio between the MRD and the Neptune's Hill radius is represented on the background of the panel using a color scale (yellow means MRD$\geq$ 9). The black square in region I indicates the initial conditions for an orbit represented in the other panels. Top-right panel: regularized FLI in the (σ, S)-plane (initial conditions for N, A, α as above, $\nu, \theta = 0$; FLI computed for $T = 4000$) represented with a color scale. The projection of the orbit (after the averaging transformation) with initial conditions for σ, S indicated by the black square in the left panel (computed up to $T = 828460$) is represented in green, blue and red. Bottom panels: projection of the same orbit on the plane (α, A) using different colors to indicate the orbit's belonging to region I (red), II (blue) and (III) green. The level curves of the adiabatic invariant defined in Eq. (4.29) by fixing the value of the averaged Hamiltonian for the regions I and III (left panel) and the regions II and III (right panel) are also represented. The bold black-curve is due to the different definition of $\mathcal{I}$ at the two sides of the separatrices. The time range represented is $t \in [0, 828460]$. At $t = 0$ the orbit is in region I at $A = -0.03$, $\alpha = 2\pi$ and follows a level curve of $\mathcal{I}$ corresponding to region I (red) represented in the left-panel, until it crosses the separatrix to enter region (III), and following the corresponding level curve of $\mathcal{I}$ represented in green. Afterwards there is another crossing of the separatrix to enter region II (blue, see the right panel), and finally it returns to region I (red, see the left panel).

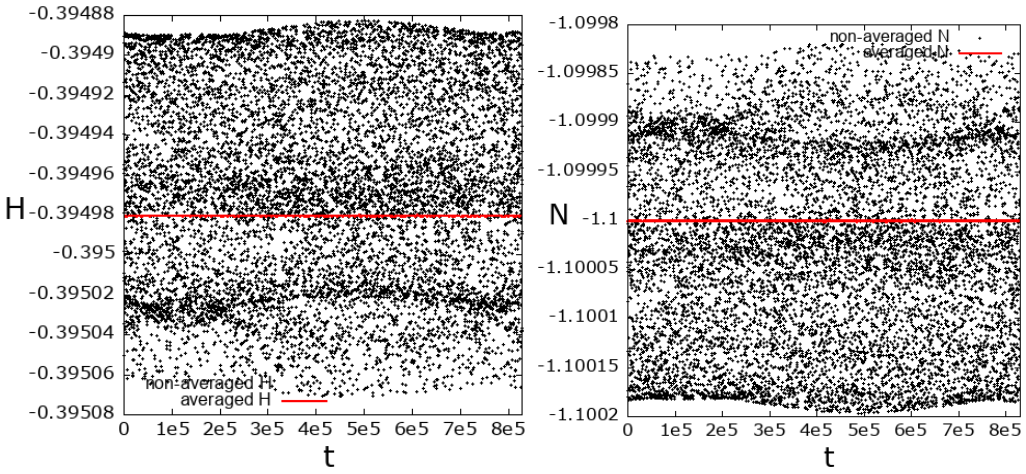

Figure 4.7: For the orbit in Fig. 4.6. Left panel: conservation of the averaged Hamiltonian before (in black) and after (red) the application of the averaging transformation. Right panel: conservation of the action N before (in black) and after (red) the application of the averaging transformation.

of the averaged Hamiltonian and of the action N (computed after the averaging transformation) show very small variations (panels in Fig. 4.7), with a very good efficacy of the averaging transformation in the reduction of the oscillations with respect to the mean value of these quantities.

In the second example, represented in Fig. 4.8, close encounters play a crucial role in shaping the chaotic dynamics: the initial condition (the black square in the top-left panel) is in the libration region III very close the the separatrix between region III and IV. Thus, at each libration, the orbit crosses a region of MRD close to $2\,r_N$ where P may have close encounters with P_1, and also may experience transitions from region III to region IV and vice versa. The FLI color map (top-right panel) shows that region IV is characterized by a large value of the FLI, indicating chaotic motions. The projection of the orbit on the FLI color map is represented in black for $t \leq 448766$, and in blue for $t \in (448766, 466610]$. In the former time interval the orbit is in region III, while in the latter the orbit performs a transition to region IV. In the bottom-left panel we represent the variation of the distance $\|P - P_1\|$ for $t \in (448766, 466610]$. The red dots sample points of the graph for which P has a close encounter with P_1 at a distance smaller than 0.15; the close encounters are with evidence clustered, due to the slow variation of the resonant variables. Up to this point, the description is similar to that given for the orbits represented in Figs. 4.4, 4.5 and 4.6,4.7. However, a significant difference emerges from the graphs representing the time variations of the averaged Hamiltonian $\widehat{\mathcal{H}}^{Ave}$ and of the actions N. In the bottom-right panel we represent the variation of the

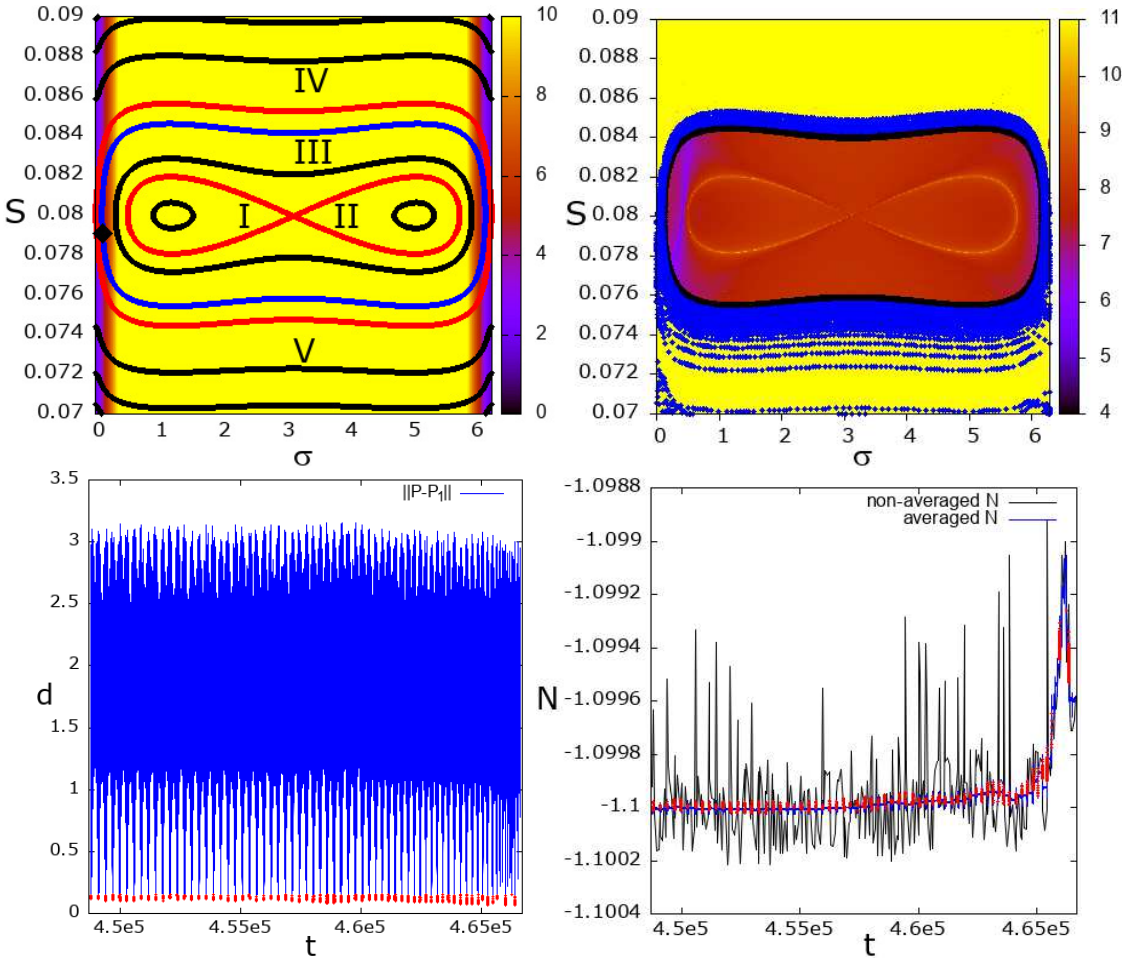

Figure 4.8: Adiabatic dynamics for $N = -1.10$, $A = -0.01$ and $\alpha = 0$. Top-left panel: level curves of the averaged Hamiltonian in the (σ, S) plane and classification of the regions of libration and circulation from I to V. The ratio between the MRD and r_N (defined in Eq. (4.25)) is represented using a color scale. The black square in region III indicates the initial conditions for an orbit represented in the other panels. Top-right panel: regularized FLI in the (σ, S)-plane represented with a color scale (initial conditions for N, A, α as above, $\nu, \theta = 0$; FLI computed for $T = 4000$, see Eq. (4.32)). The projection of the orbit (after the averaging transformation) with initial conditions for σ, S indicated by the black square in the left-panel is also represented (in black for $t \leq 448766$ and in blue for $t \in (448766, 466610]$). In the bottom-left panel we represent the variation of the distance $d = \|P - P_1\|$ for $t \in (448766, 466610]$; the red dots sample points of the graph for which P has a close encounter with P_1 at a distance smaller than 0.15. In the bottom-right panel we represent the time-variation of the action N before (in black) and after (in blue) the averaging transformation (red dots as in the bottom-left panel).

action N before (in black) and after (in blue) the averaging transformation for $t \in [448766, 466610]$: we see that while the averaging transformation is effective in reducing the local oscillations of N (compare the amplitude of the local oscillations of the black curves to the local oscillations of the blue curves), the blue curves show larger variations which are correlated with the close encounters identified by the minima of $\|P - P_1\|$ (represented in the left panel). A similar behaviour is observed for the time variation of $\widehat{\mathcal{H}}^{Ave}$ (not represented for brevity). In the time interval between each pair of close-encounter clusters the averaged values of $\widehat{\mathcal{H}}^{Ave}$ and N are almost constant, but before and after each close-encounter cluster they have a jump, which can accumulate in an apparently random way. These small random almost-stepwise variations of N and of $\widehat{\mathcal{H}}^{Ave}$ had been detected also for the planar problem (see [LiuGuzzo25]), and are similar to the Arnold diffusion detected in [GuzEP20] for a generic quasi-integrable system. In the spatial problem, the variations of N and $\widehat{\mathcal{H}}^{Ave}$ produce an additional source of chaos and diffusion with respect to the mechanism of adiabatic chaos found for the orbits of Figs. 4.4, 4.5 and 4.6, 4.7. For example, for an orbit which is initially in the circulation region of the resonance, the variation of N and $\widehat{\mathcal{H}}^{Ave}$ may determine a drift of the orbit far from the 1:2 MMR.

4.2.3 Above the critical value

We consider the value of $N = -0.85$, for which the singular set is not empty, and correspondingly we may have orbits of P crossing the orbit of P_1. The appearance of singular points in the resonant planes (σ, S) for given values of A, α has been discussed in Section 4.1.2: we refer to Fig. 4.2 for a detailed discussion and, in particular, for $N = -0.85$ the points in the singular set satisfy $-0.117 < A < 0$. We here provide more details about the properties of the level sets of the averaged Hamiltonian in the (σ, S) planes, which are determined by the appearance and the position of the singular points with respect to the resonance.

In Fig. 4.9 we provide examples for $A = -0.11$, close to its lower value for the appearance of the singular points. In this case, there are singular points in the (σ, S) plane only for specific values of α, and several model cases are represented in the panels of the figure. For $\alpha = 0$ (top-left panel) there are singular points, but they are located outside the resonance region identified by the separatrices represented in red. For $\alpha = 0.35465$ (top-right panel) there is a singular point (white square) inside the resonant region. For $\alpha = \pi/2$ (bottom-left panel) there are no singular points, and the MRD on the panel is larger than $6.4 r_N$. For $\alpha = 5.92853$ (bottom-right panel) there is a singular point (white square) located at the left side of the separatrix (represented in red). Since in a small neighborhood of the singular point the averaged Hamiltonian is not conjugate to the original

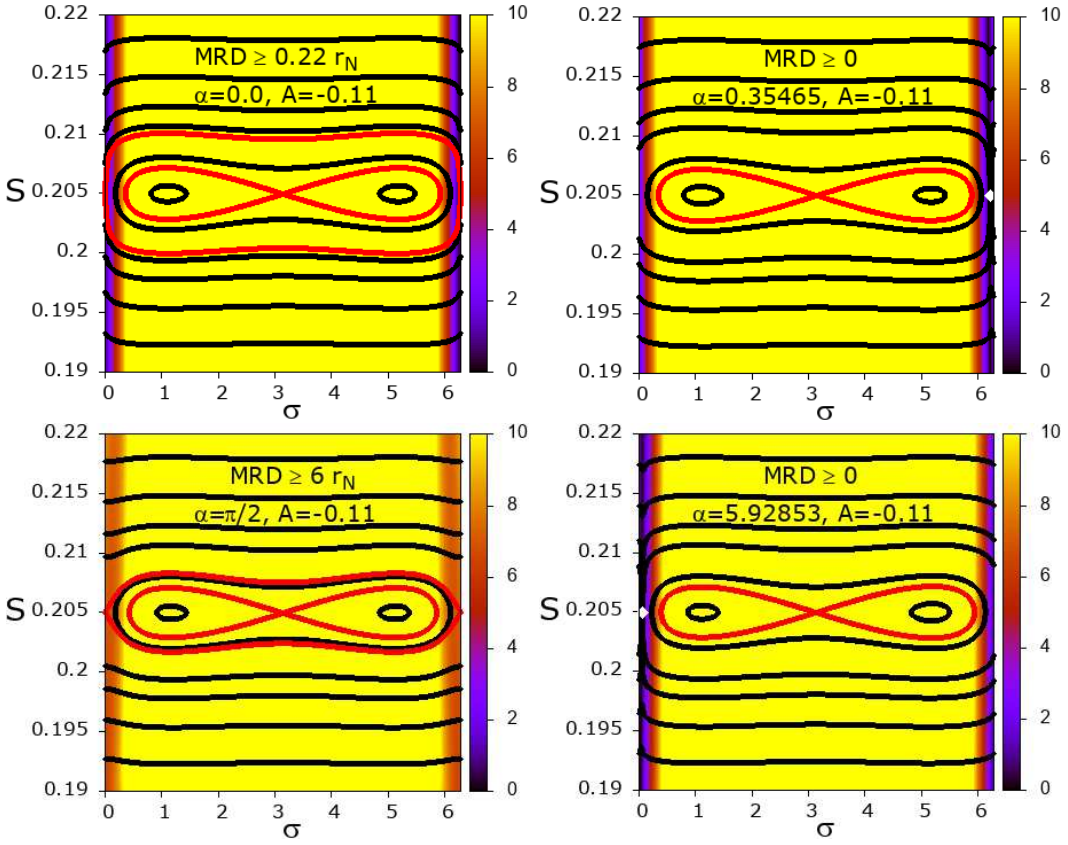

Figure 4.9: Level curves of the averaged Hamiltonian on the σ, S plane for the Sun-Neptune mass ratio, $N = -0.85, A = -0.11$ and $\alpha = 0$ (top-left), $\alpha = \alpha_* = 0.35465$ (top-right), $\alpha = \pi/2$ (bottom-left), $\alpha = \alpha_* = 5.92853$ (bottom-right). The ratio between the MRD and r_N is represented on the background of the panels using a color scale; the minimum value attained on the panel is also indicated. The red level curves contain critical points of the averaged Hamiltonian; the white square in the right panels indicate the singular points.

Hamiltonian by the averaging transformation defined in Section 4.1, we do not represent the level curves of $\widehat{\mathcal{H}}^{Ave}$ passing through a small neighborhood of the singular point, and so in this case we loose the larger separatrix that is represented in the left panels. The lack of a separatrix curve does not prevent the definition of different regions of the σ, S points, according to the libration or circulation properties of the angle σ along a level curve of $\widehat{\mathcal{H}}^{Ave}$.

In Fig. 4.10 we provide examples for $A = -0.02$, close to its upper value. In this case, there are singular points in the (σ, S) plane for all the values of α (see Fig. 4.2), so we have different possibilities depending on whether the singular point is in the resonant region or not. For $\alpha = 0$ (top-left panel) the singular

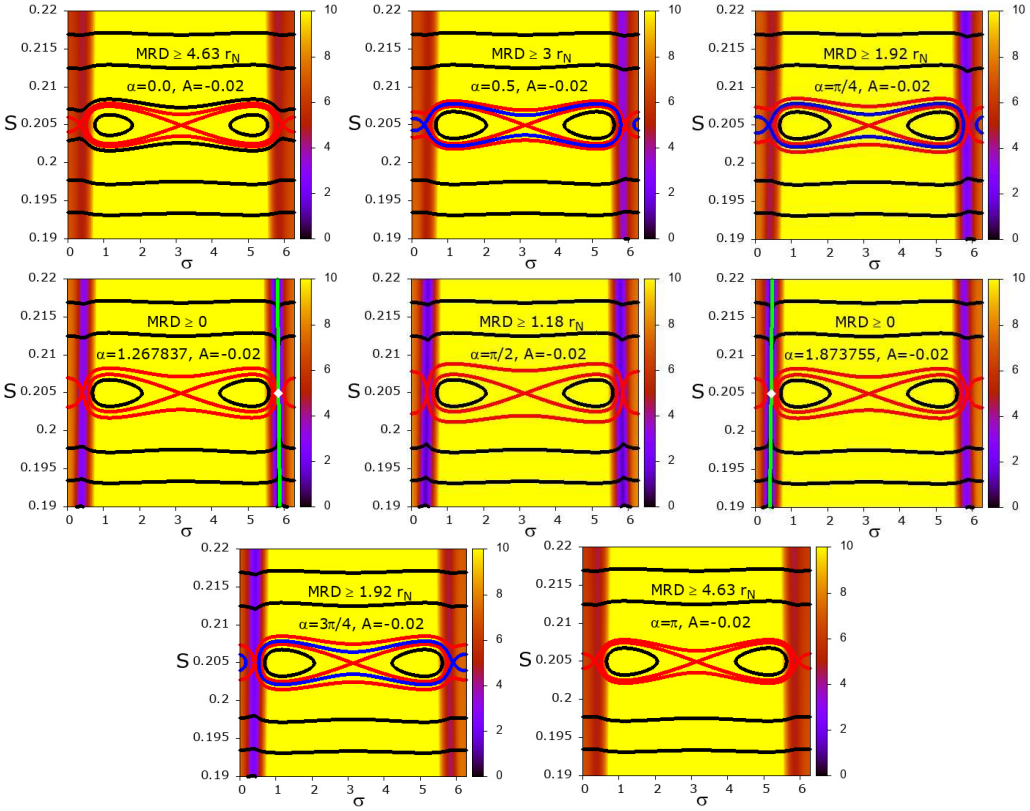

Figure 4.10: Level curves of the averaged Hamiltonian represented on the σ, S plane for the Sun-Neptune mass ratio, $N = -0.85, A = -0.02$ and $\alpha = 0, 0.5, \pi/4, 1.267837, \pi/2, 1.87375, 3\pi/4, \pi$ (from top-left to bottom-right). The ratio between the MRD and r_N is represented on the background of the panels using a color scale; the minimum value attained on the panel is also indicated. The red level curves contain critical points of the averaged Hamiltonian; the white square in the right panel indicates a singular point; the light-blue lines represent the curve $\sigma = \hat{\sigma}(S, A, N)$ (see Eq. (4.22)). The white squares are the singular points. The red and blue curves represent separatrices.

points are outside the resonant region and for all points of the panel MRD $\geq$ $4.63\, r_N$. For $\alpha = 0.5$ (top-center panel) in the resonant region there are no singular points, nevertheless we have relatively small values of MRD $\geq 3.07\, r_N$; we also note that the phase portrait exhibits greater complexity: different minimum values of MRD in the left and right critical points and three separatrices enclosed by each other (we will call them inner, big, and outer separatrices from inside to outside), compare with the symmetric case of $\alpha = 0$ (top-left panel). Similar asymmetric structures also appear for $\alpha = \pi/4$ (top-right panel), where the minimum value of MRD decreases to $1.92\, r_N$ Neptune's Hill radii. As the value of α increases

to the singular value $\alpha = \alpha_* = 1.267837$ (center-left panel), a singular point shows up (indicated with a white square) and the outer separatrix, along with its saddle point, disappears. For $\alpha = \pi/2$ (center-middle panel) the big separatrix disappears and we have symmetric phase portrait. For $\alpha = \alpha_* = 1.873755$, a singular point shows and the outer separatrix disappears. Note the two singular values $\alpha_* = 1.267837$ and $\alpha_* = 1.873755$ are symmetric with $\pi/2$. For the bottom panels $\alpha = 3\pi/4$ and $\alpha = \pi$, we appreciate the similar but "symmetric" structures with $\alpha = \pi/4$ and $\alpha = 0$, respectively; besides, the minimum MRDs of $\alpha = 3\pi/4$ and $\alpha = \pi$ are exactly equal to those of $\alpha = \pi/4$ and $\alpha = 0$, respectively.

In the following we present examples of two different kinds of motions, selected according to the different impact of close encounters on their long-term dynamics.

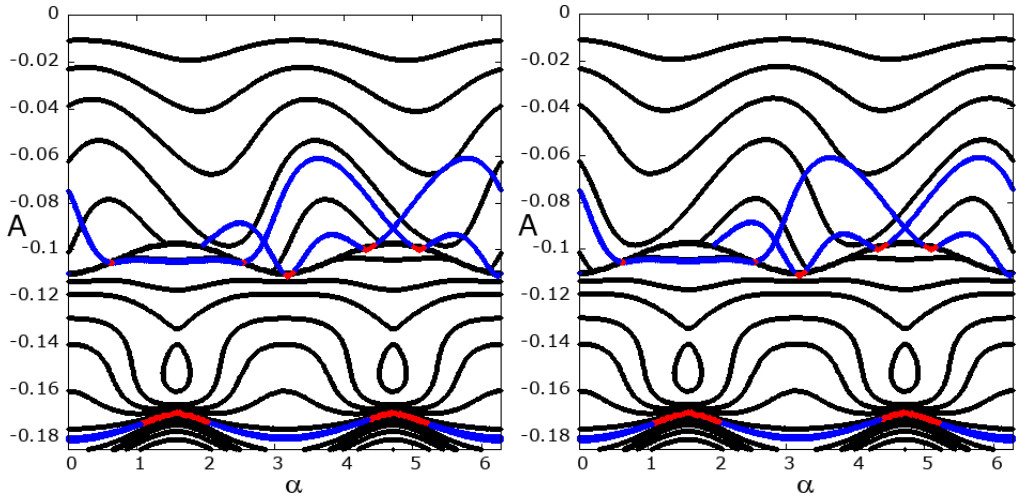

Figure 4.11: Dynamics of two orbits selected for $N = -0.85$, $h = -0.51998502949854775$ and $A = -0.11, \alpha = 0$ (orbit 1); $A = -0.18, \alpha = 0$ (orbit 2). Projection of the 2 orbits on the (α, A) plane (after averaging), for $t < 863000$ (orbit 1, on the top) and $t < 744500$ (orbit 2, on the bottom); the red dots indicate when the orbits are very close to a separatrix); on the same panel we also represent the level curves of the adiabatic invariant $\mathcal{I}$ (see Eq. (4.29)) for the given value h of the averaged Hamiltonian and of N, and for the regions I, III and IV (from top to bottom in the left panel) and for the regions II, III, IV (from top to bottom in the right panel); the two bold curves in both panels represent the separatrices between different zones. See also Fig. 4.12.

The first one refers to motions which are well within the resonant domain in the σ, S plane, so that they do not have deep close encounters with P_1; for example, they may be close to or inside the inner separatrices in the panels of Fig. 4.9, or correspond to values of A for which there are no deep close encounters. Since

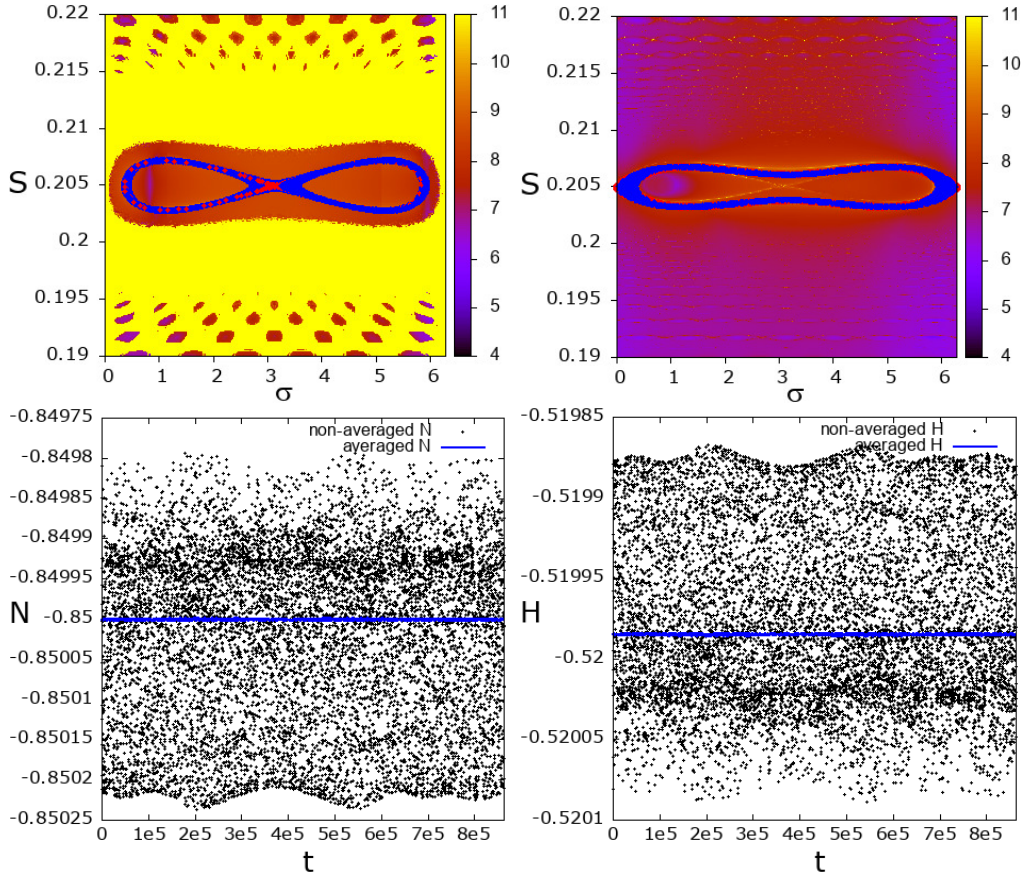

Figure 4.12: Dynamics of two orbits selected for $N = -0.85$, $h = -0.51998502949854775$ and $A = -0.11, \alpha = 0$ (orbit 1); $A = -0.18, \alpha = 0$ (orbit 2), see also Fig. 4.11 for level curves of the adiabatic invariant $\mathcal{I}$. Top panels: projection of orbit 1 (left panel) and orbit 2 (right panel) on the (σ, S) plane (after averaging). On the background we represent the FLI computed of the initial values of α, A of orbit 1 and 2 respectively, for $T = 10000$ units of the fictitious time of the KS regularization. Bottom panels: representation of the time evolution of the action N (left) and of the averaged Hamiltonian $\widehat{\mathcal{H}}^{Ave}$ (right) before (in black) and after (red) the application of the averaging transformation, for orbit 1.

in these cases we expect very good conservation of $\widehat{\mathcal{H}}^{Ave}$ and N (after averaging) along the motion, we analyze orbits with the same initial value h of the averaged Hamiltonian (in addition to N) so that we can compare their projection on the α, A secular plane with the level curves of the adiabatic invariant obtained by fixing both values of $\widehat{\mathcal{H}}^{Ave}$ and N. Fig. 4.11 shows the dynamics of two chaotic orbits with initial value h identifying the inner separatrix of the top-left panel in Fig. 4.9. The projection of the orbits (after averaging) on the planes α, A

is represented on the top panels: orbits (1) and (2) are chaotic, and their secular dynamics follow the level curves of the adiabatic invariants defined for regions I,III and II,III, and III,IV respectively. The good agreement of the secular dynamics of all these orbits with the level curves of the adiabatic invariants represented in the top panels is a consequence of the very good conservation of N and $\widehat{\mathcal{H}}^{Ave}$ along the orbits. Bottom panels of the Fig. 4.12 illustrate the time variation of N and of the averaged Hamiltonian $\widehat{\mathcal{H}}^{Ave}$ for orbit (1). The time evolution for orbit 2 is not represented for brevity since they have very similar behavior with orbit 1. We also remark that these orbits, despite corresponding to the large value of $N = -0.85$, are not subject to deep close encounters: along the numerical integration we detect that the minimum value of $\|P - P_1\|$ is larger than $8\, r_N$ for both orbits. In the top panels of Fig. 4.12 we represent the projection of the two orbits on the σ, S plane (after averaging), with the values of the regularized FLI computed for $T = 10000$ reported in the background: we notice that both chaotic orbits are surrounded by regions of regular motions.

The second kind of resonant dynamics contains motions which initially are in the peripheral region of the resonance, and are characterized by deep close encounters with P_1. In Fig. 4.13 we consider initial values of N, A, α for which we have a singular point in the resonant region of the σ, S plane (white point in the top-right panel), as well as a region characterized by small values of the MRD crossing the resonance. The red point in the panel (very close to the singular point) belongs to the large libration highlighted in blue, and indicates the initial conditions of σ, S for the orbit analyzed in the other panels which represent the project on the σ, S plane (top-right panel) and the time evolution of N (bottom-left) and of the semi-major axis (bottom-right). Different time intervals are highlighted with different colors: in the first time interval (correspondingly, the projection on the σ, S plane is in red; top-right panel) the orbit is performing large librations with $\|P - P_1\| \simeq 0.06$, but at the end of the interval crosses the larger separatrix and afterwards, close encounters at $\|P - P_1\| \simeq 0.015$ extract the orbit from the resonance. In the next time interval (indicated in blue), the orbit is outside the larger separatrix and performs circulations crossing the region of small MRD determining variations of N (and of the averaged Hamiltonian, not reported for brevity) and also of the semi-major axis. This sequence of close encounters determines the diffusion of the orbit towards a nearby resonance of larger order. In fact, at the beginning of the third time interval (indicated in brown) the semi-major axis oscillates close to $a \simeq 1.41$, and after other sequences of close encounters it oscillates close to $a \simeq 1.36$ (at the end of the magenta interval). The diffusion towards nearby resonances is also represented in Fig. 4.14 for a set of 20 orbits with very close initial conditions near the initial conditions for σ, S indicated by the red dot in the top-left panel of Fig. 4.13. In the left panel we see the diffusion of the set of

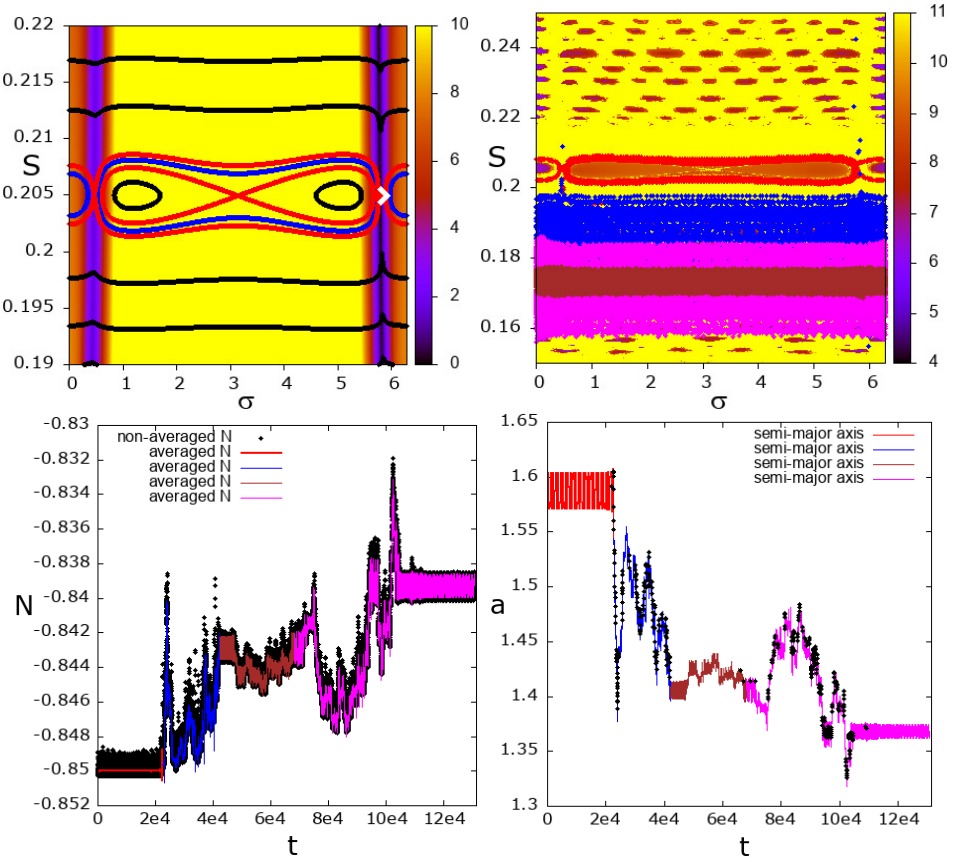

Figure 4.13: Top-left panel: level curves of the averaged Hamiltonian represented on the σ, S plane for $N = -0.85, A = -0.01$, $\alpha = 1.316903$; the ratio between the MRD and r_N is represented on the background of the panels using a color scale; the white square indicates a singular point; the red square (very close to the singular point) indicates the initial values of σ, S for the orbit analyzed in the other panels. Top-right panel: projection on the (σ, S) plane (after averaging) of the orbit with initial conditions indicated in the right panel, for $t < 130855$; on the background we represent the FLI computed for the same initial values of α, A and $T = 10000$ (see Eq. (4.32)); the different colors used for the orbit projection correspond to different time intervals (red, blue, brown, magenta for $[0, 22603]$, $[22603, 42281.2]$, $[42281.2, 68246]$, $[68246, 130854.7]$ respectively). Bottom-left panel: time evolution of the action N before (black) and after (red, blue, brown, magenta as explained above) the application of the averaging transformation. Bottom-right panel: time evolution of the value of the semi-major axis; the black dots indicates a close encounter at distance $\|P - P_1\| < 0.05$.

orbits from the border of the resonance to its exterior, due to a sequence of close

encounters (indicated by the red dots). The accumulation of the effects of close encounters determines also the chaotic diffusion of the action N. The exit from the 1:2 MMR resonance is also appreciated from the spread of the values of the semi-major axis, reported in the right panel.

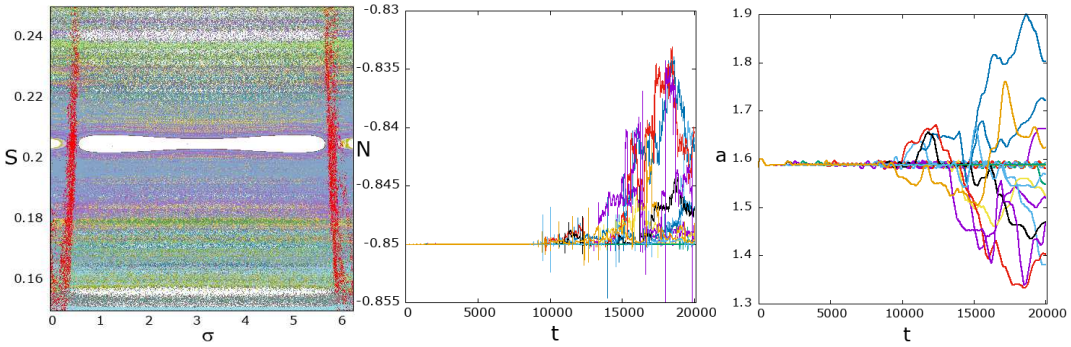

Figure 4.14: Diffusion in the phase space for orbits with 20 initial conditions close to the orbit previously selected for Fig. 4.13. The 20 initial conditions have the same value of N, A, α, while σ, S are regularly spaced in a segment joining $(\sigma_1, S_1) = (5.7229756139649535, 0.20490981963927857)$ and $(\sigma_2, S_2) = (5.7229573588698726, 0.20496993987975951)$. For the 20 orbits we represent: the projection on the (σ, S) plane (after averaging) for a maximum value of t in a range between 10^5 and 2×10^5 corresponding to the same fictitious regularized time (left panel; the red dots indicate where a close encounter at $\|P - P_1\| < 0.05$ occurs); the time evolution of N (after averaging; center panel); the time evolution of the semi-major axis (right panel; a running average along a window of $\Delta t = 500$ has been applied).

Note that the application of perturbation theory to describe chaotic orbits, particularly for time spans exceeding their Lyapunov times, is justified in the following sense. Perturbation theory correctly establishes the conservation of relevant approximate integrals, while only some variables are subject to diffusion. The time evolution of these variables may differ significantly for very close initial conditions, as evident in Fig. 4.14. Consequently, while normal forms and numerical integrations may not accurately predict individual orbits, they do provide correct statistical properties, such as the spread of a set of orbits as it is detected in Fig. 4.14 (for analytical details on this topic, see also [GuzEP20]).

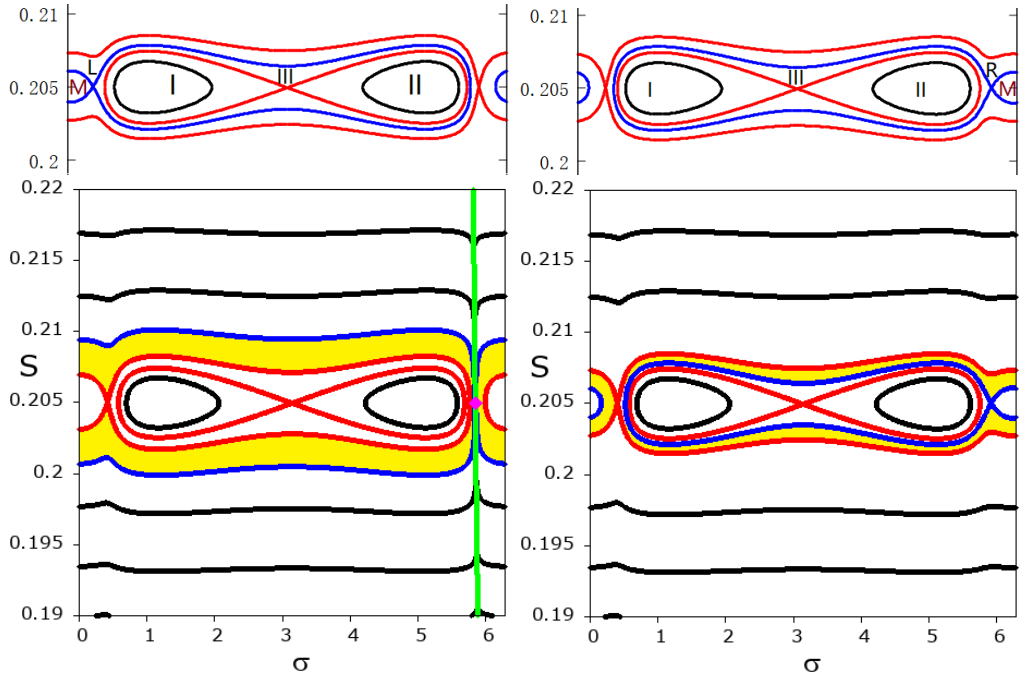

Figure 4.15: Classification of libration regions for $N = -0.85$. The pictures are from the phase portraits of $\widehat{\mathcal{H}}^{Ave}$ for $N = -0.18, A = -0.02$ and $\alpha = \pi/4$ (left), $\alpha = 3\pi/4$ (right). Note the upper and lower circulation regions will be denoted as Region IV and Region V, consistent with the aforementioned classification. The yellow regions in bottom panels are region L and region R.

4.3 Appendix and remarks

4.3.1 Classification of regions in Phase-Space

We provide some representations of the phase-portraits that illustrate how the different resonant regions are classified based on the complicated structure of the separatrices according to the different values of α, A (see Fig. 4.15). In particular, since for different values of α, A, we have different numbers of separatrices and singular points, more regions will appear corresponding to the bifurcations of the system. In Fig. 4.15, regions I, II, and III always exist due to the existence of the inner separatrix (related to the unstable equilibrium near $\sigma = \pi$). The level curves inside region I correspond to librations around the left fixed point, and the level curves in region II correspond to librations around the right fixed point. Note, outside the inner separatrix there always exists one or two additional separatrices, depending on the values of α, A, and the region between them is classified as region III. Level curves in region III represent librations around the unstable fixed point

near $\sigma = \pi$. If a level curve corresponds to a libration around the stable fixed point near $\sigma = 0$ (when this stable fixed point exists), we classify it as the inside region M. Level curves in region L (or R) represent librations around the two stable fixed points, the unstable fixed point near $\sigma = \pi$, and the stable fixed point near $\sigma = 0$. Then the remaining level curves will be circulations, located in region IV (upper circulations) and region V (lower circulations). Note that regions L and R are well defined even if there are singular points, see bottom panels of Fig. 4.15 for examples.

4.3.2 Adiabatic invariants for the CRTBP inside MMRs

The use of adiabatic invariants to study the long-term dynamics of MMRs of the SCRTBP is well established (for instance, see [Wis82, Wis83, Wis85, Nei87, NesTFM02, NeiSido04, Sido06, SidoNAZ14, Huang18, Lei22, Sido24, Pan25]). For a fixed value of N, the equations of motion of the averaged Hamiltonian (see Eq. (4.27)):

$$\dot{\sigma} = \frac{\partial \widehat{\mathcal{H}}}{\partial S}, \qquad \dot{S} = -\varepsilon \frac{\partial \widehat{\mathcal{H}}_1^{Res}}{\partial \sigma},$$
$$\dot{\alpha} = \varepsilon \frac{\partial \widehat{\mathcal{H}}_1^{Res}}{\partial A}, \qquad \dot{A} = -\varepsilon \frac{\partial \widehat{\mathcal{H}}_1^{Res}}{\partial \alpha},$$

have different timescales: the shorter one characterizing the time evolution of the resonant variables S, σ and the longer one characterizing the time evolution of A, α. Therefore, it is natural to apply the theory presented in [Nei87b] for the Hamiltonian systems of 2 degrees of freedom, having fast and slow evolution. In this Section, we recall the fundamental aspects of this theory that are utilized also in this paper, to study the dynamics of the 1:2 MMR.

Within the time scale $T << \frac{1}{\varepsilon}$ the slower variables (α, A) could be regarded as frozen to a constant value, and the motion of the faster variables (σ, S) could be described by the corresponding "frozen" Hamiltonian (see Eq. (4.7))

$$\widehat{h}(S, \sigma; N_0, A_0, \alpha_0) := -\frac{1}{(qS - N_0)^2} - n_1 p S + \varepsilon c_0(S, \sigma; N_0, A_0, \alpha_0), \tag{4.28}$$

where (N_0, A_0, α_0), which are the initial values of the corresponding action-angle variables, are treated as parameters. In suitable librational or rotational domains of the one-degree-of-freedom reduced Hamiltonian $\widehat{h}$ one introduces the action-angle variables $\phi, \mathcal{I}$, where

$$\mathcal{I} = \frac{1}{2\pi} \oint_{\widehat{h}=h} S d\sigma, \tag{4.29}$$

is called adiabatic invariant (the integration is defined on the cycle $\widehat{h} = h$ corresponding to a libration or a circulation), and ϕ is a conjugate angle. The integral is related to an area enclosed or delimited by the integration path. See Fig. 4.16 for the illustration.

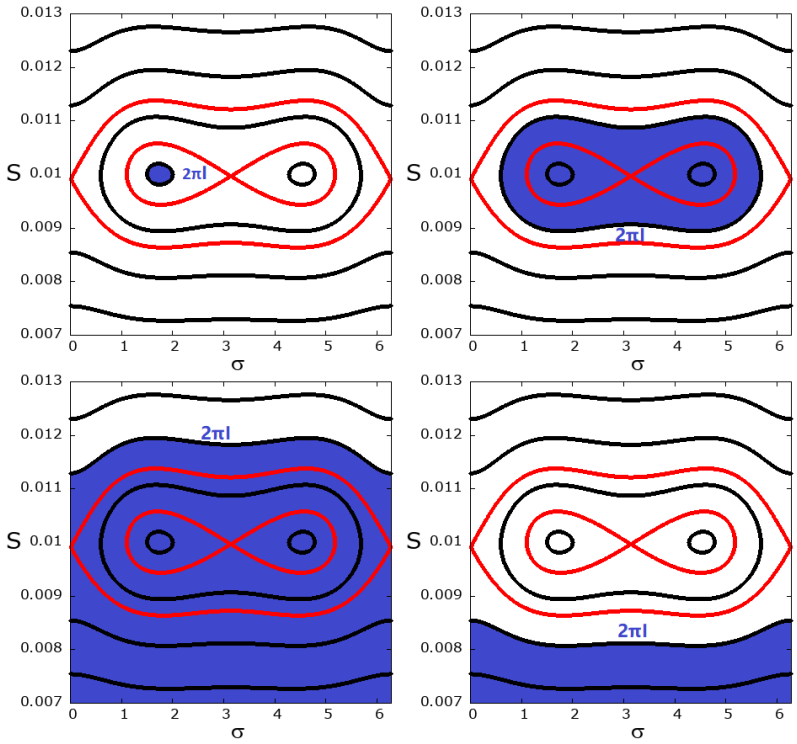

Figure 4.16: Definition of the adiabatic invariant, corresponding to the area enclosed by level curves of the averaged Hamiltonian in the resonant phase space.. The phase portraits are obtained with $N_0 = -1.24, A_0 = -0.003, \alpha_0 = 0.0$. The red curves are separatrix. The area of the blue shaded region is equal to $2\pi J$.

To account for the time variation of the secular variables A, α, in accordance with the theory presented in [Nei87b], a canonical transformation is defined for each distinct librational or rotational domain of the one-degree-of-freedom reduced Hamiltonian $\widehat{h}$:

$$(S, A, \sigma, \alpha) \mapsto (\mathcal{I}, A', \phi, \alpha')$$

such that (A', α') is closed to (A, α), conjugating $\widehat{h}$ to a perturbation of the function (we omit the use of 'primes' for simplicity) $\mathcal{F}(N, \mathcal{I}, A, \alpha)$, which is obtained by expressing the function (4.28) in terms of the adiabatic invariant $\mathcal{I}$ instead of S, σ. Since the Hamiltonian flow of $\mathcal{F}(N, \mathcal{I}, A, \alpha)$ has the constant of motions

$\mathcal{I}$, it defined a one-degree-of-freedom Hamiltonian for the motion of the variables (A, α).

The adiabatic approximation for the motion of the variables (A, α) given by the Hamiltonian $\mathcal{F}(N, \mathcal{I}, A, \alpha)$ is valid when the system remains within the librational or rotational domain where the adiabatic invariant $\mathcal{I}$ is defined. But the separatrices delimiting such domain may change along time because of the secular variation of the variables (A, α), forcing the system to approach a separatrix. When the motion enters a small neighborhood of the separatrix this adiabatic approximation is no more valid. As an example, we refer to Fig. 4.4 where we represent the phase-portrait of the Hamiltonian $\widehat{h}$ in the (σ, S) plane (top-left panel) as well as the level curves of the adiabatic invariant $\mathcal{I}(N, A, \alpha; h)$ in the secular phase-plane A, α (bottom panels), computed for a fixed value h of the averaged Hamiltonian and of the action N. In particular, the bottom-left panel shows the separatrix crossing between region II and region III and the center-right one is related to separatrix crossing between region I and region III. The bold curve is due to the different definition of the adiabatic invariants $\mathcal{I}$ at the two sides of the separatrix.

4.3.3 The Fast Lyapunov Indicator

The Fast Lyapunov Indicator computed in this Chapter are defined, as indicated in Section 2.5, from the variational dynamics of the equations of motions of the non-averaged CRTBP regularized at P_1 with the Kustaanheimo-Stiefel regularization, see [GuzL18, GuzL23, RosG24]. The definition of the KS regularization is also given in Section 2.4.3.

Let us denote with: $u \in \mathbb{R}^4$ the KS variables; s the fictitious time related to the physical time by $dt = \|P - P_1\| ds$; $v = du/ds$; $\xi = (u, v)$ the variables of the KS state-space; $w = (w_u, w_v) \in \mathbb{R}^8$ the tangent vector to the space of the variables $\xi = (u, v)$. For any initial datum ξ_0 of the equations of motion of the CRTBP regularized at P_1 with the Kustaanheimo-Stiefel regularization:

$$\frac{d\xi}{ds} = F(\xi), \tag{4.30}$$

and any initial tangent vector w_0, we consider the solution $\xi(s)$ of Eq. (4.30) with initial conditions ξ_0, and the solution $w(s)$ of the variational equations of (4.30):

$$\frac{dw}{ds} = \frac{\partial F}{\partial \xi}(\xi(s))w \tag{4.31}$$

with initial conditions w_0. The regularized Fast Lyapunov Indicator of the initial

condition ξ_0, initial tangent vector w_0 and fictitious time T is defined as:

$$FLI(\xi_0, w_0; T) = \max_{0 \leq s \leq T} \log_{10} \frac{\|w(s)\|}{\|w(0)\|}. \tag{4.32}$$

4.4 Conclusions

The analysis of the singular sets and the computation of the FLI and MRD allow to select and analyze the behavior of orbits in a MMR of the spatial CRTBP having close encounters with a planet. There is a difference in the chaotic diffusion when close encounters may happen only at moderate distance from the planet: in such a case we have two quasi-conserved quantities (N and $\widehat{\mathcal{H}}^{Ave}$ in this Chapter), so the secular dynamics may be analyzed by considering, in the secular plane of the variables α, A, the level curves of the adiabatic invariants obtained for fixed values of these quantities. In this case, we observe the well-known mechanism of chaos generation due to the crossing of a separatrix. Instead, when deep close encounters are possible, we observe also a step-wise diffusion of N and $\widehat{\mathcal{H}}^{Ave}$, which superimposes on the chaotic effects due to the crossing of a separatrix. For some orbits, this diffusion determines the extraction from the given MMR and its migration towards other MMRs, overlapping with the initial one. The analytic characterization of this diffusion, in our opinion, could be done in a future work by developing for the specific case of the semi-analytic theory of [GuzEP20].

Appendix A

Computation of the perturbation function $\widehat{\mathcal{H}}_1$ with resonant variables

Recall that the perturbation part for spatial problem is

$$\widehat{\mathcal{H}}_1(a,e,i,\omega,f,\Omega,\lambda_1) = -\left(\frac{1}{\sqrt{r^2+1-2r\cos\psi}} - r\cos\psi\right),$$

where $r = a(1-e\cos E)$, E is the eccentric anomaly of P, and

$$\cos\psi = \cos(i)\sin(f+\omega)\sin(\lambda_1-\Omega) + \cos(f+\omega)\cos(\lambda_1-\Omega),$$

of which all variables are related to the resonant variables but Θ. According to the definition of modified Delaunay variables, we have

$$\begin{aligned} a &= (qS-N)^2, \\ e &= \sqrt{1-\left(1-\frac{S+A}{qS-N}\right)^2}, \\ \cos(i) &= 1+\frac{A}{pS-N-A}, \end{aligned}$$

with given values of N, S, A one can compute the semi-major axis a, the eccentricity e, and the inclination i.

We compute the mean anomaly M from the values of $\sigma, \nu+\theta$:

$$M = \lambda + \varphi = \sigma + p(\nu+\theta).$$

By computing numerically the solution E of Kepler's equation $M = E - e\sin E$, one gets the value of eccentric anomaly. Finally the value of $\cos\psi$ is computed as

follows. First we have

$$\begin{aligned}\cos\psi = &\cos(i)\sin(\lambda_1-\Omega)\left(\sin f\cos\omega+\cos f\sin\omega\right)\\ &+\cos(\lambda_1-\Omega)\left(\cos f\cos\omega-\sin f\sin\omega\right),\end{aligned}$$

and next from the definition of resonant action angle variables we have:

$$\begin{aligned}\omega &= -\alpha,\\ \theta-\Omega &= \sigma-\alpha+q(\nu+\theta),\end{aligned}$$

finally we compute $\cos f$ and $\sin f$ with

$$\tan\frac{f}{2}=\sqrt{\frac{1+e}{1-e}}\tan\frac{E}{2}.$$

As a consequence, the value of $\widehat{\mathcal{H}}_1(S,N,A,\sigma,\alpha,\nu+\theta)$ is computed for any given value of $(S,N,A,\sigma,\alpha,\nu+\theta)$.

All the numerical computations of this thesis have been obtained by my implementation with Fortran language, using also subroutines from: Numerical Recipes in Fortran [NumRecipe77]; from the graphical library PGPLOT[1]; from the library Swift[2]. The pictures have been obtained using Gnuplot, Wolfram Mathematica and the PGPLOT libaray.

[1]https://sites.astro.caltech.edu/ tjp/pgplot/
[2]https://www2.boulder.swri.edu/ hal/swift.html

Acknowledgements

I wish to acknowledge my advisor Massimiliano Guzzo for introducing me to this topic. In these three years, we met almost every week. His patience and suggestions gave me very important guide for this thesis, and also for my future life.

I would like to thank Prof. Elena Lega for her co-supervision, Prof. Vladislav Sidorenko for the helpful discussions, Prof. Gabriella Pinzari for her lectures about KAM and supervision for my master thesis, and Prof. Lei Zhao and Prof. Urs Frauenfelder for their support and useful discussions during my visiting in Augsburg.

Besides, I am also grateful to the people I meet in different conferences, workshops and summer schools, in Namur, Firenze, Verona, Augsburg, Heidelberg, Cetraro, and Strobl. I wish to thank the reviewers Prof. G. Baù and Prof. C. Lhotka for carefully reading the thesis and providing useful advice for improving the final version.

I would also like to thank all students of the 7th floor, specifically of the 38th cycle. I would like to thank Tommaso Bertin, Giacomo Ceccherini, Pietro De Checchi, Martina Galeazzo, Beatrice Ongarato, Giacomo Passuello, Runlei Xiao, David Klompenhouwer, Gianluca Somma, Francesca Berlinghieri and Anastasios Slaftsos, for the support they gave me and the time we spent together inside bars and restaurants.

With all my love and tears, I want to thank Alessandra Nardi, Marco Di Marco, Ishan Singh, Francesco Fantin, and Gaia Marangon for the love, the support, the chats, the fun, the mutual help, the laugh, the tears, the beers, the football e la vita bella.

Finally I would like to express my deep gratitude to my family for their infinite love, support, and understanding.

Bibliography

[AntoLib18] K. I. Antoniadou and A. S. Libert: Origin and continuation of 3/2, 5/2, 3/1, 4/1 and 5/1 resonant periodic orbits in the circular and elliptic restricted three-body problem. Celestial Mechanics and Dynamical Astronomy, Vol. 130, art. 41, 2018.

[Bea94] C. Beagué: Asymmetric Librations in Exterior Resonances. Celestial Mechanics and Dynamical Astronomy, 60:225-248, 1994.

[BeneGGS80a] G. Benettin, L. Galgani, A. Giorgilli, and J. M. Strelcyn: Lyapunov Characteristic Exponents for smooth dynamical systems and for hamiltonian systems; a method for computing all of them. Part 1: Theory. Meccanica, Vol. 15, pp.9-20, 1980.

[BeneGGS80b] G. Benettin, L. Galgani, A. Giorgilli, and J. M. Strelcyn: Lyapunov Characteristic Exponents for smooth dynamical systems and for hamiltonian systems; A method for computing all of them. Part 1: Numerical application. Meccanica, Vol. 15, pp.21-30, 1980.

[BraGS14] P.I. O. Brasil, R. S. Gomes, and J. S. Soares: Dynamical formation of detached trans-Neptunian objects close to the 2:5 and 1:3 mean motion resonances with Neptune. Astronomy and Astrophysics, Vol. 564, art. A44, 2014.

[CardG22] F. Cardin and M. Guzzo: Integrability of close encounters in the spatial restricted three-body problem. Communications in Contemporary Mathematics, Vol. 24, No. 06, 2022.

[CavE22] I. Cavallari and C. Efthymiopoulos: Closed-form perturbation theory in the restricted three-body problem without relegation. Celestial Mechanics and Dynamical Astronomy, 134:16, 2022.

[CelSLF11] A. Celletti, L. Stefanelli, E. Lega, C. Froeschlé: Some results on the global dynamics of the regularized restricted three-body problem with dissipation. Celest Mech Dyn Astr 109, 265–284, 2011.

[Chirikov] B. V. Chirikov: A universal instability of many-dimensional oscillator systems. Physics Reports, Vol. 52, pp. 263-279, 1979.

[Chodas99] P. W. Chodas: Orbit Uncertainties, Keyholes, and Collision Probabilities. AAS/Division for Planetary Sciences Meeting Abstracts, Vol. 31, 1999.

[CinS00] P. M. Cincotta and C. Simò: Simple tools to study global dynamics in non-axisymmetric galactic potentials - I. Astronomy and Astrophysics Supplement Series, Vol. 147, pp. 205-228, 2000.

[EfimS20] S. S. Efimov and V. V. Sidorenko: On Asymmetric Zeipel-Lidov-Kozai Cycles in Mean Motion Resonances. Cosmic Research, Vol. 58, pp. 249-255, 2020.

[Féj16] J. Féjoz, M. Guàrdia, V. Kaloshin, and P. Roldán: Kirkwood gaps and diffusion along mean motion resonances in the restricted planar three-body problem. Journal of the European Mathematical Society, 18, 2315-2403, 2016.

[FenGS22] M. Fenucci, G. F. Gronchi, and M. Saillenfest: Proper elements for resonant planet-crossing asteroids. Celestial Mechanics and Dynamical Astronomy, 134:23, 2022.

[FerS89] S. Ferraz-Mello and M. Sato: The very-high-eccentricity asymmetric expansion of the disturbing function near resonances of any order. Astronomy and Astrophysics, 225:541-547, 1989.

[Fer87] S. Ferraz-Mello: Expansion of the disturbing force-function for the study of high-eccentricity librations. Astronomy and Astrophysics, 183:397-402, 1987.

[Fer07] S. Ferraz-Mello: Canonical perturbation theories, degenerate systems and resonance. Springer, 2007.

[Fer24] S. Ferraz-Mello: Chaotic Dynamics in Planetary Systems. Springer Nature, 2024.

[Fro70] C. Froeschlé: Numerical Study of Dynamical Systems with Three Degrees of Freedom I. Graphical Displays of Four-Dimensional Sections. Astronomy and Astrophysics, Vol. 5, pp. 115-128, 1970.

[FroGL97a] C. Froeschlé, R. Gonczi, and E. Lega: The fast Lyapunov indicator: a simple tool to detect weak chaos. Application the structure of the main asteroidal belt. Planetary and Space Science, Vol. 45, pp. 881-886, 1997.

[FroLG97b] C. Froeschlé, E. Lega, and R. Gonczi: Fast Lyapunov Indicators. Application to asteroidal motion. Celestial Mechanics and Dynamical Astronomy, Vol. 67, pp. 41-62, 1997.

[FroGL00] C. Froeschlé, M. Guzzo, and E. Lega: Graphical evolution of the Arnold web: from order to chaos. Science, 289:2108-2110, 2000.

[FroGL01] C. Froeschlé, M. Guzzo, and E. Lega: The Fast Lyapunov Indicator: detection of the Arnold web for Hamiltonian systems and symplectic mappings with 3 degrees of freedom. In SSUP Proceedings: The Restless Universe. Application of gravitational N-body dynamics to planetary, stellar and galactic systems. Editors B. A. Steves and A. J. Maciejewsky, 2001.

[FroGL05a] C. Froeschlé, M. Guzzo, and E. Lega: First numerical evidence of global Arnold diffusion in quasi-integrable systems. Discrete and Continuous Dynamical Systems - B, Vol. 5(3): 687-698, 2005.

[FroGL05] C. Froeschlé, M. Guzzo, and E. Lega: Local And Global Diffusion Along Resonant Lines in Discrete Quasi-integrable Dynamical Systems. Celestial Mechanics and Dynamical Astronomy, Vol. 92, pp. 243-255, 2005.

[GalHP12] T. Gallardo, G. Hugo, and P. Pais: Survey of Kozai dynamics beyond Neptune. Icarus, Vol. 220, pp. 392-403, 2012.

[Gal18] T. Gallardo: Resonances in the asteroid and trans-Neptunian belts: A brief review. Planetary and Space Science, Vol. 157, pp. 96-103, 2018.

[Gal20] T. Gallardo: Three-dimensional structure of mean motion resonances beyond Neptune. Celestial Mechanics and Dynamical Astronomy, 132:9, 2020.

[Gior22] A. Giorgilli: Notes on Hamiltonian Dynamical Systems. Cambridge University Press; 2022.

[GreenCV88] R. Greenberg, A. Carusi, and G. B. Valsecchi: Outcomes of planetary close encounters: A systematic comparison of methodologies. Icarus, Vol. 75, pp. 1-29, 1988.

[GroM98] G. F. Gronchi and A. Milani: Averaging on Earth-Crossing Orbits. Celestial Mechanics and Dynamical Astronomy, 71:109-136, 1998.

[GroT12] G. F. Gronchi and C. Tardioli: The evolution of the orbit distance in the double averaged restricted 3-body problem with crossing singularities. Discrete and Continuous Dynamical Systems - Series B, 18:1323-1344, 2012.

[Guzzo05] M. Guzzo: The web of three-planet resonances in the outer Solar System. Icarus, Vol. 174, pp. 273-284, 2005.

[Guzzo24] M. Guzzo: Parametric approximations of fast close encounters of the planar three-body problem as arcs of a focus-focus dynamics, Nonlinearity, 37, 105011, 2024.

[GuzEP20] M. Guzzo, C. Efthymiopoulos and R. Paez: Semi-analytic computations of the speed of Arnold diffusion along single resonances in a priori stable Hamiltonian systems. Journal of Nonlinear Science, Vol. 30, 851-9010, 2020.

[GuzLF02] M. Guzzo, E. Lega, and C. Froeschlé: On the numerical detection of the effective stability of chaotic motions in quasi-integrable systems. Physica D: Nonlinear Phenomena, Vol. 163, pp. 1-25, 2002.

[GuzLF09a] M. Guzzo, E. Lega, and C. Froeschlé: A Numerical Study of Arnold Diffusion in a Priori Unstable Systems. Communications in Mathematical Physics, Vol. 290, pp. 557-576, 2009.

[GuzLF09] M. Guzzo, E. Lega, and C. Froeschlé: A numerical study of the topology of normally hyperbolic invariant manifolds supporting Arnold diffusion in quasi-integrable systems. Physica D: Nonlinear Phenomena, Vol. 238, pp. 1797-1807, 2009.

[GuzL02] M. Guzzo, E. Lega, and C. Froeschlé: On the numerical detection of the effective stability of chaotic motions in quasi-integrable systems. Physica D: Nonlinear Phenomena, Vol. 163, pp. 1-25, 2002.

[GuzL13] M. Guzzo and E. Lega: On the identification of multiple close-encounters in the planar circular restricted three body problem. Monthly Notices of the Royal Astronomical Society, 428, 2688-2694, 2013.

[GuzL13b] M. Guzzo and E. Lega: The numerical detection of the Arnold web and its use for long-term diffusion studies in conservative and weakly dissipative systems. Chaos, Vol. 23, 023124, 2013.

[GuzL14] M. Guzzo and E. Lega: Evolution of the tangent vectors and localization of the stable and unstable manifolds of hyperbolic orbits by Fast Lyapunov Indicators. SIAM Journal on Applied Mathematics, Vol. 74, No. 4, pp. 1058-1086, 2014.

[GuzL15] M. Guzzo and E. Lega: A study of the past dynamics of comet 67P/Churyumov-Gerasimenko with fast Lyapunov indicators. Astronomy & Astrophysics, vol. 579, A79, 2015.

[GuzL17] M. Guzzo and E. Lega: Scenarios for the dynamics of comet 67P/Churyumov-Gerasimenko over the past 500 kyr. Monthly Notices of the Royal Astronomical Society, Vol. 469, pp. S321-S328, 2017.

[GuzL18] M. Guzzo and E. Lega: Geometric chaos indicators and computations of the spherical hypertube manifolds of the spatial circular restricted three-body problem. Physica D, 373, 38–58, 2018.

[GuzL23] M. Guzzo, E. Lega: Theory and applications of fast Lyapunov indicators to model problems of celestial mechanics, Celest. Mech. Dyn. Astron., Vol. 135, Article number: 37, 2023.

[Hadji93] J. D. Hadjidemetriou: Resonant motion in the restricted three body problem. Celestial Mechanics and Dynamical Astronomy, Vol. 56, pp. 201-219, 1993.

[HenL83] J. Henrard and A. Lemaitre: A Second Fundamental Model for Resonance. Celestial Mechanics, 30:197-218, 1983.

[Huang18] Y. Huang, M. Li, J. Li and S. Gong: Kozai-Lidov mechanism inside retrograde mean motion resonances. Monthly Notices of the Royal Astronomical Society, Vol. 481, pp. 5401-5410, 2018.

[Kust64] P. Kustaanheimo: Spinor regularisation of the Kepler motion. In: Annales Universitatis Turkuensis A 73, pp. 1-7, 1964.

[Kust65] P. Kustaanheimo and E. L. Stiefel: Perturbation theory of Kepler motion based on spinor regularization. In: J. fur die Reine und Angewandte Mathematik, 218, pp. 204-219-569, 1965.

[LasFC92] J. Laskar, C. Froeschlé, and A. Celletti: The measure of chaos by the numerical analysis of the fundamental frequencies. Application to the standard mapping. Physica D: Nonlinear Phenomena, Vol. 56, pp. 253-269, 1992.

[Las93] J. Laskar: Frequency analysis for multi-dimensional systems. Global dynamics and diffusion. Physica D: Nonlinear Phenomena, Vol. 67, pp. 257-281, 1993.

[LegGF03] E. Lega, M. Guzzo, and C. Froeschlé: Detection of Arnold diffusion in Hamiltonian systems. Physica D: Nonlinear Phenomena, Vol. 182, pp. 179-187, 2003.

[LegGF10] E. Lega, M. Guzzo, and C. Froeschlé: A numerical study of the hyperbolic manifolds in a priori unstable systems. A comparison with Melnikov approximations. Celestial Mechanics and Dynamical Astronomy, Vol. 107, pp. 115-127, 2010.

[LegGF11] E. Lega, M. Guzzo, and C. Froeschlé: Detection of close encounters and resonances in three-body problems through Levi-Civita regularization. Monthly Notices of the Royal Astronomical Society, 418, 107-113, 2011.

[LegG16] E. Lega and M. Guzzo: Three-dimensional representation of the tube manifolds of the planar restricted three-body problem, Physica D: Nonlinear Phenomena, Vol. 325, pp. 41-52, 2016.

[LegGF16] E. Lega, M. Guzzo and C. Froeschlé: Theory and Application of the Fast Lyapunov Indicator (FLI) method, chapter in: Chaos Detection and Predictability, pp. 35-54, 2016.

[Lei22] H. Lei, J. Li, X. Huang, and M. Li: The Von Zeipel-Lidov-Kozai Effect inside Mean Motion Resonances with Applications to Trans-Neptunian Objects. The Astronomical Journal, 164:74, 2022.

[Lam84] A. Lemaitre: High-order resonances in the restricted three-body problem. Celestial Mechanics, 32:109-126, 1984.

[LidZ74] M. L. Lidov and S. L. Ziglin: The analysis of restricted circular twice-averaged three body problem in the case of close orbits. Celestial Mechanics, Vol. 9, pp. 151-173, 1974.

[LiuGuzzo25] X. Liu and M. Guzzo: On the limits of application of mean motion resonant normal forms of the three-body problem for crossing orbits and close encounters. Celestial Mechanics and Dynamical Astronomy, 137:1, 2025.

[Mal98] R. Malhotra: Orbital Resonances and Chaos in the Solar System. Solar System Formation and Evolution: ASP Conference Series, Vol. 149, ed. D. Lazzaro; R. Vieira Martins; S. Ferraz-Mello; J. Fernandez; and Beauge, p. 37, 1998.

[MaroG18] S. Maró and G. F. Gronchi: Long Term Dynamics for the Restricted N-Body Problem with Mean Motion Resonances and Crossing Singularities. SIAM Journal on Applied Dynamical Systems, Vol. 17, pp. 1786-1815, 2018.

[MasE23] R. Mastroianni and C. Efthymiopoulos: The phase-space architecture in extrasolar systems with two planets in orbits of high mutual inclination. Celestial Mechanics and Dynamical Astronomy, 135:22, 2023.

[MasL23] R. Mastroianni and U. Loatelli: Secular orbital dynamics of the innermost exoplanet of the υ-Andromedæ system, Celestial Mechanics and Dynamical Astronomy, 135:28, 2023.

[MilB98] A. Milani and S. Baccili: Dynamics of Earth-crossing asteroids: the protected Toro orbits. Celestial Mechanics and Dynamical Astronomy, 71:35-53, 1998.

[Mog22] F. Mogavero and J. Laskar: The origin of chaos in the Solar System through computer algebra. Astron. & Astroph., 662, L3, 2022.

[Moons94] M. Moons: Extended Schubart averaging. Celestial Mechanics and Dynamical Astronomy 60:173-186, 1994.

[Mor97] A. Morbidelli: Chaotic Diffusion and the Origin of Comets from the 2/3 Resonance in the Kuiper Belt, Icarus, 127:1-12, 1997.

[Mor02] A. Morbidelli: Modern celestial mechanics: aspects of solar system dynamics, 2002.

[MorTM95] A. Morbidelli, F. Thomas and M. Moons: The Resonant Structure of the Kuiper Belt and the Dynamics of the First Five Trans-Neptunian Objects. Icarus, 118:322-340, 1995.

[MorG97] A. Morbidelli, and M. Guzzo: The Nekhoroshev theorem and the asteroid belt dynamical system. Celestial Mechanics and Dynamical Astronomy, 65: 107-136, 1997.

[MorM93] A. Morbidelli and M. Moons: Secular Resonances in Mean Motion Commensurabilities: The 2/1 and 3/2 Cases. Icarus, Vol. 102, pp. 316-332, 1993.

[Morbi95] A. Morbidelli, V. Zappalà, M. Moons, A. Cellino, and R. Gonczi: Asteroid Families Close to Mean Motion Resonances: Dynamical Effects and Physical Implications. Icarus, Vol. 118, pp. 132-154, 1995.

[MurDer00] C. D. Murray and F. S. Dermott: Solar System Dynamics, 2000.

[Nei87] A. I. Neishtadt: Jumps of the adiabatic invariant on crossing the separatrix, and the origin of the Kirkwood gap 3:1. Doklady Akademii Nauk SSSR, Vol. 295, pp. 47-50, 1987 (Russian). English translation in Sov. Phys. Dokl. 32, pp. 571-573, 1987.

[Nei87b] A. I. Neishtadt: On the Change in the Adiabatic Invariant on Crossing a Separatrix in System with Two Degrees of Freedom. Prikl. Mat. Mekh., 51, 5, pp. 750–757, 1987.

[NeiSido04] A. I. Neishtadt and V. V. Sidorenko: Wisdom system: Dynamics in the adiabatic approximation. Celestial Mechanics and Dynamical Astronomy, Vol. 90, pp. 307-330, 2004.

[NesF00] D. Nesvorny, and F. Roig: Mean Motion Resonances in the Transneptunian Region I. The 2:3 Resonance with Neptune,. Icarus, 148, 282–300, 2000.

[NesF01] D. Nesvorny, and F. Roig: Mean Motion Resonances in the Transneptunian Region II: The 1:2, 3:4, and Weaker Resonances. Icarus 150, 104–123, 2001.

[NesTFM02] D. Nesvorný, F. Thomas, S. Ferraz-Mello, and A. Morbidelli: A perturbative treatment of the co-orbital motion. Celestial Mechanics and Dynamical Astronomy, 82:323-361, 2002.

[Nesv02] D. Nesvorný, S. Ferraz-Mello, M. Holman, and A. Morbidelli: Regular and Chaotic Dynamics in the Mean-Motion Resonances: Implications for the Structure and Evolution of the Asteroid Belt. Chapter of Asteroids III, University of Arizona Press, Tucson, pp. 379-394, 2002.

[Opik76] E. J. Öpik: Interplanetary Close Encounters. Elsevier, New York, 1976.

[PaezG20] R. I. Paea, and M. Guzzo: A study of temporary captures and collisions in the Circular Restricted Three-Body Problem with normalizations of the Levi-Civita Hamiltonian. International Journal of Non-Linear Mechanics, Vol. 120, 2020.

[Pan25] N. Pan and T. Gallardo: An attempt to build a dynamical catalog of present-day solar system co-orbitals. Celestial Mechanics and Dynamical Astronomy, Vol. 137, art. 2, 2025.

[PetroMalTre13] C. Petrovich, R. Malhotra, and S. Tremaine: Planets near mean-motion resonances. The Astrophysical Journal, Vol. 770:24, 2013.

[Pin23] G. Pinzari and X. Liu: Quantitative KAM Theory, with an Application to the Three-Body Problem. Journal of Nonlinear Science, Vol. 33, art. 90, 2023.

[NumRecipe77] W. H. Press, S. A. Teukolsky, W. T. Vetterling and B. P. Flannery: Numerical Recipes in Fortran 77: The Art of Scientific Computing. Cambridge University Press, 1992.

[RoigSFT97] F. Roig, A. Simula, S. Ferraz-Mello, and M. Tsuchida: The high-eccentricity asymmetric expansion of the disturbing function for non-planar resonant problems. Astronomy and Astrophysics, 329:339-349, 1998.

[RosE23] M. Rossi and C. Efthymiopoulos: Relegation-free closed-form perturbation theory and the domain of secular motions in the restricted three-body problem. Celestial Mechanics and Dynamical Astronomy, 135:42, 2023.

[RosG24] M. Rossi and M. Guzzo: A Kustaanheimo–Stiefel regularization of the elliptic restricted three-body problem and the detection of close encounters with fast Lyapunov indicators, Physica D, 463, 134173, 2024.

[Sail16] M. Saillenfest, M. Fouchard, G. Tommei, and G. B. Valsecchi: Long-term dynamics beyond Neptune: secular models to study the regular motions. Celestial Mechanics and Dynamical Astronomy, 126:369-403, 2016.

[ScantaG] E. Scantamburlo and M. Guzzo: Short-period effects of the planetary perturbations on the Sun-Earth Lagrangian point L_3. Astronomy and Astrophysics, Vol. 648, art. A137, 2020.

[Schu64] J. Schubart: Long-period effects in nearly commensurable cases of the restricted three-body problem. Smithsonian Astrophys. Obs., Spec. Rept. 149, 1964.

[Schu66] J. Schubart: Special cases of the restricted problem of three bodies', The theory of orbits in the solar system and in stellar systems (G. Contopoulos ed.) , 187-193, 1966.

[Szeb67] V. Szebehely: Theory of orbits, The restricted problem of three bodies. 1967.

[Sido06] V. V. Sidorenko: Evolution of asteroid orbits at the 3:1 their mean motion resonance with Jupiter (planar problem). Cosmic Research, Vol. 44, pp. 440-455, 2006.

[SidoNAZ14] V. V. Sidorenko, A. I. Neishtadt, A. V. Artemyev, and L. M. Zelenyi: Quasi-satellite orbits in the general context of dynamics in the 1:1 mean motion resonance: perturbative treatment. Celestial Mechanics and Dynamical Astronomy, Vol. 120, pp. 131-162, 2014.

[Sido24] V. V. Sidorenko: Secular evolution of co-orbital motion of two exoplanets: semi-analytical investigation. Celestial Mechanics and Dynamical Astronomy, Vol. 136, art. 25, 2024.

[TangB96] X.Z. Tang and A.H. Boozer: Finite time Lyapunov exponent and advection-diffusion equation. Physica D: Nonlinear Phenomena, 95:283-305, 1996.

[Tho98] F. Thomas: La dynamique résonnante dans le systéme solaire: application au mouvement des objects transneptuniens. PhD dissertation, Observatoire De Paris, 1998.

[TodoGLF11] N. Todorović, M. Guzzo, E. Lega, and C. Froeschlé: A numerical study of the stabilization effect of steepness. Celestial Mechanics and Dynamical Astronomy, Vol. 110, pp. 389-398, 2011.

[Valse99] G. B. Valsecchi: Planetary Close Encounters: The Engine of Cometary Orbital Evolution. In: B. A. Steves, A. E. Roy (eds) The Dynamics of Small Bodies in the Solar System: A Major Key to Solar System Studies. NATO ASI Series, Vol. 522. Springer, Dordrecht, 1999.

[Valse02] G. B. Valsecchi: Close Encounters in Öpik Theory. In: D. Benest, C. Froeschlé, (eds) Singularities in Gravitational Systems. Lecture Notes in Physics, Springer, 2002.

[ValseMGC03] G. B. Valsecchi, A. Milani, G. F. Gronchi, and S. R. Chesley: Resonant returns to close approaches: Analytical theory. Astronomy and Astrophysics, Vol. 408, pp. 1179-1196, 2003.

[Valse05] G. B. Valsecchi: Close encounters and collisions of Near-Earth asteroids with the Earth. Comptes Rendus Physique 6, pp. 337-344, 2005.

[WangMal17] X. Wang and R. Malhotra: Mean motion Resonances at High Eccentricities: The 2:1 and the 3:2 Interior Resonances. The Astronomical Journal, Vol. 154, art. 20, 2017.

[WinMur97a] O. Winter and C. Murray: Resonance and chaos: I. First-order interior resonances. Astronomy and Astrophysics, 319:290-304, 1997.

[WinMur97b] O. C. Winter and C. D. Murray: Resonance and chaos: II. Exterior resonances and asymmetric libration. Astronomy and Astrophysics, Vol. 328, pp. 399-408, 1997.

[Wis82] J. Wisdom: The origin of the Kirkwood gaps: a mapping for the asteroid motion near the 3/1 commensurability. Astronomical Journal, Vol. 87, pp. 577-593, 1982.

[Wis83] J. Wisdom: Chaotic behavior and the origin of the 3:1 Kirkwood gap. Icarus, Vol. 56, pp. 51-74, 1983.

[Wis85] J. Wisdom: A perturbative treatment of motion near the 3/2 commensurability. Icarus, Vol. 63, pp. 272-289, 1985.

[Yoko94] T. Yokoyama: Expansion of the Disturbing Function for High Eccentricity and Large Amplitude of Libration. Celestial Mechanics and Dynamical Astronomy, 60:387-400, 1994.